

Measurement of electron azimuthal anisotropy and  
implications of heavy quark flow in Au+Au  
collisions at  $\sqrt{s_{NN}} = 200$  GeV

Shingo Sakai

February 2007



Measurement of electron azimuthal anisotropy and  
implications of heavy quark flow in Au+Au  
collisions at  $\sqrt{s_{NN}} = 200$  GeV

Shingo Sakai  
(Doctoral Program in Physics)

Submitted to the Graduate School of  
Pure and Applied Sciences  
in Partial Fulfillment of the Requirements  
for the Degree of Doctor of Philosophy in  
Science

at the  
University of Tsukuba



## Abstract

The goal of the Relativistic Heavy Ion Collider (RHIC) at Brookhaven National Laboratory is to produce "Quark Gluon Plasma (QGP)", which is a new state of matter of deconfined quarks and gluons and to investigate a property of the matter. Charm quark is believed to be produced in initial collisions via gluon fusion therefore it is a powerful probe for studying the early stage of the medium created in the collisions. Elliptic flow, which is defined as a second harmonic parameter  $v_2$  of the Fourier expansion of the azimuthal distribution with respect to the reaction plane. Elliptic flow is also sensitive to the initial stage of the collision, since it originates from the initial geometrical overlap of colliding nuclei as well as the later elliptical collective expansion.

Charm quark production has been studied by measuring electrons from their semi-leptonic decays in the PHENIX experiment at RHIC. We define measured inclusive electron sample into two components: (1) 'non-photonic' - primarily semi-leptonic decays of charmed- (and bottom-) mesons and (2) 'photonic' - Dalitz decays of light neutral mesons ( $\pi_0$ ,  $\eta$ ,  $\eta'$ ,  $\omega$  and  $\phi$ ) and photon conversions in the detector material. Two independent techniques 'cocktail' and 'photon converter' methods are used to subtract the 'photonic' electrons backgrounds from the measured inclusive electron in order to extract the 'non-photonic' electron signal from the heavy flavor decays. More than 50 % of measured inclusive electrons come from 'non-photonic' sources above 1.5 GeV/c which is given by the relative ratio of those 'photonic' and 'non-photonic' sources and materials in the PHENIX experiment.

In this thesis, we study the elliptic azimuthal anisotropy of charm quark via electron measurement. We first measure the transverse momentum dependence of the azimuthal anisotropy parameter  $v_2$  for inclusive electrons at mid-rapidity ( $|\eta| < 0.35$ ). The data are taken with the PHENIX detector in Au+Au collisions at  $\sqrt{s_{NN}} = 200$  GeV during the fourth experiment period at RHIC run (2004 - 2005). The  $v_2$  of electrons from heavy flavor decays is then extracted by subtracting the  $v_2$  of 'photonic' electrons. This 'photonic' electron  $v_2$  is determined with a Monte Carlo simulation using measured  $v_2$  and  $p_T$  distributions of these 'photonic' sources, which is same as the 'cocktail' method, and this has also been confirmed by the 'converter' method. The extracted  $v_2$  of the 'non-photonic' electron clearly shows positive value below  $p_T = 3.0$  GeV/c, which is slightly smaller to pion  $v_2$  though. The  $v_2$  increases with  $p_T$  up to about 1.5-2.0 GeV/c and then saturate or slightly reduces with increasing  $p_T$ .

The main source of the 'non-photonic' electrons is  $D$  meson decay at relatively low  $p_T$  below 2-3 GeV/ $c$ . The non-zero  $v_2$  for the 'non-photonic' electrons automatically gives a non-zero  $v_2$  of  $D$  meson according to the decay kinematics.  $D$  meson  $v_2$  is estimated with a Monte Carlo simulation using the measured 'non-photonic' electron  $v_2$ . Various  $p_T$  dependent shape of  $D$  meson  $v_2$  are assumed in the simulation and the peak  $v_2$  value is obtained to be  $0.09 \pm 0.03$  at about 2-3 GeV/ $c$ . This corresponds to a non-zero  $v_2$  measurement of  $D$  meson in Au+Au collisions at  $\sqrt{s_{NN}} = 200$  GeV. Based on a quark coalescence model, the charm quark  $v_2$  is finally estimated. The same  $p_T$  dependent shape for  $v_2$  of charm quark are assumed as for the light and strange quarks. The effective mass of charm quark is used for coalescing them at similar velocity. Simultaneous fitting of measured  $v_2$  parameters for pion, Kaon, proton and 'non-photonic' electron are done with 2  $v_2$  parameters for light and heavy quarks including the quark coalescence effect and  $D$  meson decay kinematics. The extracted charm quark  $v_2$  has similar magnitude compared with the light quark. Besides the binary collision scaling of 'non-photonic' electron yield at relatively low  $p_T$  region below 2 GeV/ $c$ , the strong elliptic anisotropy of the heavy quark, which is similar to the light quark, indicates a collectivity of different mass quarks during the quark phase of the high density matter created in the ultra-relativistic heavy-ion collisions. The collectivity of the heavy quark is one of the strong evidence of the quark gluon plasma. The presented results on  $v_2$  measurement of 'non-photonic' electron give a strong support of this scenario.

# Acknowledgement

This thesis work was supported by many people. I would like to take this opportunity to thank the many people who have made this work possible.

I first would like to express my great gratitude to Prof. Yasuo Miake for providing me the exciting field of physics. His appropriate and valuable advice show me the way to promote the present work, and I could learn a lot from him as an experimental physicist.

I express my heartfelt thanks to Prof. Shinichi Esumi. His appropriate and valuable advice and discussions for the analysis are very helpful for this work. I am much obliged to Prof. Tatsuya Chujo for his advice and discussion not only in the analysis but also work at BNL. I wish to express my thanks to Dr. Susumu Sato for leading me to the PHENIX experiment. His appropriate advice have helped me a lot to work at BNL. I would like also thank Prof. Motoi Inaba. His advice of electronics for detectors is very helpful for me to work at BNL.

I wish to acknowledge for all the collaborations of the PHENIX experiment. I am grateful to the spokesperson Prof. W. A. Zajc for his various arrangements for my activity at BNL. I express my appreciation to deputy spokesperson Dr. Yasuyuki Akiba for various advice for the electron analysis. I wish to express my special thanks to Prof. M. Kaneta for his helpful advice on the analysis. I would like to many thanks to Heavy-Light convenors, Prof. R. Averbeck, Dr. M. L. Brooks, Dr. V. Cianciolo, Prof. A. D. Frawley, Prof. T. K. Hemmick, Dr. A. Molov, Dr. D. Silvermyr and Dr. W. Xie, for their kind helps and many useful advice for the analysis.

I wish to acknowledge for all the members of the PHENIX-J. I gratefully acknowledge to the PHENIX-J leader, Prof. Hideki Hamagaki for the continuous financial support. I extend hearty thanks to Prof. Kyoichiro Ozawa for the financial support and various advice for working at BNL. I acknowledge for Dr. F. Kajihara and Dr. T. Gunji for giving me a lot of information about electron analysis. I also acknowledge for Mr. T. Hachiya and Mr. T. Nakamura for their kind help and useful advice at BNL.

Here I acknowledge all the members of the high energy nuclear experiment group at University of Tsukuba. I would like to thank Mr. H. Masui for giving me many information

of the reaction plane analysis. I would like to thank Mr. M. Konno, Mr. T. Takagi and Ms. M. Shimomura for their help, freindship and kindness. I would like to thank Dr. A. Kiyomichi for his kind helps. I would like to thank Mr. S. Kato and Mr. Y. Nagata for supporting computer environment. I also acknowledge Mr. H. Tsuruoka, Mr. M. Ono, Mr. Y. Kuroki, Mr. M. Oka, Mr. M. Narisawa, Mr. K. Miki, Mr. M. Sato, Mr. Y. Ikeda, Mr. R. Tanabe, Mr. Y. Tomita, Mr. T. Niida, Mr. K. Watanabe, Mr. D. Sakata, Mr. A. Saito, Mr. M. Sano, Mr. N. Shiohara and Ms. N. Seya for their freindship.

Finally, I would like to express my great appreciation to my parents, Kougi Sakai and Emiko Sakai, for their support and encouragement to accomplish this work.



# Contents

<b>1</b>	<b>Introduction</b>	<b>1</b>
1.1	Quantum Chromodynamics and Quark Gluon Plasma . . . . .	1
1.2	Quark Gluon Plasma and Relativistic Heavy Ion Collisions . . . . .	2
1.3	Thermalization . . . . .	6
1.3.1	Chemical Equilibrium . . . . .	6
1.3.2	Kinematical equilibrium and the collective flow . . . . .	8
1.4	Suppression of high $p_T$ particle . . . . .	12
1.5	Quark coalescence/recombination . . . . .	16
1.5.1	Baryon excess . . . . .	16
1.5.2	Quark coalescence model . . . . .	17
1.6	Charm quark production in RHIC . . . . .	20
1.7	Thesis motivation . . . . .	22
<b>2</b>	<b>The PHENIX experiment</b>	<b>24</b>
2.1	The Relativistic Heavy Ion Collider (RHIC) . . . . .	24
2.2	Overview of PHENIX experiment . . . . .	27
2.3	Magnet system . . . . .	29
2.4	Global detectros . . . . .	32
2.4.1	Beam-Beam counters (BBCs) . . . . .	32
2.4.2	Zero-Degree Calorimeters (ZDCs) . . . . .	33
2.5	Central arms detectros . . . . .	35
2.5.1	Drift Chambers (DCs) . . . . .	35
2.5.2	Pad Chambers (PC) . . . . .	37
2.5.3	Ring Imaging Cherenkov Counters (RICHs) . . . . .	37
2.5.4	Electro-Magnetic Calorimeters (EMCals) . . . . .	40
2.5.5	Time of flight (TOF) . . . . .	40

<b>3</b>	<b>Data analysis</b>	<b>43</b>
3.1	Event selection . . . . .	43
3.2	Centrality determination . . . . .	44
3.3	Track Reconstruction and momentum determination . . . . .	44
3.4	Electron identification . . . . .	47
3.5	Azimuthal anisotropy analysis . . . . .	53
3.5.1	Fourier Expansion of Azimuthal Distribution . . . . .	53
3.5.2	Reaction Plane method . . . . .	54
3.5.3	Reaction Plane Determination . . . . .	55
3.5.4	Reaction Plane Resolution . . . . .	57
3.6	Determination of non-photonic electron at PHENIX . . . . .	59
3.6.1	Electron sources . . . . .	59
3.6.2	Cocktail method . . . . .	59
3.6.3	Photon converter method . . . . .	60
3.6.4	Ratio of the non-photonic to photonic electrons $R_{NP}$ . . . . .	62
<b>4</b>	<b>Experimental Results</b>	<b>64</b>
4.1	Inclusive Electron $v_2$ . . . . .	64
4.2	Non-photonic electron $v_2$ . . . . .	68
4.2.1	Method of non-photonic electron $v_2$ determination . . . . .	68
4.2.2	Determination of photonic electron $v_2$ by the cocktail method . . . . .	69
4.2.3	Kaon decay background subtraction . . . . .	77
4.3	Systematic uncertainties . . . . .	80
4.4	Result . . . . .	83
<b>5</b>	<b>Discussions</b>	<b>84</b>
5.1	Non-photonic electrons . . . . .	84
5.2	Kinematics of $D$ meson decay and $v_2$ . . . . .	87
5.3	Charm quark $v_2$ assuming Quark Coalescence Model . . . . .	91
5.4	Bottom quark contribution to the non-photonic electron $v_2$ . . . . .	97
5.5	Comparison with charm quark thermalization model . . . . .	98
5.6	Non-photonic electron $R_{AA}$ and $v_2$ . . . . .	101
<b>6</b>	<b>Conclusions</b>	<b>105</b>
<b>A</b>	<b>Data points</b>	<b>111</b>

<b>B Kinematics</b>	<b>112</b>
B.1 Transverse Momentum and Transverse Mass . . . . .	112
B.2 Rapidity . . . . .	112
B.3 Centrality Variables . . . . .	113

# List of Figures

1.1	A schematic phase diagram of nuclear matter as a function of temperature $T$ and baryon chemical potential $\mu$ . The figure is taken from [2]. . . . .	3
1.2	$\varepsilon_{Bj}\tau$ as a function of $N_{part}$ measured at three RHIC energies. . . . .	5
1.3	Space-time evolution of a nucleus-nucleus collisions. The time and temperature are calculated by the hydrodynamical framework [6] . . . . .	6
1.4	Ratios of measured yield of various particles in $\sqrt{s_{NN}} = 130$ GeV and 200 GeV, compared with the statistical thermal model [11]. . . . .	7
1.5	Inverse slope parameter $T$ as a function of particle mass. They are compared at mid-rapidity in $p + p$ , S+S and Pb+Pb collisions [15]. . . . .	9
1.6	An illustration of non-central Au-Au collisions. The plane defined as the direction of the impact parameter ( $x$ ) and direction of the beam axis ( $z$ ) is called “reaction plane”. . . . .	10
1.7	Beam energy dependence of $v_2$ measured at AGS, SPS and RHIC. . . . .	11
1.8	Identified particle ( $\pi$ , K, p) $v_2$ as a function of $p_T$ [19]. The lines in the figure are the hydrodynamical model calculation. [23] . . . . .	12
1.9	Comparison of two-particle azimuthal angular correlations of charged particles for central Au + Au, central $d + Au$ and $p + p$ collisions, where $N_{Trigger}$ is the number of high $p_T$ particles. . . . .	13
1.10	Nuclear modification factor measured for $\pi^0$ and charged particle in Au + Au collisions ( $R_{AA}$ ) and in $d + Au$ collisions ( $R_{dAu}$ ) in $\sqrt{s_{NN}} = 200$ GeV as a function of $p_T$ [25]. The bands around the data points show systematic errors, while the shade band around unity indicates the normalization uncertainty. . . . .	14
1.11	$p/\pi$ ratio as a function of $p_T$ for central (0-10 %), mid-central (20-40 %) and peripheral (60-92 %) collisions [30]. The dashed and dotted lines are proton and pion ratio in gluon and in quark jets [31]. . . . .	16
1.12	$p/\pi$ ratio measured by PHENIX [30] and quark coalescence model calculations for the comparison. This picture is taken from [5]. . . . .	17

1.13	$v_2/n$ as a function of $p_T/n$ where $n$ is the number of constituent quarks plus anti-quarks ( $n = 2$ for meson and $n = 3$ for baryon). . . . .	19
1.14	(a) Invariant differential cross section of electrons from heavy flavor, charm and bottom, in $p + p$ collisions at $\sqrt{s_{NN}} = 200$ GeV measured at PHEXNIX experiment [39]. The curves are the FONLL calculations. (b) Ration of the data and the FONLL. The upper and lower curves are theoretical upper and lower limit of the FONLL. . . . .	21
1.15	Theoretical prediction of $p_T$ distributions of initial (solid), prethermal (dot-dashed) and thermal (dashed) charm production for central Au+Au collisions at RHIC energy, $\sqrt{s_{NN}} = 200$ GeV [41]. . . . .	22
2.1	A picture of RHIC complex. . . . .	24
2.2	RHIC acceleration scenario for gold. The tandem Van de Graff accelerators, the Booster synchrotron, and the Alternating Gradient Synchrotron (AGS) serve as the injector for RHIC. . . . .	26
2.3	PHENIX experiment setup in the 4th year of RHIC run (Run4). (Top:Cross section perpendicular to the beam pipe. Bottom: East side view of the cross section along the beam pipe.) PHENIX consists of four parts of spectrometer arms and a set of global detectors. The spectrometers around mid-rapidity are called central arms (west and east arm), and those around forward rapidity are called muon arms. . . . .	28
2.4	PHENIX acceptance of leptons and hadrons. . . . .	29
2.5	Line drawings of the PHENIX magnets, shown in perspective and cut away to show the interior structures. . . . .	31
2.6	(a) A picture of BBC array comprising 64 BBC elements. (b) A picture of BBC element which consists of one-inch mesh dynode PMT mounted on a 3 cm quartz radiator. (c) The configuration of the 64 PMTs of each BBC. . . . .	32
2.7	(a) Top view of the beam geometry and ZDC location. (b) A picture of ZDC. . . . .	34
2.8	(left) The layout of wire position of DCs. (right) Constriction of a DC frame. . . . .	36
2.9	A picture of the Pad Chamber system in PHENIX. . . . .	38
2.10	A cutaway view of one arm of the PHENIX RICH detector. . . . .	39
2.11	Interior view of a Pb-scintillator calorimeter module showing a stack of scintillator and lead plates, wavelength shifting fiber readout and leak fiber inserted in the central hole. . . . .	41

2.12	Schematic diagram of the components of a single TOF panel which consists of 96 plastic scintillation counters with PMTs at both ends, light guides and supports. . . . .	42
3.1	Correlation between the charge sum measured by BBC and energy of spectator neutrons measured by the ZDC. The lines in the figure present the definition of centrality classes in the ZDC vs. BBC plot. . . . .	45
3.2	Definition of the Hough transform parameters ( $\phi$ and $\alpha$ ) for the drift chamber track reconstruction. The X1 and X2 hits in the drift chamber are shown as small circles. . . . .	46
3.3	an illustration of electron identification by RICH. (a) Cherenkov photons are emitted by the electrons at RICH. (b) The Cherenkov photons are reflected by the mirrors and make a circle with 5.9 cm radius on the PMT arrays. . .	48
3.4	$(E - p)/p/\sigma$ distributions in different $p_T$ slices. The red line is for electrons after subtracting background (blue line) from electrons identified by RICH (black line). . . . .	50
3.5	$E/p$ distributions for electrons (black solid line), swapped background (dotted line), and hadrons (red solid line). The figure is taken from [46] . . . . .	51
3.6	Signal to background ratio ( $B/(S + B)$ ) for electron signals as a function of $p_T$ . . . . .	52
3.7	Illustration of the reaction plane determination. The true reaction plane can not measure directly therefore the plane is determined by using anisotropic flow itself. . . . .	55
3.8	Azimuthal angle correlation of the measured reaction plane North side and South side of BBC. . . . .	56
3.9	Centrality dependence of the combined reaction plane resolution that is determined by the BBCs. . . . .	58
3.10	$p_T$ distribution of the background electrons [54][55]. The background electrons are calculated by the hadron decay generator. . . . .	60
3.11	Invariant yield spectra of the photonic electron. The curve in the figure is the spectra from cocktail method and the closed circles is from the conveter method. . . . .	61
3.12	Invariant yield of the non-photonic electron measured in Au+Au collisions at $\sqrt{s_{NN}} = 200$ GeV [55]. . . . .	62
3.13	Transverse momentum dependence of the ratio of the number of non-photonic electrons to the number of photonic electrons ( $R_{NP} = N_e^{non-\gamma}/N_e^\gamma$ ). . . . .	63

4.1	Transverse momentum dependence of the inclusive electron $v_2$ measured with 10 % step of the centrality bin. The $v_2$ was already corrected for the reaction plane resolution. . . . .	66
4.2	Inclusive electron $v_2$ for the the minimum bias events as a function of $p_T$ . . . . .	67
4.3	Relative contributions of electron sources ( $\pi^0$ Dalitz, $\gamma$ conversion, $\eta$ Dalitz and direct $\gamma$ ) to the photonic electrons. The data is obtained from Fig 3.10. . . . .	70
4.4	$p_T$ dependence of electron $v_2$ from $\pi^0$ decay. . . . .	71
4.5	$\eta$ $v_2$ calculated by the Blast wave model. The dashed lines are the systematic uncertainties from the systematic uncertainty of $\pi$ , kaon, proton $v_2$ . . . . .	73
4.6	$p_T$ dependence of electron $v_2$ from $\eta$ decay. $\eta$ $v_2$ was assumed same as kaon in this calculation. . . . .	73
4.7	Direct $\gamma$ $v_2$ as a function of $p_T$ measured at PHENIX. The closed circles are inclusive $\gamma$ $v_2$ and the open squares are background $\gamma$ $v_2$ mainly from $\pi^0$ decay. The open circles corresponds to the direct $\gamma$ $v_2$ [59]. . . . .	74
4.8	$p_T$ dependence of photonic electron $v_2$ obtained by the cocktail and converter method. The lines on the figure are photonic electron $v_2$ calculated by the cocktail method. The solid line is the mean of $v_2$ and the dashed lines are the systematic uncertainty of the cocktail method. The photonic electron $v_2$ from converter is shown as boxes. . . . .	75
4.9	Inclusive electron $v_2$ measured with/without converter (Minimum bias event). . . . .	76
4.10	$p_T$ dependence of the non-photonic electron $v_2$ (closed circles) together with the inclusive electron $v_2$ (open circles) and photonic electron $v_2$ (solid line). . . . .	77
4.11	Contribution of kaon decays to the non-photonic electron yield. The contribution is 18% at $p_T = 0.5$ GeV/ $c$ and decreases to less than 5% for $p_T > 1.0$ GeV/ $c$ . . . . .	78
4.12	Input kaon $p_T$ spectra for the kaon decay study simulation (the solid line). The spectrum at $p_T > 2.0$ GeV/ $c$ we assumed that the shape is same as $\pi^0$ spectrum. The $p_T$ spectrum is obtained by the scaled $\pi^0$ spectra connected around $p_T = 2.0$ GeV/ $c$ to the low $p_T$ kaon spectrum with the scale factor 0.55. . . . .	79
4.13	$p_T$ shape dependence of electron $v_2$ from kaon decay. The $v_2$ which is calculated from the exponential shape (the dashed red line in Fig. 4.12) is shown as red points and the scaled $\pi^0$ spectra (the blue line in Fig. 4.12) is shown as blue points. No shape dependence is seen in the electron $v_2$ . . . . .	79

4.14	(Top) The inclusive electron $v_2$ measured with three type of the reaction plane. (Bottom) The relative ratio respect to the $v_2$ measured with combined reaction plane ( $v_2^{N(S)}/v_2^{comb}$ ). . . . .	81
4.15	Systematic uncertainty from the electron identification is estimated by measuring the inclusive electron $v_2$ with slightly change the condition of the standard electron identification cut (top). The relative ratio of the $E/p$ is about 2%, the $n0$ is about 2% and the $\chi^2/npe0$ is 1 % (bottom). . . . .	82
4.16	Transverse momentum dependence of non-photonic electron $v_2$ in Au+Au collisions at $\sqrt{s_{NN}} = 200$ GeV for the minimum bias events. The vertical solid lines mean statistical error and the brackets mean $1 \sigma$ systematic uncertainty of the non-photonic electron $v_2$ . . . . .	83
5.1	(Left) Non-photonic electron yield ( $0.8 < p_T < 4.0$ GeV/ $c$ ) measured in Au+Au collisions at 200 GeV [42] scaled by $N_{coll}$ as a function of $N_{coll}$ . Normalizing by the nuclear overlap function obtained charm electron cross section per $N + N$ collisions (right-hand scale). (Right) Invariant yields of electrons from heavy flavor decays for different Au+Au centrality [55], scaled by powers of ten for clarity. The solid lines are the result of a FOMLL calculation of heavy flavor decay normalized to the $p + p$ data [39] for each centrality class. . . . .	85
5.2	$p_T$ dependence of the confidence level for the non-zero non-photonic electron $v_2$ . . . . .	86
5.3	Comparison of the non-photonic electron $v_2$ with pion $v_2$ . The dashed line on the figure is the electron $v_2$ from charm decay assuming charm has same $v_2$ as u quark. . . . .	87
5.4	(Left) Momentum correlation between $D$ meson and the decay electrons. The open circles represent the mean $p_T$ of $D$ meson momentum distribution for the given electron momentum and closed data points represent the peak of the $D$ meson momentum distribution. (Right) $p_T$ dependence of the decay angle correlation between $D$ mesons and the decay electrons. . . . .	88
5.5	Results of the $\chi^2$ test between measured non-photonic electron $v_2$ and electron $v_2$ calculated by the simulation assuming $D$ meson $v_2$ shape as a function of the scaled factor $a(\%)$ . . . . .	90
5.6	$1 \sigma$ bands for each of the five assumed $D$ $v_2$ shapes. . . . .	91



5.7	$D$ meson $v_2$ estimated by the measured non-photonic electron $v_2$ . The closed data points represent the most suitable $D$ meson $v_2$ ( $\chi^2$ minimum) from the calculation. The dashed lines are $\chi^2$ minimum+2 value for the determination. The open circles is $\pi$ $v_2$ . . . . .	92
5.8	Universal $v_2$ shape for quarks in the calculation. . . . .	93
5.9	Fitting result of non-photonic electron $v_2$ , kaon $v_2$ and proton $v_2$ . The open circles mean decay electron $v_2$ from the $D$ meson. . . . .	94
5.10	Contour plot of $v_2$ of $c$ quark and $u$ quark which are defined as $v_{2,u} = a \times v_{2,q}$ and $v_{2,c} = b \times v_{2,q}$ . Here $v_{2,q}$ is a quark $v_2$ determined by the measured $v_2$ . Parameters $a$ and $b$ are obtained by fitting the measured non-photonic electron $v_2$ , Kaon $v_2$ and proton $v_2$ . The contour lines are one sigma step. . . . .	95
5.11	Charm quark $v_2$ from the calculation based on the quark coalescence model. The solid lines are obtained from 1 $\sigma$ contour level, the dashed lines are obtained 2 $\sigma$ contour level and the dotted + dashed lines are obtained from 4 $\sigma$ contour level by the fitting. The open boxes mean $u$ quark $v_2$ . . . . .	96
5.12	Electron $v_2$ from $D$ meson and $B$ meson. The curve (1) is assumed no $b$ quark contributions to the non-photonic electron (only take into account charm decay). The curve (2) is assumed that $D$ meson and $B$ meson $v_2$ have same $v_2$ . And the curve (3) is assumed that $B$ meson $v_2$ is zero. . . . .	97
5.13	The electron spectra from the model calculations. The dashed curves are the PYTHIA calculation and solid curves are the results from the thermal hydrodynamic model. The data in the figure is non-photonic electron measured at PHENIX in Au+Au collisions at $\sqrt{s_{NN}} = 130$ GeV [51]. The picture is taken from [10]. . . . .	99
5.14	Comparison of the non-photonic electron $v_2$ with two different charm flow scenarios [62]. The solid line corresponds to the no rescattering of the initially produced charm quarks (without flow), while the dashed line reflects the effect of complete thermalization (with flow). . . . .	100
5.15	$R_{AA}$ of the non-photonic electrons in 0-10 % central collisions compared with model calculations assuming the initial gluon densities is 3500 ( $dN^g/dy = 3500$ ). . . . .	102
5.16	(a) $R_{AA}$ of the non-photonic electron in 0-10 % central collisions. (b) $v_2$ for the non-photonic electron in minimum bias collisions. The curves in the figure are model calculations assuming elastic scattering mediated by resonance excitation of $D$ meson and $B$ meson in QGP [65]. . . . .	104

B.1 an illustration of the collision geometry for a non-head on nucleus-nucleus collision. The nucleons in the overlap region of the two nuclei participate in the collisions are called "*participants*" and the rest nucleons which are not participate in the collisions are called "*spectator*" . . . . . 114

# Chapter 1

## Introduction

The goal of high energy nucleus collisions at the Relativistic heavy ion collider (RHIC) is to create "Quark-Gluon plasma" (QGP) which is a plasma state of quarks and gluons. In this chapter we introduce QGP and review the experimental results at RHIC. Finally, we present the thesis motivation, why we study elliptic flow of charm quark.

### 1.1 Quantum Chromodynamics and Quark Gluon Plasma

"What is the fundamental particle?" is one of the longstanding questions for mankind. At the present day, the fundamental particle is thought to be "quark". Quark was introduced by M. Gell-Mann and G. Zweig to classify hadrons. They proposed that all hadrons are made from quarks and the model based on the proposition is called quark model. In the model hadron made from two quark and anti-quark pair is called meson and made from three quarks is called baryon. One of the most interesting features of the quark is that they are confined in hadron and they can not be observed outside hadron. The strong interaction, one of the fundamental interactions in the nature, is the interaction which binds quarks and makes hadrons. The remarkable feature of the strong interaction is that the interaction is weak at shorter distances or large momentum transfer ( $Q^2$ ). The feature of the strong interaction is called "asymptotic freedom". Due to the feature quarks move as free, non-interacting particles, in the depth of hadrons. Experimentally such feature has been observed in the deep inelastic scattering between leptons and hadrons in 1969. On the other hand, the interaction is strong with distances or small momentum transfer therefore quarks are pulled back by the strong force if they try to move from hadrons. It is the reason why single quark has not been observed alone.

The strong interaction is described by the field theory of Quantumchromo dynamics

(QCD). QCD is based on non-Abelian gauge theory and the gauge theory represents asymptotic freedom. In the theory, the field is given as color charge and gluons are gauge bosons that mediate strong color charge interactions between quarks. As results of QCD calculation, the effect of confinement for quarks is broken and a matter becomes a plasma state of quark and gluons under the very high temperature and high density circumstance. Such the state of the matter is called "Quark-Gluon plasma" (QGP). Lattice QCD predicts the phase transition to a QGP at a temperature  $T \sim 170$  MeV which corresponds to an energy density  $\epsilon \sim 1.0$  GeV/fm<sup>3</sup> [1] at zero baryon density, nearly an order of magnitude larger than that of normal nuclear matter. It is thought that such a state of matter existed in the early universe, a few  $\mu$ s after "Big Bang" which is thought the origin of the universe. Now we have already known that the universe has been expanding since Big-Bang. If we extrapolate the universe to Big-Bang, dawn of the universe can be extremely high dense and temperature. Therefore the research of QGP is an important topic not only testing QCD but also astrophysics.

## 1.2 Quark Gluon Plasma and Relativistic Heavy Ion Collisions

Figure 1.1 shows the phase diagram of nuclear matter as a function of temperature and baryon chemical potential  $\mu$ . Ordinary nuclear matter exist at  $T \sim 0$  and  $\mu_B \sim 1$ . It is predicted that the nuclear matter becomes QGP state by raising temperature or density. Relativistic heavy ion collisions are powerful tool to achieve high temperature (or density) because a large amount of energy is deposited in the collision zone.

Since 1980 attempt to create QGP has been performed at AGS (Alternating Gradient Synchrotron) in Brookhaven National Laboratory and Super Proton Synchrotron (SPS) in European Laboratory for Particle Physics (Table 1.1). The AGS accelerates Si ions up to the center of mass energy per nucleon ( $\sqrt{s_{NN}}$ ) 5.4 GeV and Au ions up to 4.8 GeV. The SPS accelerates O ions up to 19.4 GeV and Pb ions up to 17.4 GeV. The relativistic heavy ion collider (RHIC) at BNL is the world's first head-on collider and the maximum center of mass energy per nucleon pair is 200 GeV. RHIC has been operated from June 2000 and achieved the center of mass energy per nucleon 200 GeV in 2001. LHC is the future high energy heavy ion collision program and it will be operated from 2007.

The initial energy density of the collision region can be estimated by the Bjorken energy density [3] as

$$\epsilon_{Bj} = \frac{1}{\tau_{form} A_{\perp}} \frac{dE_T(\tau_{form})}{dy} \quad (1.1)$$

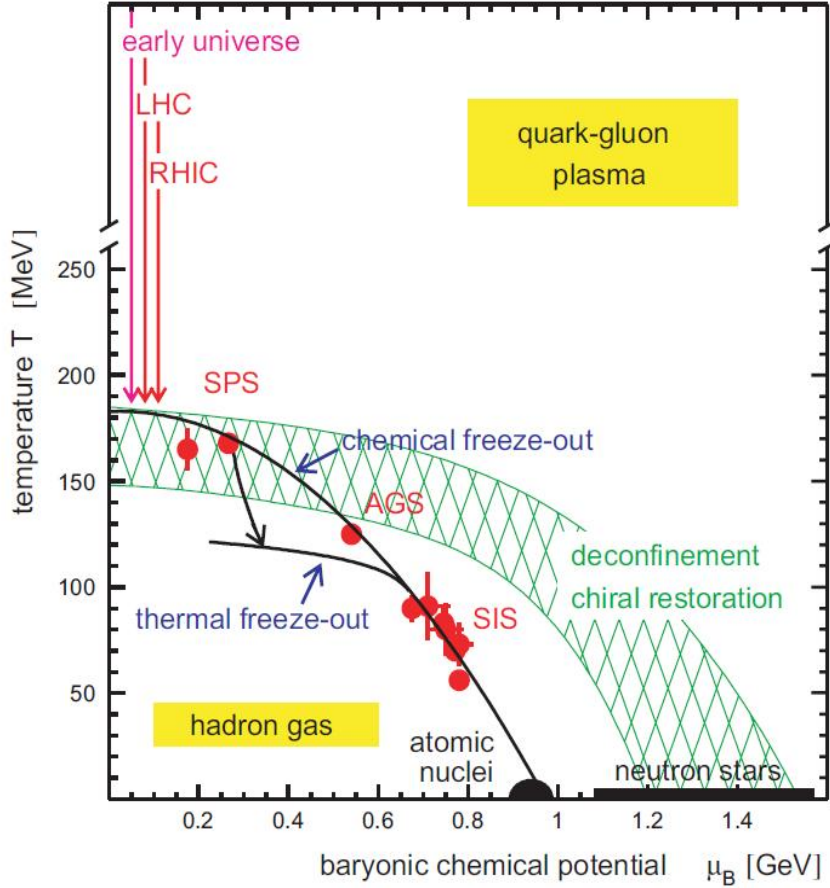


Figure 1.1: A schematic phase diagram of nuclear matter as a function of temperature  $T$  and baryon chemical potential  $\mu$ . The figure is taken from [2].

where  $\tau_{form}$  is a proper time that the secondary particles can be consider "formed",  $A_{\perp}$  is the nuclei transverse over rap area and  $dE_T/dy$  is the transverse energy per unit rapidity. In PHENIX experiment, the value of  $dE_T/d\eta$  has been measured and obtained 600 GeV for 0-5% centrality [4]. This leads to  $\varepsilon_{Bj}\tau_{form} = 5.4 \pm 0.6 \text{ GeV } c^{-1} \text{ fm}^{-2}$  for  $\sqrt{s_{NN}} = 200 \text{ GeV}$  ( $A_{\perp}$  was  $140 \text{ fm}^2$  and a scale factor of 1.25 was used for the transformation from  $dE_T/d\eta$  to  $dE_T/dy$  [4]). Figure 1.2 shows  $\varepsilon_{Bj}\tau_{form}$  as a function of the number of participant nucleons ( $N_{part}$ ) measured at PHENIX [4]. Historically,  $\varepsilon_{Bj}$  has been calculated by choosing  $\tau_{form} = 1 \text{ fm}/c$ . As described in [5], more realistic value of  $\tau_{form}$  from experiment is  $0.35 \text{ fm}/c$  which is larger than the crossing time of the nuclei ( $2R/\gamma = 0.13 \text{ fm}/c$ ) and this leads to  $\varepsilon_{Bj} \sim 15 \text{ GeV}/\text{fm}^3$  in central Au+Au collisions at  $\sqrt{s_{NN}} = 200 \text{ GeV}$ . This energy density is

Accelerator	Location	Ion beam	$\sqrt{s_{NN}}$	Start
AGS	BNL	$^{16}\text{O}, ^{28}\text{Si}$	5.4	Oct. 1986
		$^{197}\text{Au}$	4.8	Apr. 1992
SPS	CERN	$^{16}\text{O}, ^{32}\text{S}$	19.4	Sep. 1986
		$^{208}\text{Pb}$	17.4	Nov. 1994
RHIC	BNL	$^{197}\text{Au}+^{197}\text{Au}$	130	2000
		$^{197}\text{Au}+^{197}\text{Au}$	200	2001
LHC	CERN	$^{208}\text{Pb}+^{208}\text{Pb}$	5600	2007(project)

Table 1.1: List of heavy ion accelerator facilities with the ion beams, the center of mass energy.

larger than  $1 \text{ GeV}/\text{fm}^3$  which was predicted by the lattice QCD, therefore the matter created at RHIC might be above the threshold for QGP formation.

A key issue of QGP formation at the relativistic heavy ion collisions is the thermalization of the matter created by the collisions. At the very early stage of the collisions among quarks and gluons scatter each other in the collision zone. If they scatter over and over again, the matter made from quarks and gluons can be achieved a thermal equilibrium, *i.e.* quark gluon plasma. Once thermal equilibrium is achieved, the evolution of the matter would be described by the hydrodynamical framework. Figure 1.3 shows the illustration of the space-time evolution of the medium created by heavy ion collisions at RHIC as a function of temperatures and times calculated by the hydrodynamical framework [6]. At the center of the collision zone, pressure is larger than the surrounding area thus the medium expands and temperature is drop. At the expanding process medium passes through the mixed phase of QGP and hadron gas then the medium becomes hadron gas state. In the hadron gas, inelastic scattering of hadrons continues until chemical freeze-out temperature where hadron species and ratios are fixed (Chemical equilibrium). During this time the system is still expanding, finally elastic scattering of hadrons finishes at kinetic freeze-out temperature where hadron momentum are fixed (Kinematical equilibrium).

Various measurements have been proposed to study QGP and the property in the relativistic heavy ion collisions. Here we introduce some of them.

1. Particle ratio - chemical freeze-out

Measurement of particle ratios give us information about chemical equilibrium due to particle species are fixed at the point of chemical freeze-out.

2. Elliptic flow

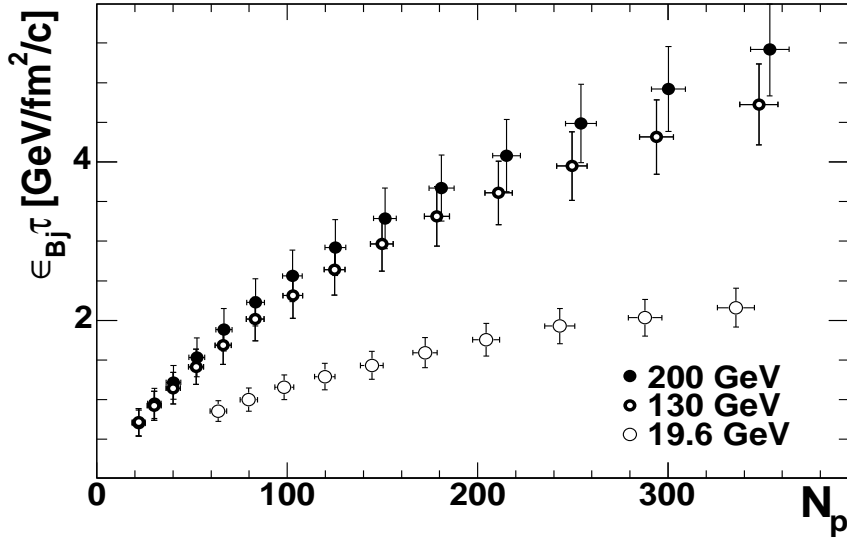


Figure 1.2:  $\epsilon_{Bj}\tau$  as a function of  $N_{part}$  measured at three RHIC energies.

Elliptic flow, collective motion in azimuthal space, is thought sensitive to the early stage of collisions. In the hydrodynamical frame work, elliptic flow is arised as a result of pressure gradient in thermal equilibrium system. If strong elliptic flow is observed, it indicates thermal equilibrium status is achieved at the RHIC energy.

### 3. Suppression of high $p_T$ particle- energy loss

QCD predicts that the partons (quark and gluons) lose their energy when they propagate the dense matter [7]. As the result, jet productions are suppressed. One of the good methods to study parton energy loss in the matter is a comparison of the yield for high  $p_T$  particles in Au+Au collisions with the yield in  $p + p$  collisions. The origin of the high  $p_T$  particle production is jet, therefore high  $p_T$  particle production is suppressed compared with the production in  $p + p$  collisions if partons lose their energy in the matter.

### 4. Charmed hadrons

Charm quark is believed to be produced in initial collisions via gluon fusion and it propagates through hot and dense medium created in the collisions. At RHIC energies, charm quark energy loss [8], charm quark coalescence [9] and charm quark flow [10] has been proposed to study the properties of the medium created by Au+Au collisions. Such topics can be observed via charm hadron, *i.e.*  $D$  meson, measurement.

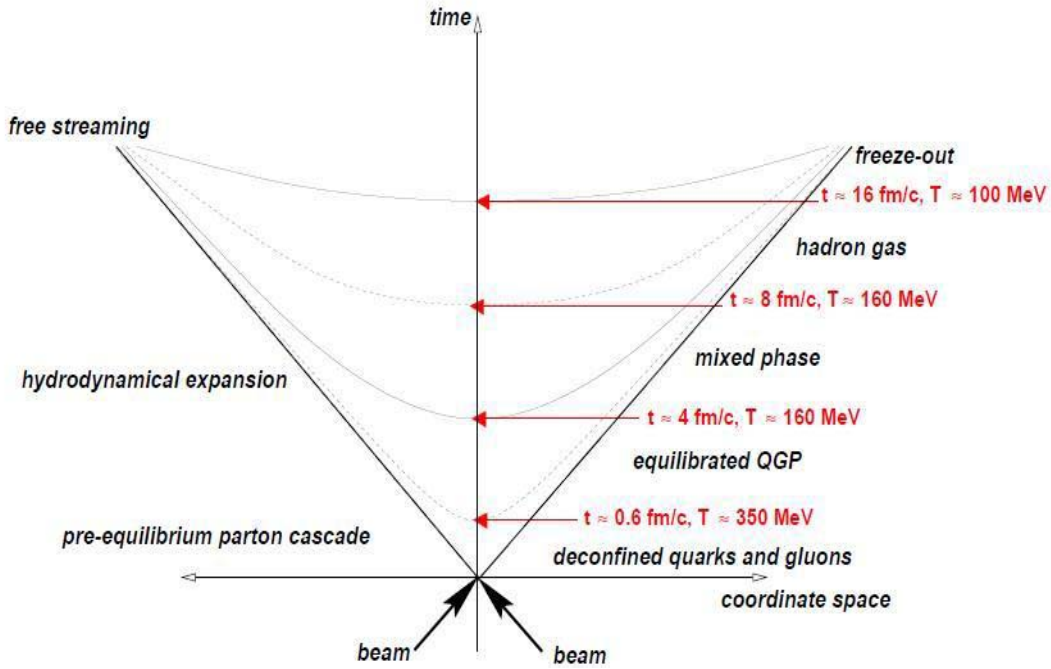


Figure 1.3: Space-time evolution of a nucleus-nucleus collisions. The time and temperature are calculated by the hydrodynamical framework [6]

## 1.3 Thermalization

### 1.3.1 Chemical Equilibrium

Measurement of particle ratios give us information about chemical equilibrium due to particle species are fixed at the point of chemical freeze-out. A simple statistical model which assumes local thermal equilibrium reproduces well the measured ratios. The statistical model is based on a grand canonical ensemble to describe the partition function and hence the density of the particles of species  $i$  an equilibrated fireball is given as by

$$n_i = g_i \frac{dp^3}{(2\pi)^3} \frac{1}{\exp((E_i - \mu_i)/T) \pm 1}, \quad (1.2)$$

with particle density  $n_i$ , spin degeneracy  $g_i$ , momentum  $p$ , total energy  $E$  and chemical potential  $\mu_i = \mu_B B_i - \mu_S S_i - \mu_{I_3} I_i^3$ . The quantities  $B_i$ ,  $S_i$  and  $I_i^3$  are baryon, strangeness and



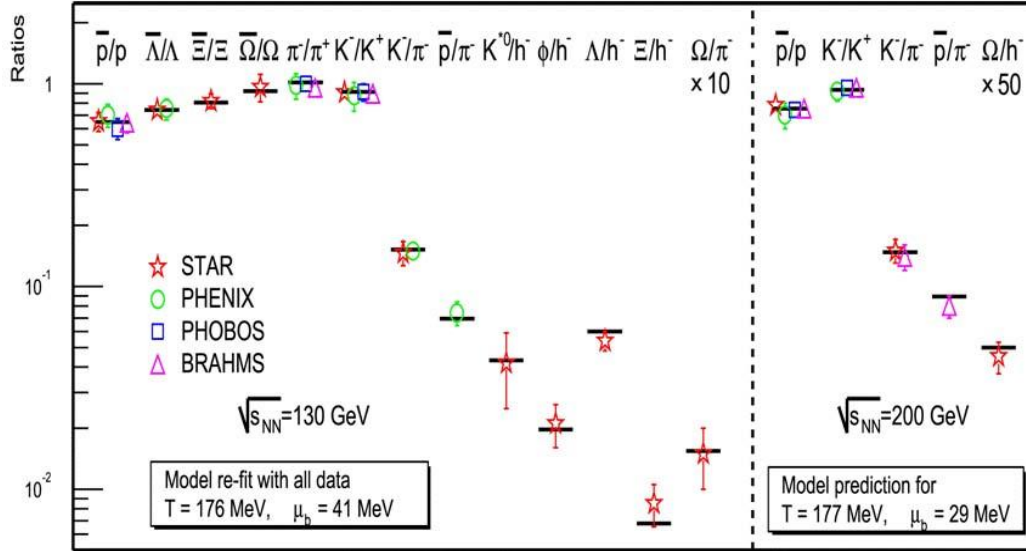


Figure 1.4: Ratios of measured yield of various particles in  $\sqrt{s_{NN}} = 130$  GeV and 200 GeV, compared with the statistical thermal model [11].

isospin quantum numbers of the particles  $i$ . In this model, the temperature  $T$  and the baryochemical potential  $\mu_B$  are the two independent parameters. Figure 1.4 shows the particle ratios measured in Au+Au collisions at  $\sqrt{s_{NN}} = 130$  GeV and 200 GeV. The results are well reproduced by the thermochemical model with  $T = 176$  MeV and  $\mu = 41$  MeV for  $\sqrt{s_{NN}} = 130$  GeV,  $T = 177$  MeV and  $\mu = 29$  MeV for  $\sqrt{s_{NN}} = 200$  GeV/c. As described in Chapter 1.1, the lattice QCD predicts that the phase transition from a hadronic phase to QGP phase, which takes place at a temperature of approximately 170 MeV. The temperature obtained from particle ratios with thermochemical models has a good agreement with the prediction. It indicates that the medium created at RHIC is achieved chemical equilibrium.

### 1.3.2 Kinematical equilibrium and the collective flow

#### Radial flow

Transverse momentum spectra is one of the most basic measurement not only in heavy ion collisions but also proton-proton or proton-nucleus collisions to study the particle productions in the collisions. If the system created by collisions is a thermal equilibrium state of hadron gas, the momentum distribution of particles should follow Maxwell-Boatman distribution and the transverse momentum distribution is given as an exponential function of transverse mass  $m_T (= \sqrt{p_T^2 + m^2})$  as

$$\frac{1}{m_T} \frac{dN}{dm_T} = A \exp\left(\frac{-m_T}{T}\right), \quad (1.3)$$

where  $A$  is a constant and  $T$  is the inverse slope parameter of the distribution. It is known that the transverse momentum spectra is well described with the equation in the region  $p_T < 2.0$  GeV/ $c$  and it is called  $m_T$  *scaling*. The inverse slope parameter  $T$  corresponds to the temperature of the system at the kinetic freeze-out. In high energy  $p + p$  collisions the slope parameters are independent of particle species [12] ( $T_\pi \sim T_K \sim T_p \sim 150$  MeV). On the other hand, it has been observed that these parameters depend on the particle mass in heavy ion collisions [13] [14]. Fig.1.5 shows inverse slope parameter  $T$  as a function of particle mass measured in  $p + p$ , S+S and Pb+Pb collisions [15]. As we see, the slope parameters measured in S+S and Pb+Pb collisions are not independent of particle species. The feature of the slope parameters in heavy ion collisions is that the larger mass particle have larger slope parameter ( $T_\pi < T_K < T_p$ ) and it also increases with mass of collided nucleus. The feature indicates that the existence of the outward collective motion (collective radial flow). Most successful description of the difference slope parameters in heavy ion collisions is given by a model including the common transverse expanding velocity (collective flow) field together with a moderate temperature of a thermalized system. If the system is a expanding system, particles have a common transverse expanding velocity, not only their thermal motion. In the framework, the slope parameter is given as;

$$T \sim T_{fo} + \frac{1}{2}m\beta^2 \quad (1.4)$$

where  $T_{fo}$  is the thermal temperature,  $m$  is particle mass and  $\beta$  is the collective velocity. At RHIC we have obtained  $T_{fo} = 177.0 \pm 1.2$  and  $\beta = 0.48 \pm 0.07$  in most central Au+Au collisions at  $\sqrt{s_{NN}} = 200$  GeV [16] [17] from the fitting of transverse momentum spectra for identified particles ( $\pi$ , K, p).

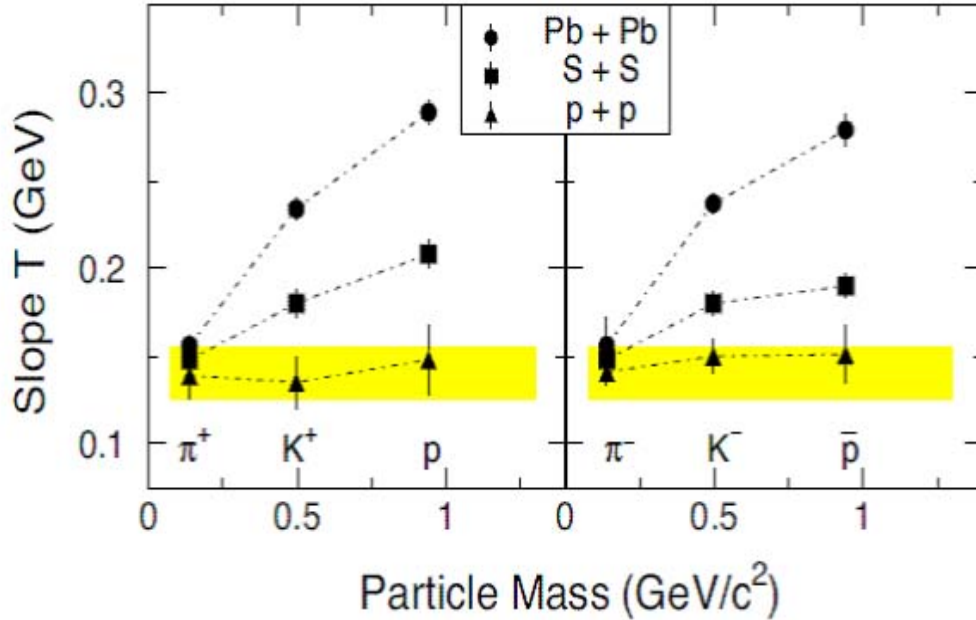


Figure 1.5: Inverse slope parameter  $T$  as a function of particle mass. They are compared at mid-rapidity in  $p + p$ , S+S and Pb+Pb collisions [15].

### Azimuthal anisotropy

As describe in the previous section, the measurement of transverse momentum spectra gives us information about the existence of the outward collective motion. The measurement of particle production in the azimuthal space can be more information about collective motion in heavy ion collisions. The azimuthal distribution of the particles is very influenced by the mean free path. When the mean free path is larger than the size of the system, the particle emission is isotropic in the azimuthal space. On the other hand, the mean free path is much shorter than the size of the system (thus hydrodynamical description apply), the emission pattern is affected by the shape of the system. In heavy ion collisions at RHIC, the mean free path is about  $10^{-1} fm$  and it is smaller than the system size ( $R = 6 fm$ ). In the hydrodynamical framework, the driving force of the collective flow is the pressure gradient,  $\Delta P$ . In the non-central collisions, the initial medium shape created by the collisions is an almond like shape (Fig. 1.6). If the medium becomes equilibrium (or local equilibrium), the pressure in  $x - z$  plane is larger than  $y$  direction. Therefore the particles produced by collisions are emitted more to the  $x - z$  plane than to  $y$  direction and it is measured as an anisotropy in the azimuthal distribution. Thus the initial spatial anisotropy in the early stage

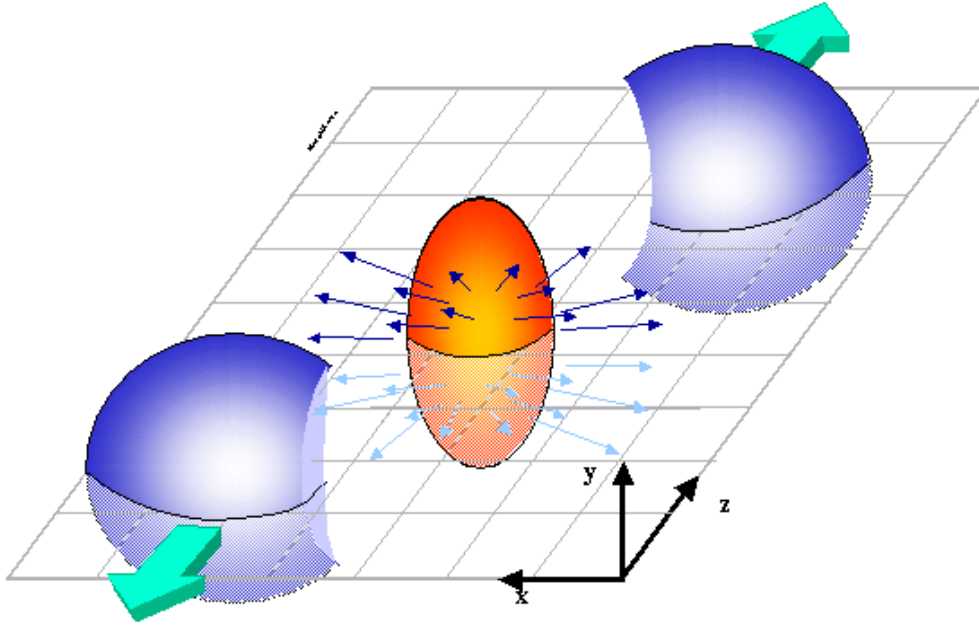


Figure 1.6: An illustration of non-central Au-Au collisions. The plane defined as the direction of the impact parameter ( $x$ ) and direction of the beam axis ( $z$ ) is called “reaction plane”.

of the collisions transfer to the momentum space anisotropy in the final stage. Therefore the azimuthal anisotropy is sensitive to the early stage of the collisions, in contrast to transverse momentum spectra which is sensitive to the expanding velocity in the final stage of the collision.

Experimentally the azimuthal anisotropy has been studied using Fourier expansion of the azimuthal distribution. The azimuthal anisotropy is defined by

$$\frac{dN}{d\phi} = N_0 \left\{ 1 + \sum_n 2v_n \cos(n(\phi - \Psi_{R.P.})) \right\}, \quad (1.5)$$

where  $N_0$  is a normalization constant,  $\phi$  is the azimuthal angle of particles, and  $\Psi_{R.P.}$  is the direction of the nuclear impact parameter (“reaction plane”) in a given collision. The harmonic coefficients,  $v_n$ , indicate the strength of the  $n^{\text{th}}$  anisotropy. Especially the second harmonic coefficient of the Fourier expansion of the azimuthal distribution is called “elliptic flow” and it is sensitive to the early stage of the collisions [18]. Indeed,  $v_2$  which is the strength of the elliptic flow scales with the geometrical eccentricity which is defined as;

$$\epsilon = \frac{\langle y^2 \rangle - \langle x^2 \rangle}{\langle y^2 \rangle + \langle x^2 \rangle}. \quad (1.6)$$

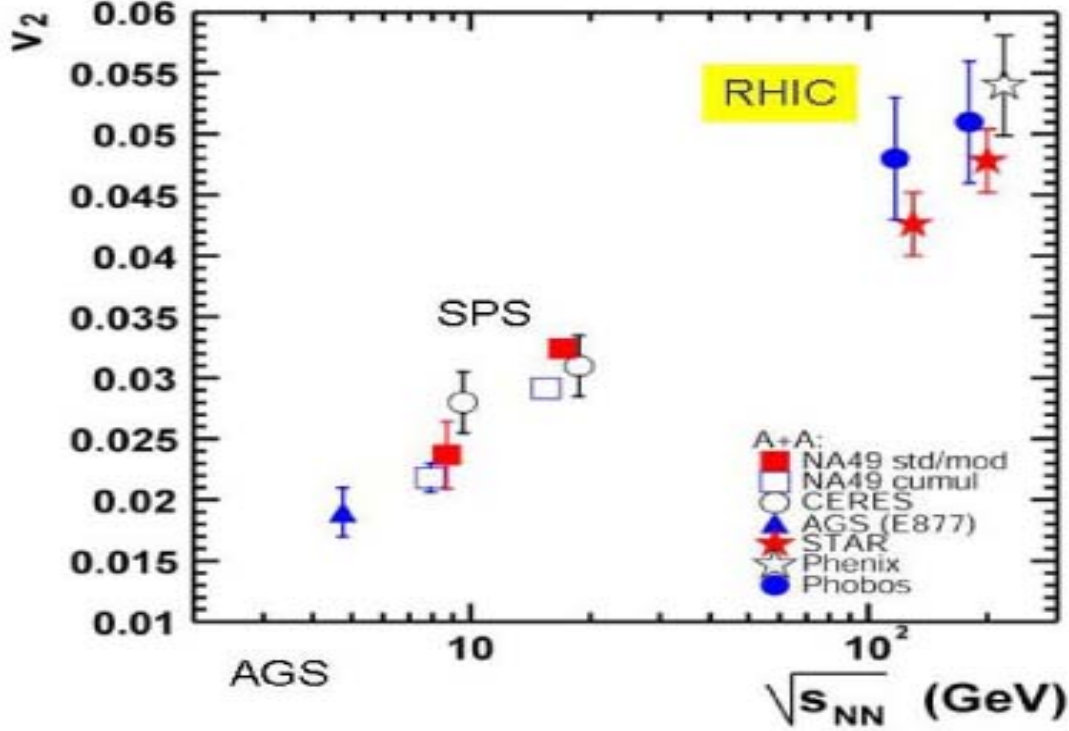


Figure 1.7: Beam energy dependence of  $v_2$  measured at AGS, SPS and RHIC.

Elliptic flow has been measured in the early stage of the experiment of heavy ion collisions. Figure 1.7 shows the energy dependence of  $v_2$  measured at AGS, SPS and RHIC experiments. At RHIC, strong elliptic flow has been measured and the value of  $v_2$  is 2 times larger than  $v_2$  measured at SPS. The transverse momentum ( $p_T$ ) dependence of  $v_2$  has been measured for identified particles at RHIC [19, 20, 21, 22]. Figure 1.8 shows the  $p_T$  dependence of  $v_2$  for  $\pi, K, p$ . In low  $p_T$  region ( $< 1.5$  GeV/c),  $v_2$  increases with  $p_T$  and show the clear mass dependence,

$$v_2^\pi > v_2^K > v_2^p. \quad (1.7)$$

This behavior is consistent with a hydrodynamical model calculation [23] which is shown as solid lines in Fig. 1.8. The model assumes that the initial time when the local equilibrium is occurred is  $0.6$  fm/c and the phase transition is first-order phase transition with a freeze-out temperature of  $120$  MeV. The agreement suggests as evidence that the collective motion develops in the very early stages of the reaction. In addition, the model assumes that the viscosity of the matter is very low, therefore the property of the matter created in Au+Au

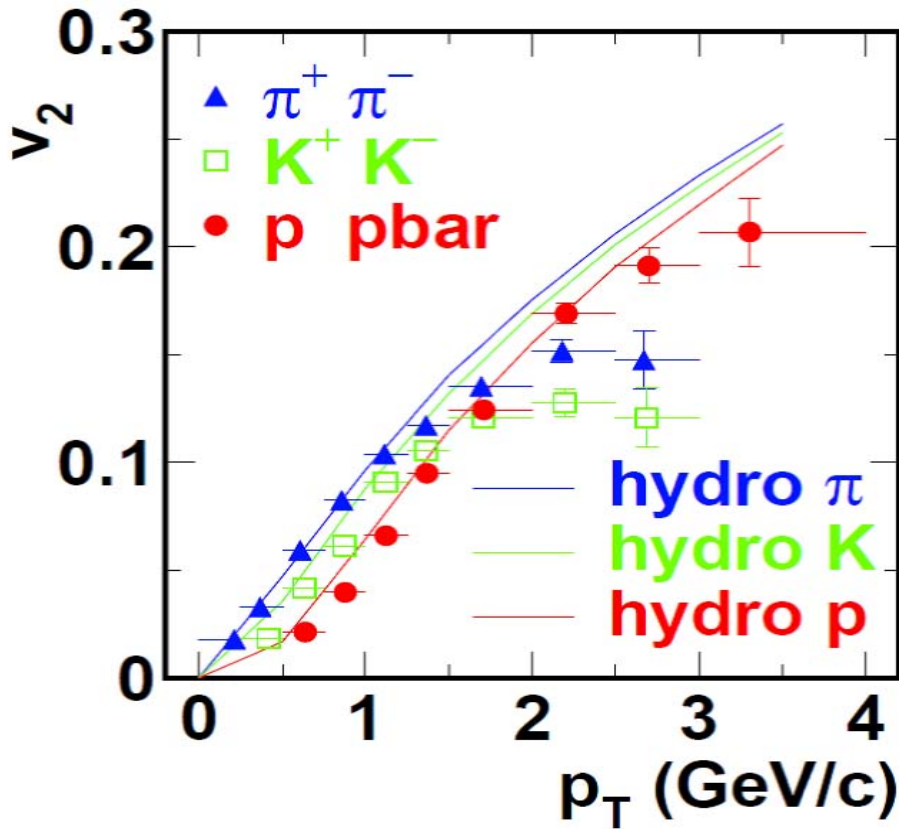


Figure 1.8: Identified particle ( $\pi$ ,  $K$ ,  $p$ )  $v_2$  as a function of  $p_T$  [19]. The lines in the figure are the hydrodynamical model calculation. [23]

collisions is thought like a liquid. The other feature of  $v_2$  for identified particles is that  $v_2$  for meson,  $\pi$  and  $K$ , is saturated around  $p_T = 2.0$  GeV/c, on the other hand  $v_2$  for baryon,  $p$ , is still increasing. The difference between meson  $v_2$  and baryon  $v_2$  is well explained by a quark coalescence model. The detail is described in the 1.5.

## 1.4 Suppression of high $p_T$ particle

One of the good probes for studying the medium is to measure high  $p_T$  particles. In the RHIC energy range, the dominant process of the particle production with  $p_T > 2.0$  GeV/c in nucleon-nucleon collisions is hard scattering. Typically, particles with  $p_T > 2$  GeV/c are produced from states with two roughly back-to-back jets which are the result of scattering of constituents of the nucleons (partons) as described by the perturbative QCD. The hard scattering will occur before the medium creation, therefore the high  $p_T$  particles propagate

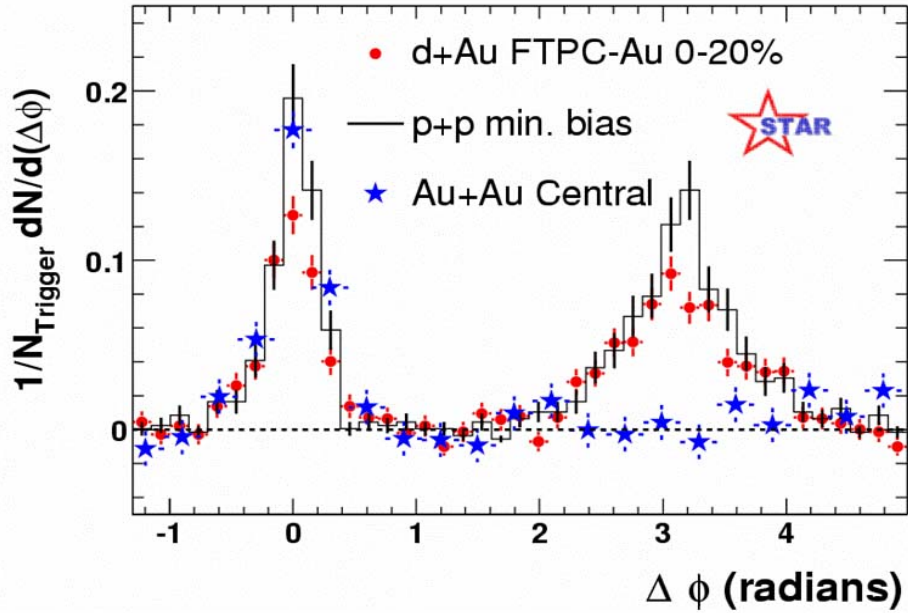


Figure 1.9: Comparison of two-particle azimuthal angular correlations of charged particles for central Au + Au, central  $d + Au$  and  $p + p$  collisions, where  $N_{\text{Trigger}}$  is the number of high  $p_T$  particles.

through the medium. It has been predicted that the high  $p_T$  particles are suppressed compared with  $p + p$  collisions at RHIC due to the energy loss of partons, which called "jet quenching".

One of the methods to study the suppression of high  $p_T$  hadrons is to measure two particle azimuthal angular correlations. Due to the high  $p_T$  particles are produced from back-to-back jets, we can expect peaks around  $\Delta \phi \sim 0^\circ$  (nearside) and  $\Delta \phi \sim 180^\circ$  (away side). Figure 1.9 shows the two particles ( $4 < p_T < 6$ ) azimuthal angular correlations ( $\Delta \phi$ ) for inclusive charged hadrons measured in  $p + p$ ,  $d+Au$  and  $Au+Au$  in 200 GeV collisions [24]. Two particles are chosen such that one "trigger" particle and the other "associated" particles. In this plot, other sources of angular correlations, elliptic flow, are subtracted. We can see clear peaks around at  $\Delta \phi \sim 0^\circ$  in  $p + p$ ,  $d+Au$  and  $Au+Au$  which is expected from the high  $p_T$  particles production. On the other hand, the away side peak at  $\Delta \phi \sim 180^\circ$  is



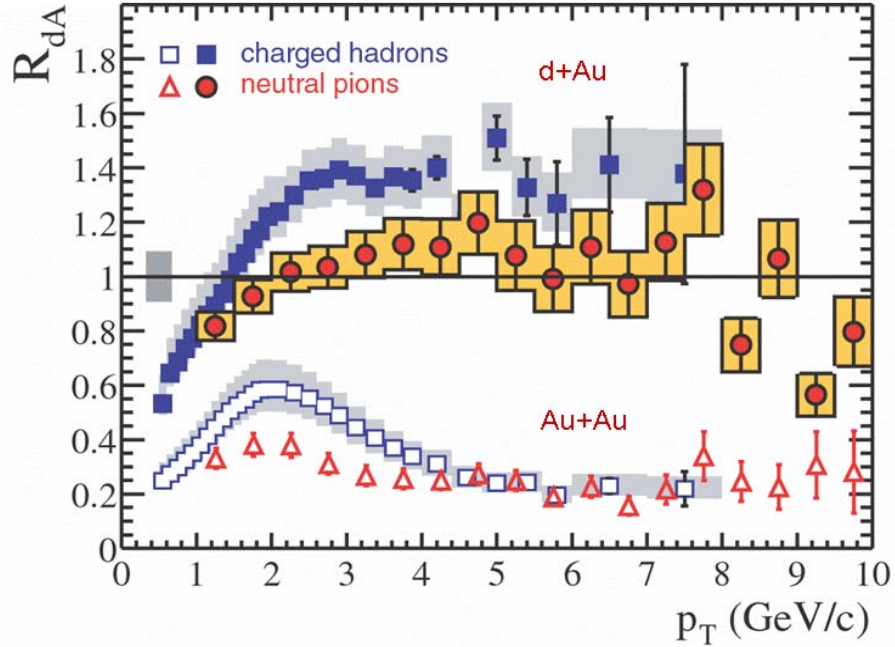


Figure 1.10: Nuclear modification factor measured for  $\pi^0$  and charged particle in Au + Au collisions ( $R_{AA}$ ) and in  $d + Au$  collisions ( $R_{dAu}$ ) in  $\sqrt{s_{NN}} = 200$  GeV as a function of  $p_T$  [25]. The bands around the data points show systematic errors, while the shade band around unity indicates the normalization uncertainty.

vanished in Au+Au collisions, while  $p + p$  and  $d+Au$  collisions make peaks at  $\Delta \phi \sim 180^\circ$ . The different results between Au+Au and  $d+Au$  indicate that the suppression of the away side yields in Au+Au is due to the final state interactions with the medium created in Au+Au collisions. Because the same suppression of the away side yields should be also observed in  $d+Au$  if it is due to the initial state interaction.

The other method to study the suppression is to compare yields between Au+Au collisions and  $p + p$  collisions. The hard scattering cross section usually have a small cross-section (point like), therefore the yields are proportional to the number of a binary scaled nucleon-nucleon ( $N + N$ ) collisions,  $N_{coll}$ . The yield ratio between Au+Au and  $p + p$ , nu-



clear modification factor  $R_{AA}$ , is expressed as;

$$R_{AA} = \frac{d\sigma_{Au+Au}}{\langle N_{binary} \rangle \times d\sigma_{p+p}}, \quad (1.8)$$

where  $d\sigma_{Au+Au}$  and  $d\sigma_{p+p}$  is the cross section in Au+Au and  $p + p$  collisions.  $\langle N_{binary} \rangle$  is the number of primary nucleon-nucleon collisions which is estimated by using Glauber model. If there is no medium effect, the rate of hard processes scales linearly with the number of binary collisions,  $\langle N_{binary} \rangle$ . Therefore  $R_{AA}$  is unity ( $R_{AA} = 1.0$ ). Figure 1.10 shows the  $R_{AA}$  for charged hadron and neutral pion in Au+Au collisions at  $\sqrt{s_{NN}} = 200$  GeV, together with the nuclear modification factor measured in  $d$ +Au collisions ( $R_{dAu}$ ) at  $\sqrt{s_{NN}} = 200$  GeV [25]. The  $R_{dAu}$  is consistent with unity for neutral pions and greater than unity for charged particles at high  $p_T$  region. The  $R_{dAu}$  is greater than unity means the yield is enhanced compared to that in  $p + p$  collisions. It is known that the particle production in  $p$ +A collisions is enhanced compared to  $p + p$  collisions due to "Cronin effect" [26]. On the other hand,  $R_{AA}$  is much smaller than unity in Au+Au collisions. It means that the yields of Au+Au are suppressed. Such the suppression is not observed in  $d$ +Au collisions, the suppression in Au+Au is due to the final state interactions. The high  $p_T$  particle suppression is thought that partons lose their energy through gluon bremsstrahlung [27] in the dense matter, rescuing the momentum and depleting the yield [28] [29].

## 1.5 Quark coalescence/recombination

### 1.5.1 Baryon excess

One of the most striking observations in RHIC is that the yield of proton (anti-proton) is larger than that of pion at intermediate  $p_T$  region ( $2 < p_T$  (GeV/c)  $< 5$ ). Figure 1.11 shows  $p/\pi$  ratio as a function of  $p_T$  for central (0-10 %), mid-central (20-40 %) and peripheral (60-92 %) collisions [17] [30]. As we see, the ratios increase with centrality and the ratio in the central collisions is enhanced by almost a factor of three compared with the peripheral results. The dashed and dotted lines are proton and anti-proton to pion ratio in gluon and in quark jets [31]. In the high  $p_T$  ( $p_T > 3.0$  GeV/c), these ratios are consistent with the ratio measured in peripheral Au+Au collisions. Thus the  $p/\pi$  ratio at the peripheral Au+Au collisions can be well describe by the fragmentation. On the other hand, the ratio at most central collisions is much larger than the ratio which is expected by the fragmentation. This result indicates that there is an additional mechanism for hadron production at the intermediate  $p_T$  region.

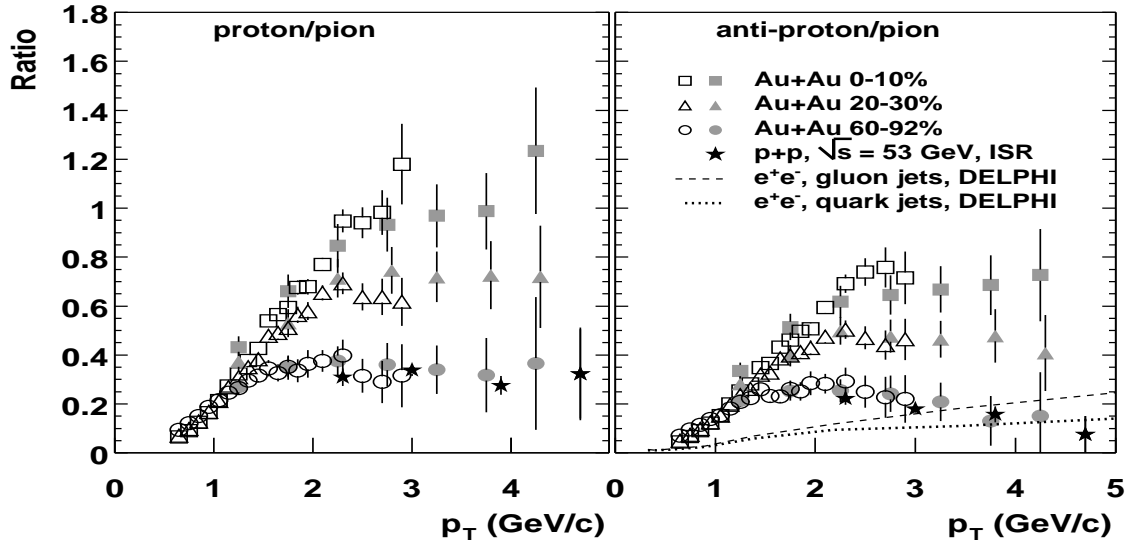


Figure 1.11:  $p/\pi$  ratio as a function of  $p_T$  for central (0-10 %), mid-central (20-40 %) and peripheral (60-92 %) collisions [30]. The dashed and dotted lines are proton and pion ratio in gluon and in quark jets [31].

## 1.5.2 Quark coalescence model

A quark coalescence (recombination) model is one of the models for hadron production. In the model, hadrons are produced by valence quarks from the thermal medium when they are close together in the phase space. In the framework, mesons are formed from coalescence of a quark and anti-quark and baryon are formed of three quarks. If the model can explain the data, it implies that there is a larger thermalized source of quarks and anti-quarks and it is a strong evidence for a QGP formation at RHIC [32].

In a simplified version of the model, the production rates of mesons and baryons are evaluated as,

$$E \frac{d^3 N_M}{d^3 p} \propto \int dx w_a(x p_T) \bar{w}_b((1-x)p_T) |\Psi_{ab}|^2, \quad (1.9)$$

$$E \frac{d^3 N_B}{d^3 p} \propto \int dx dx' w_a(x p_T) w_b(x' p_T) w_c((1-x-x')p_T) |\Psi_{abc}|^2, \quad (1.10)$$

where  $w(p_T)$  is a parton distribution function,  $x$  is a fraction of the momentum and  $\Psi_{ab}$  ( $\Psi_{abc}$ ) is a meson (baryon) wave function. In case of an equal momentum fraction *i.e.* the effective masses of constituent quarks are similar,  $x = 1/2$  for mesons and  $x = x' = 1/3$  for baryons and above equations can be written as;

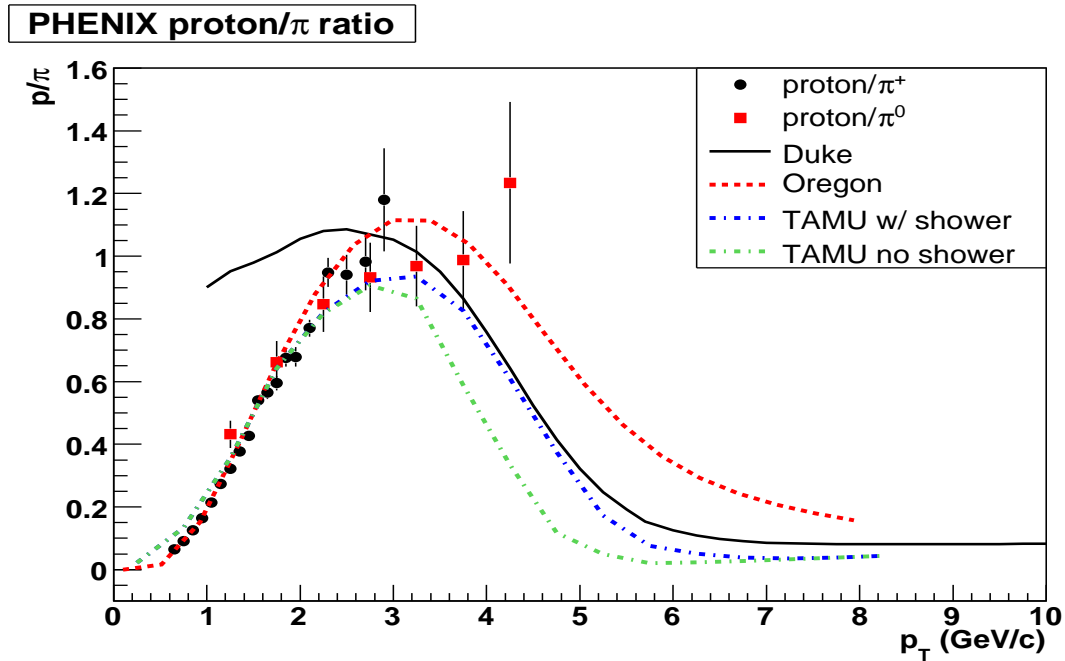


Figure 1.12:  $p/\pi$  ratio measured by PHENIX [30] and quark coalescence model calculations for the comparison. This picture is taken from [5].

$$\frac{d^3 N_M}{d^3 p} = C_M w_a(p_T/2)^2, \quad (1.11)$$

$$\frac{d^3 N_B}{d^3 p} = C_B w_a(p_T/3)^3, \quad (1.12)$$

where  $C_M$  and  $C_B$  correspond to the coalescence probabilities for mesons and baryons, respectively [33]. The coalescing parton distribution is assumed to be exponential, thermal. Under this assumption, lower momentum quarks are much more abundant than those for the high  $p_T$  quarks. As the result, the chance for lower  $p_T$  quarks to recombine is much higher than the chance for higher  $p_T$  quarks from a hard scattering to fragment into the final state hadrons. Thus baryons at moderate  $p_T$  are enhanced relative to mesons as their transverse momentum is the sum of three quarks rather than two. Figure 1.12 shows several quark coalescence model calculations for proton and pion ratio compared to the data as a function of  $p_T$  measured at PHENIX [30]. These calculations well reproduce the strong enhancement of proton at intermediate  $p_T$ .

The model also predicts that the elliptic flow of hadrons reflect the elliptic flow of constituent quarks. The parton distribution function ( $w(p_T)$ ) for  $v_2$  is given as;

$$w = 1 + 2v_{2,q} \cos(2\phi), \quad (1.13)$$

Then we can obtain following equation for meson and baryon  $v_2$  as;

$$v_{2,M} = 2v_{2,q}(p_T/2), \quad (1.14)$$

$$v_{2,B} = 3v_{2,q}(p_T/3). \quad (1.15)$$

where  $v_{2,q}$  is quark  $v_2$ . The model predicts that elliptic flow for mesons and baryons are scaled with the number of constituent quarks. Fig. 1.13 shows that  $v_2$  as a function of  $p_T$  scales via the number of quarks, that is,  $v_2/n$  as a function of  $p_T/n$  where  $n$  is the number of constituent quarks plus anti-quarks ( $n = 2$  for meson and  $n = 3$  for baryon). As we can see,  $v_2$  of identified hadrons after scaling with number of quarks falls on same curve. This suggests that the  $v_2$  already develops in the partonic phase for hadrons which made of light quarks.

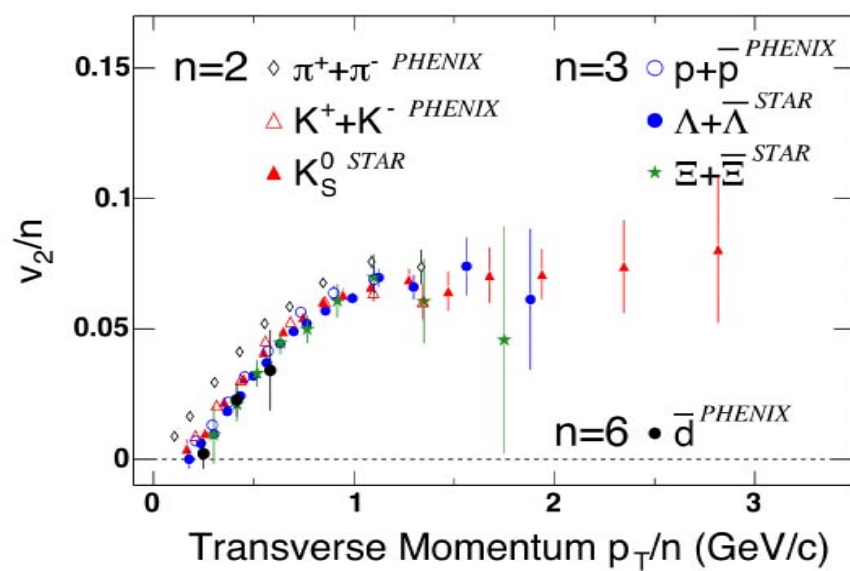


Figure 1.13:  $v_2/n$  as a function of  $p_T/n$  where  $n$  is the number of constituent quarks plus anti-quarks ( $n = 2$  for meson and  $n = 3$  for baryon).

## 1.6 Charm quark production in RHIC

Charm quark is believed to be produced in initial collisions via gluon fusion. Due to the large mass of charm quark ( $\sim 1.5 \text{ GeV}/c^2$ ), the charm production rate is calculated by pQCD [34] [35]. Measurements of charmed hadron,  $D$  mesons, are good tools for the study of charm production. But the directly measurement and the reconstruction of  $D$  meson ( $D^0 \rightarrow K^- \pi^+$ ) is difficult due to the small short lifetime ( $D^0 \sim 124 \mu\text{m}$ ), the small yield of charm quarks and the large background of other hadrons. Table 1.2 shows the main decay modes of the  $D$  meson. In PHENIX experiment charm quark production has been studied by measuring single electrons from semileptonic decays of charmed particles at mid-rapidity region ( $|\eta| < 0.35$ ). Electrons from charm were observed at the CERN-ISR experiment in early 1970 [36] [37] before charm discovery and later it has interpreted as a signal of open charm [38]. Thus the measurement of single electron is also a powerful tool to study the charm production in heavy ion collisions. PHENIX has two independent techniques, “cocktail” method and “conversion” method to remove electron backgrounds from other sources, mainly conversions and light hadron decays. In the cocktail method, background electrons are calculated by a Monte Carlo simulation and they are subtracted from inclusive electrons. In the converter method, background electrons are experimentally determined with and without a converter that increases/decreases background electrons. Figure 1.14 shows the invariant differential cross section of electrons from heavy flavor, charm and beauty, in  $p + p$  collisions at  $\sqrt{s_{NN}} = 200 \text{ GeV}$  measured at PHEXNIX experiment [39]. The curves in the figure are a fixed-order-plus-next-leading-log (FONLL) pQCD calculation [40]. The bottom figure shows the ratio of the data and the FONLL. The upper and lower curves are the theoretical upper and lower limits of the FONLL. The pQCD calculation describes the cross sections of heavy flavor decay electrons within uncertainties.

Decay mode	branching ratio
$D^0 \rightarrow K^- \pi^+$	3.80 %
$D^0 \rightarrow e^+ + X$	6.87 %
$D^\pm \rightarrow e^\pm + X$	17.2 %

Table 1.2: The branching ratio of  $D$  meson decay

In the relativistic heavy ion collisions there would be three stage of charm quark productions if the matter is thermalized: (1) the first stage is the initial collisions which is same as the production in  $p + p$  collisions, (2) the second stage is the pre-equilibrium production from secondary parton cascade, and (3) the third stage is the thermal production. Figure

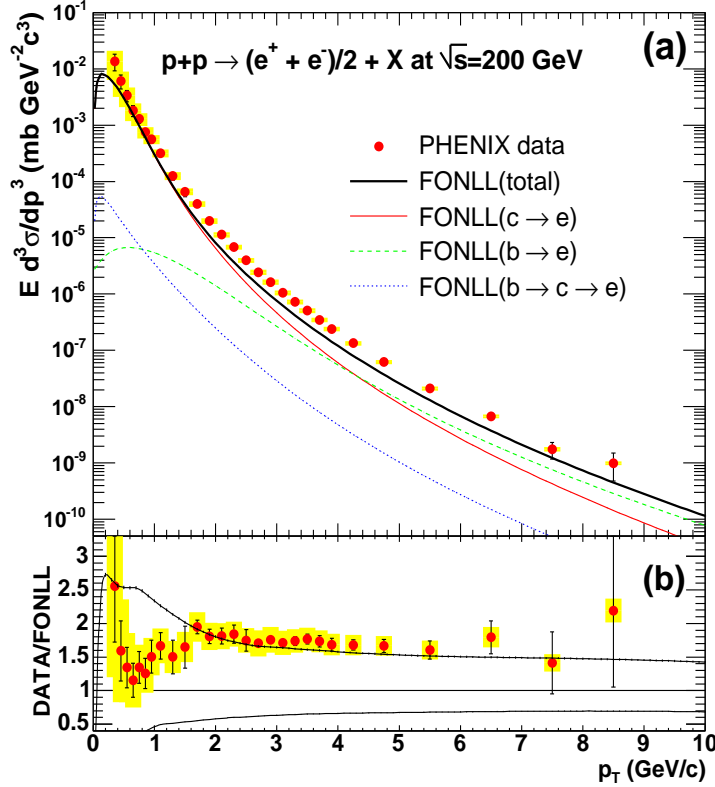


Figure 1.14: (a) Invariant differential cross section of electrons from heavy flavor, charm and bottom, in  $p + p$  collisions at  $\sqrt{s_{NN}} = 200$  GeV measured at PHENIX experiment [39]. The curves are the FONLL calculations. (b) Ratio of the data and the FONLL. The upper and lower curves are theoretical upper and lower limit of the FONLL.

1.15 shows the theoretical prediction for charm quark productions in Au+Au collisions at  $\sqrt{s_{NN}} = 200$  GeV [41]. The theory predicts that the most largest contribution is also initial collisions in Au+Au collisions and the thermal production is very small even if the matter is thermalized. In Au+Au collisions the total yield of heavy-flavor decay electrons was found to scale with the number of nucleon-nucleon collisions as expected for pQCD [42]. Thus the dominant process of charm quark production in Au+Au collisions is also initial collisions via gluon fusion.

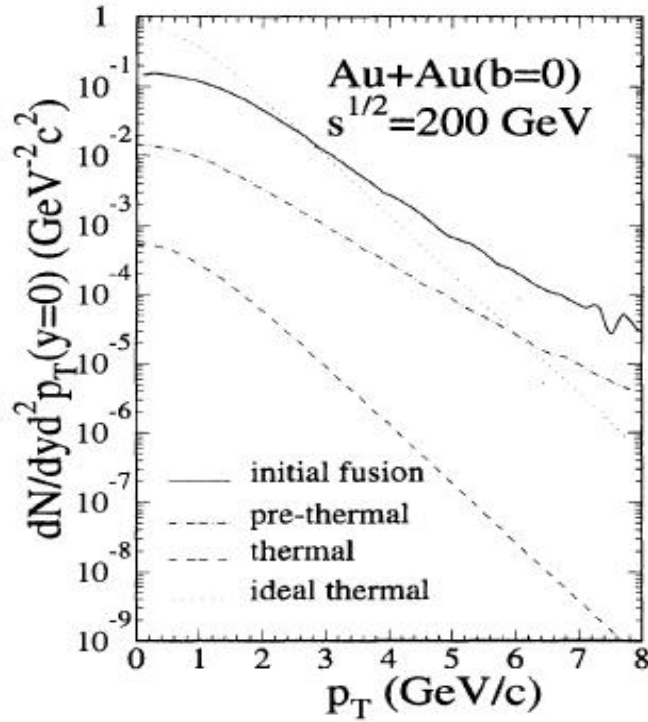


Figure 1.15: Theoretical prediction of  $p_T$  distributions of initial (solid), prethermal (dot-dashed) and thermal (dashed) charm production for central Au+Au collisions at RHIC energy,  $\sqrt{s_{NN}} = 200$  GeV [41].

## 1.7 Thesis motivation

As reviewed in this chapter, there are various hints for QGP formation in Au+Au collisions at  $\sqrt{s_{NN}} = 200$  GeV. The initial energy density of the medium created in Au+Au collisions is about  $15 \text{ GeV}/\text{fm}^3$  and the value is large enough to create the QGP, which  $1.0 \text{ GeV}/\text{fm}^3$  predicted by the lattice QCD. The yield of high  $p_T$  particles is strongly suppressed with regard to the yield in  $p + p$  collisions ( $R_{AA} < 1.0$ ). The origin of the suppression is thought that energy loss of partons in the dense medium. Thus the density of the medium would be very high. The particle ratios are well reproduced by a statistical thermal model calculation, which assumed chemical freeze-out temperature of 170 MeV. Collective flow, especially a large elliptic flow has been observed. The strength of elliptic flow,  $v_2$ , for various particles has been measured. The  $v_2$  for identified particles shows a clear mass dependence and it is well explained by the hydrodynamical model calculation which assumes a very early time thermal equilibrium ( $\tau = 0.6 \text{ fm}/c$ ) and very low viscosity. These  $v_2$  are scaled with the



number of quarks. It indicates that partonic collectivity has been developed for light quarks in Au + Au collision at RHIC. If charm quarks also flow same as light quarks, it indicates a quark level thermalization is achieved at RHIC energies. Because it is needed that charm quarks are scattered over and over again due to their large mass. Thus it would be a strong evidence of QGP formation at RHIC.

In this thesis we study elliptic flow, which is defined as a second harmonic of the Fourier expansion of the azimuthal distribution, of charm quark via electron measurement. We measured the transverse momentum dependence of the azimuthal anisotropy parameter  $v_2$  for electrons at mid-rapidity ( $|\eta| < 0.35$ ) with the PHENIX detector in Au+Au collisions at  $\sqrt{s_{NN}} = 200$  GeV during the fourth experiment period at RHIC run (2004 - 2005). From the result, we have measured the  $v_2$  of electrons from heavy flavor decay after subtraction of the  $v_2$  of electrons from other sources such as photon conversions and Dalitz decay from light neutral mesons. Based on the result, we discuss charm quark  $v_2$  in Au+Au collisions at  $\sqrt{s_{NN}} = 200$  GeV.

## Chapter 2

# The PHENIX experiment

This analysis is based on the data measured at the RHIC-PHENIX experiment. In this chapter, the Relativistic Heavy Ion Collider complex and PHENIX detector system are presented.

### 2.1 The Relativistic Heavy Ion Collider (RHIC)

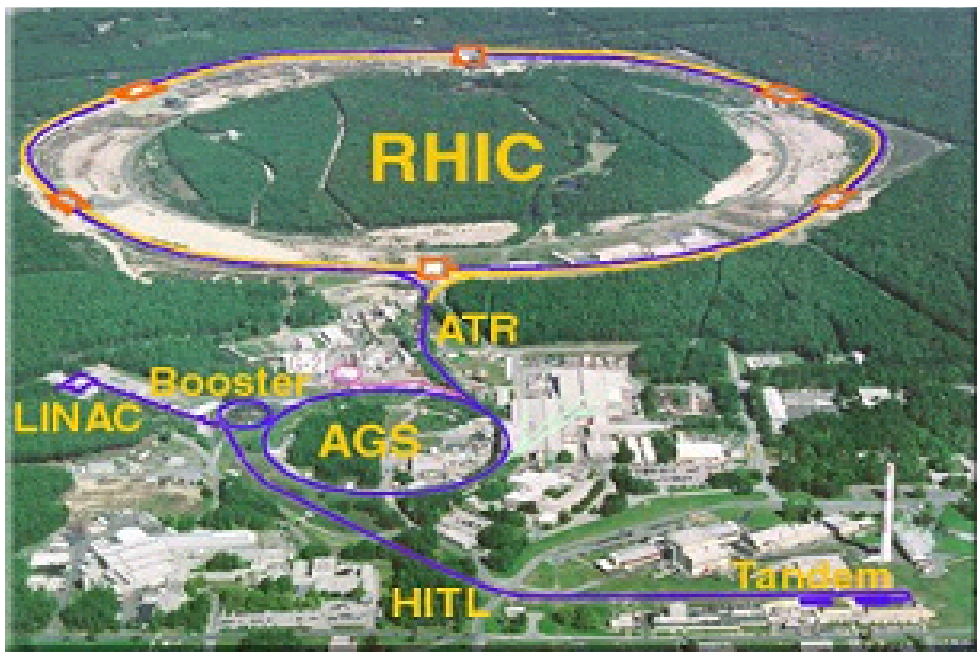


Figure 2.1: A picture of RHIC complex.

The Relativistic Heavy Ion Collider (RHIC) at BrookHaven National Laboratroy is the

Circumference of rings (km)	3.834
No. Intersection Regions	6
No. Bunches/ring	60
Bunch Spacing(nsec)	213
No. Particles/Bunch	$1 \times 10^9$
Top Energy(GeV/u)	100
Luminosity, average( $cm^{-2}sec^{-1}$ )	$2 \times 10^{26}$
Lifetime(h)	10

Table 2.1: RHIC performance for Au ions

world's first head-on collider for heavy ions. RHIC consists of two rings which are made up of 1,740 superconduction magnets and each ring has about 3.8 km circumference. Any nuclear species from proton to Au can be accelerated and collided at interaction points at RHIC. The maximum energy is 100 GeV per nucleon for Au ions and the center of mass energy ( $\sqrt{s_{NN}}$ ) is 200 GeV. The stored beam lifetime for Au is expected to be approximately 10 hours. The designed luminosity of RHIC for Au+Au is about  $2 \times 10^{26} cm^{-2} sec^{-1}$  at top energy. A total of 60 bunches are injected into each ring. Table 5.1 shows the summary of RHIC parameters.

Figure 2.2 shows the RHIC acceleration scenario for Au. Tandem Van de Graff accelerators, the Booster synchrotron, and the Alternating Gradient Synchrotron (AGS) serve as the injector for RHIC. The negative Au ions (-1) injected to Tandem Van de Graff are accelerated at the kinematic energy of 1MeV/u and with  $Q=+12$  charge state. Exiting from Tandem Van de Graf, ions are further stripped to the charge state +32. Then they are injected into the Booster synchrotron through heavy ion transfer line (550m). The Booster synchrotron accelerates the beam up to 95 MeV/u. In the Booster to AGS line, the ions are stripped to charge state +77 and injected to AGS. At AGS the beam is accelerated to 10.8 GeV/u. Then the ions are stripped to charge state +79 at the start of AGS to the RHIC transfer line tunnel. The intensity of the beam injected to RHIC is  $1 \times 10^9$  ions/bunch. Finally, the beam is accelerated to 100.0 GeV/u at RHIC. Four experiments (PHOBOS, BRAHMS, STAR and PHENIX) are instrumented at the collision point. The detail of PHENIX is described in the next section.

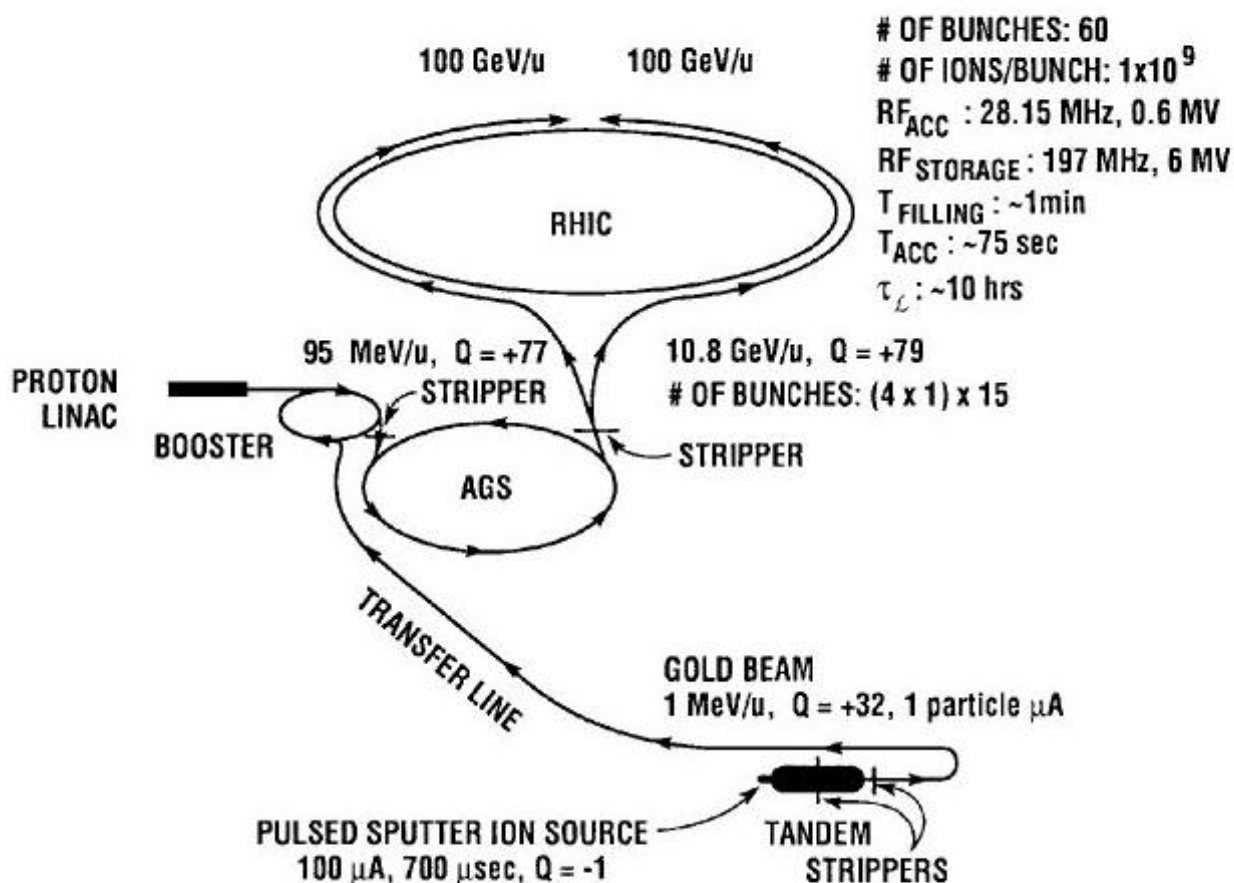


Figure 2.2: RHIC acceleration scenario for gold. The tandem Van de Graaff accelerators, the Booster synchrotron, and the Alternating Gradient Synchrotron (AGS) serve as the injector for RHIC.

Component	$\Delta\eta$	$\Delta\phi$	Purpose and Special Feature
Magnet: central(CM)	$ \eta  < 0.35$	$360^\circ$	Up to $1.15 \text{ T} \cdot \text{m}$ .
muon (MMS)	-1.1 to -2.2	$360^\circ$	$0.72 \text{ T} \cdot \text{m}$ for $\eta=2$
muon (MMN)	1.1 to 2.4	$360^\circ$	$0.72 \text{ T} \cdot \text{m}$ for $\eta=2$
BBC	$3.0 <  \eta  < 3.9$	$360^\circ$	start timing, fast vertex
ZDC	$\pm 2 \text{ mrad}$	$360^\circ$	Minimum bias trigger
DC	$ \eta  < 0.35$	$90^\circ \times 2$	Good momentum and mass resolution $\Delta m/m = 0.4\%$ at $m=1.0\text{GeV}$
PC	$ \eta  < 0.35$	$90^\circ \times 2$	Pattern recognition, tracking for nonbend direction
RICH	$ \eta  < 0.35$	$90^\circ \times 2$	Electron identification
TOF	$ \eta  < 0.35$	$45^\circ$	Good hadron identification, $\sigma_{TOF} = 100\text{ps}$
PbSc EMCAL	$ \eta  < 0.35$	$90^\circ + 45^\circ$	For both calorimeters, photon and electron detection
PbGl EMCAL	$ \eta  < 0.35$	$45^\circ$	Good $e^\pm/\pi^\pm$ separation $p > 2.0\text{GeV}/c$ by EM shower and $p < 0.35\text{GeV}/c$ by ToF $K^\pm/\pi^\pm$ separation up to $1 \text{ GeV}/c$ by ToF
$\mu$ tracker:( $\mu\text{TS}$ )	-1.15 to -2.25	$360^\circ$	Tracking for muons
$\mu$ identifier:( $\mu\text{IDS}$ )	-1.15 to -2.25	$360^\circ$	Steel absorbers and Iarocci tubes for muon/hadron separation
( $\mu\text{IDN}$ )	-1.15 to -2.44	$360^\circ$	

Table 2.2: Summary of PHENIX detector subsystems

## 2.2 Overview of PHENIX experiment

A prime goal of PHENIX experiment is to detect QGP and study its physical properties. In order to achieve the goal, PHENIX is designed to measure various particle species produced by the collisions especially photons, leptons and hadrons. These measurement are done with 11 independent sub-systems.

Figure 2.3 shows the setup of the PHENIX experiment in Run4. The acceptance of PHENIX is shown in Fig. 2.4. PHENIX consists of four parts of spectrometers arms and a set of global detectors. The spectrometers around mid-rapidity are called central arms (west and east arms) and those around forward rapidity are called muon arms. Table 2.2 shows the summary of the PHENIX detectors. The global detectors consist of Beam-Beam-Counters (BBCs) and Zero-Degree Calorimeters (ZDCs). These detectors provide a time of beam-beam collision, collision vertex, event trigger and centrality. The central arms are

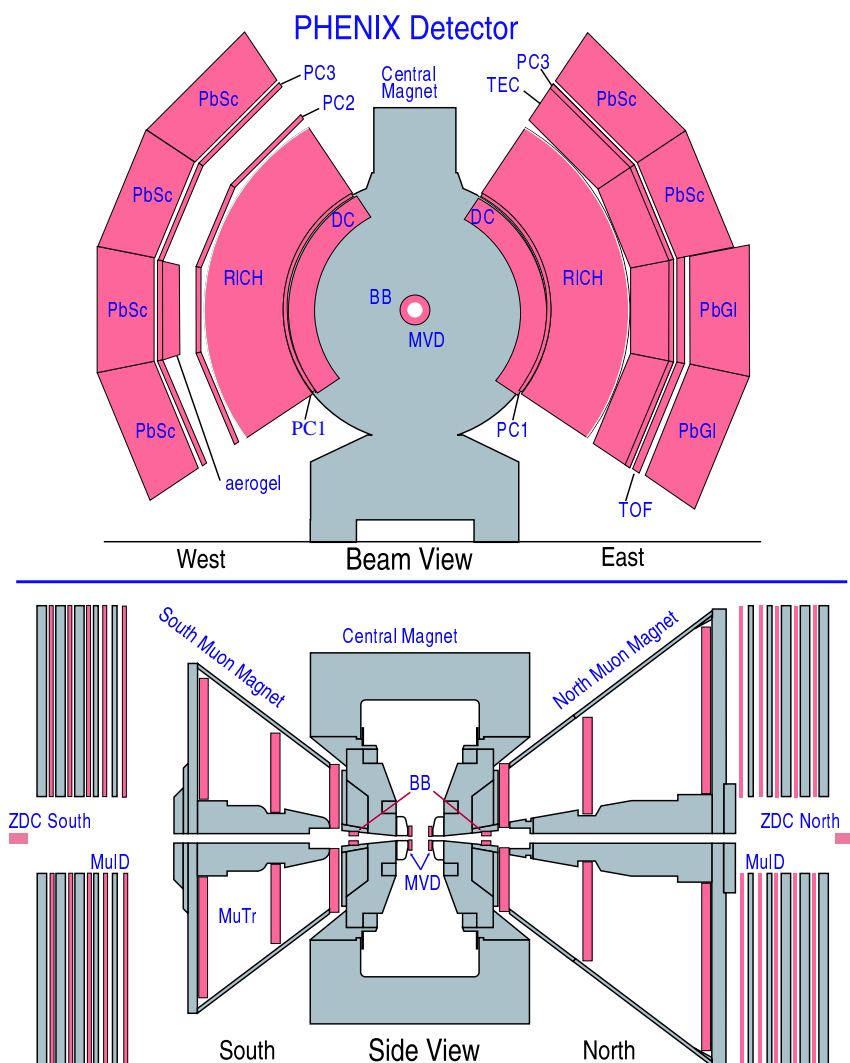


Figure 2.3: PHENIX experiment setup in the 4th year of RHIC run (Run4). (Top: Cross section perpendicular to the beam pipe. Bottom: East side view of the cross section along the beam pipe.) PHENIX consists of four parts of spectrometer arms and a set of global detectors. The spectrometers around mid-rapidity are called central arms (west and east arm), and those around forward rapidity are called muon arms.

designed to track particles emitted from collisions vertex, reconstruct momentum, and identify charged and neutral particles. The central arms cover the pseudo rapidity range  $|\eta| < 0.35$  and  $90^\circ$  in azimuthal angle. The central arms consist with several subsystems. The Drift Chamber (DC) measure charged particle trajectories in the  $r$ - $\phi$  plane. The Pad Chambers (PC) measure 3-D space position along the straight line particle trajectories. The Ring Imaging Cherenkov Counter (RICH) is the primary detector for electron identification, is installed in each central arm. The Electro-Magnetic Calorimeter (EMCal) is used to measure the spatial position and energy of electrons and photons. The combination of the RICH and the EMCal allows separation of  $\pi/e$  to less than  $10^{-4}$  at  $p < 4.7$  GeV/c [43]. The time-of flight detector (TOF) is the primary detector for charged hadron identification. The performance of the RICH, TOF and EMCal is summarized in Table 2.3.

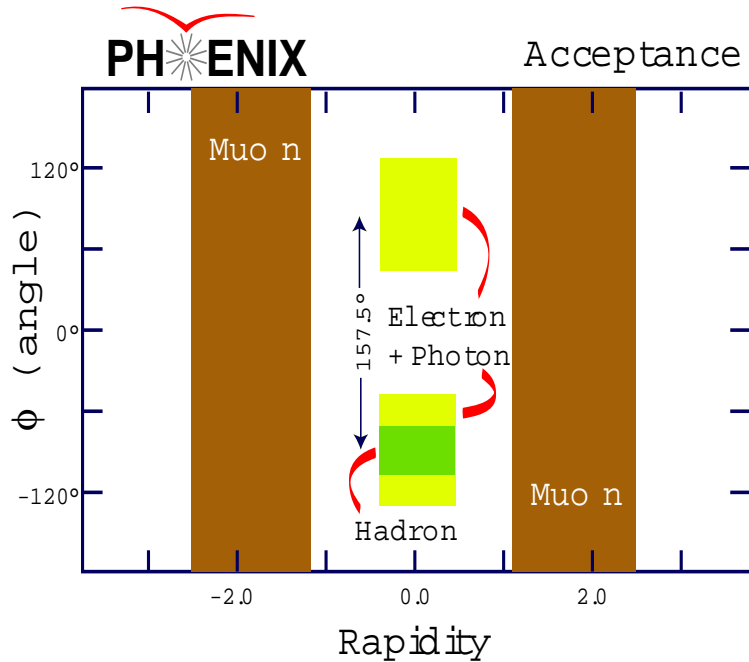


Figure 2.4: PHENIX acceptance of leptons and hadrons.

## 2.3 Magnet system

The PHENIX magnet system [44] is composed of three spectrometer magnets, Central Magnet (CM) and Muon Magnets (MMN and MMS), with warm iron yokes and water-cooled copper coils. The transverse momentum of each particle is determined from its curvature

Electrons	$\pi/e < 10^{-4}$ at $p \leq 4.7 \text{ GeV}/c$ RICH for $< 4.7 \text{ GeV}/c$ EMCal for $> 0.5 \text{ GeV}/c$
Photons	$p_t \leq 1 \text{ GeV}/c$ for 0.5 sr with PbGl. $p_t \leq 1 \text{ GeV}/c$ for 1.5 sr with PbSc.
Hadrons	$\leq 2.3 \text{ GeV}/c$ $\pi$ for 0.38 sr $\leq 1.6 \text{ GeV}/c$ K for 0.38 sr $\leq 5.0 \text{ GeV}/c$ p for 0.38 sr TOF with $\sigma < 100 \text{ ps}$ .

Table 2.3: Performance of the RICH, TOF and EMCal at Year-2 [43].

bend in the magnetic field provided in the central arms. The CM is energized by two pairs of concentric coils and provides a magnetic field around the interaction vertex that is parallel to the beam. The field covers pseudo rapidity region  $|\eta| < 0.35$  and it allows momentum analysis of charged particles in polar angle range from  $70^\circ < \theta < 110^\circ$ . The magnetic field for the central arms is axially symmetric around the beam axis. Its component parallel to the beam axis has an approximately Gaussian dependence on the radial distance from the beam axis, dropping from 0.48 T at the center to 0.096 T (0.048 T) at the inner (outer) radius of the DC. The total field integral is about 0.8 Tesla-meters and that is minimized for the radius of  $R > 2 \text{ m}$  (the radius of the DC).



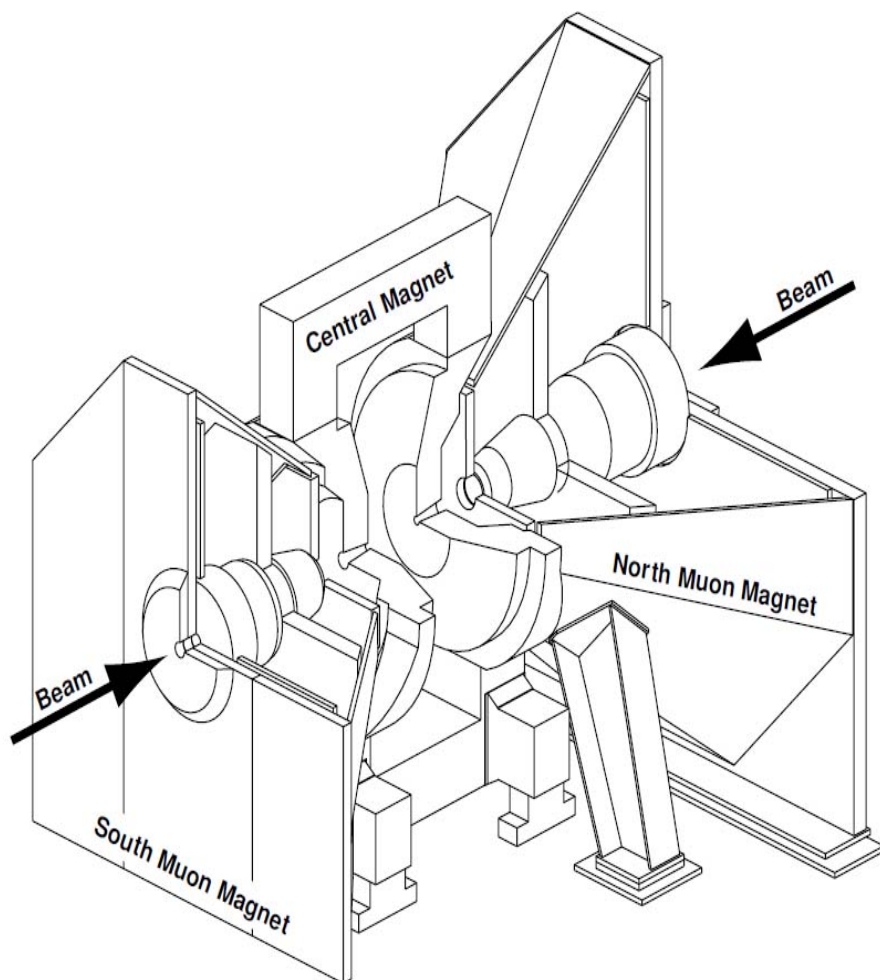


Figure 2.5: Line drawings of the PHENIX magnets, shown in perspective and cut away to show the interior structures.

## 2.4 Global detectors

### 2.4.1 Beam-Beam counters (BBCs)

The main role of BBCs is to provide the time of beam-beam collision, to produce a signal for the PHENIX LVL1 trigger, to measure the collision vertex point, to determine collision centrality with ZDCs and determined a reaction plane.

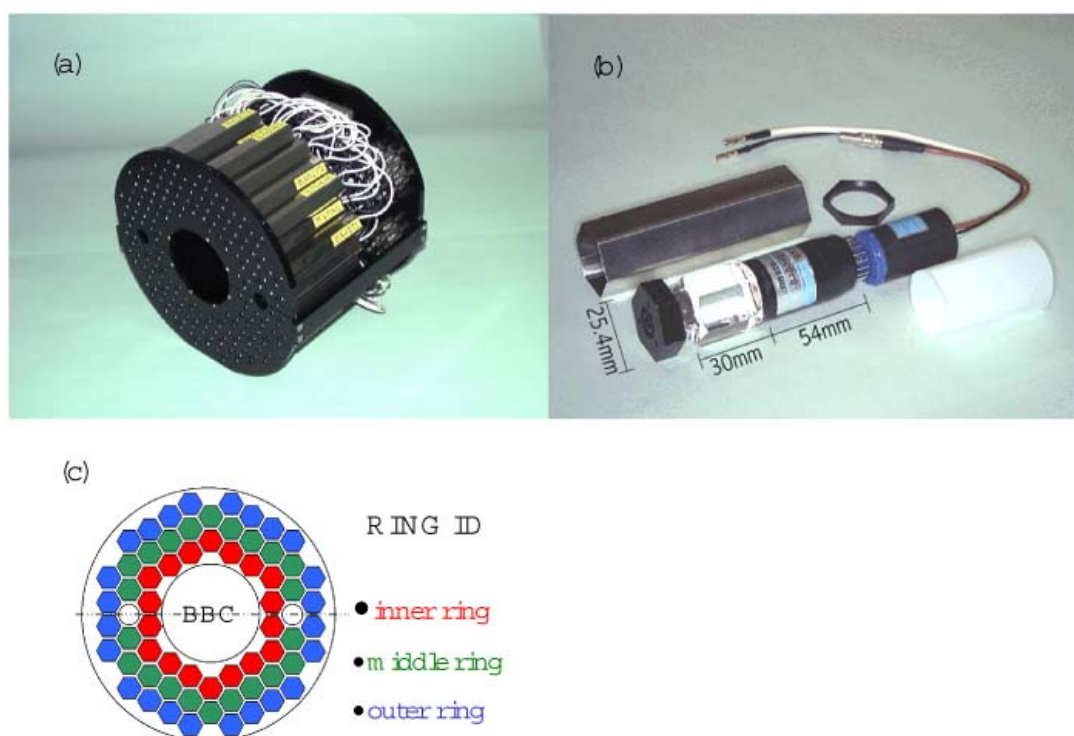


Figure 2.6: (a) A picture of BBC array comprising 64 BBC elements. (b) A picture of BBC element which consists of one-inch mesh dynode PMT mounted on a 3 cm quartz radiator. (c) The configuration of the 64 PMTs of each BBC.

Two sets of BBC are installed on North and South side of the collision point along the beam axis. The BBCs are placed 144 cm from the center of the interaction region and surround the beam pipe. This corresponds to a pseudo rapidity range from 3.0 to 3.9 over the full azimuth. Each BBC is composed 64 BBC elements. A BBC element consists of one-inch mesh dynode photomultiplier tubes mounted on a 3 cm quartz radiator. The BBC

elements are grouped inner, middle and outer ring. The outer ring of the BBC is 30 cm and inner ring is 10 cm with clearance between the beam pipe and the BBC of 1 cm. This configuration is satisfied following requirements.

- Work in a high magnetic field environment due to the BBC is placed just behind the CM.
- Radiation hard due to the BBC is placed in a very high-level radiation area around beam pipe.
- The BBC have a large dynamic range from 1 Minimum Ionizing Particles (MIP) to 30 MIP's due to the BBC are operated with not only Au-Au collisions at  $\sqrt{s_{NN}} = 200$  GeV but also p-p collisions up to  $\sqrt{s_{NN}} = 500$  GeV

The BBCs measure the time and charge of leading charged particles from beam collisions. The time information provides the time of beam-beam collision and the collision vertex. The charge information is used for determinations of the centrality and the reaction plane angles.

### 2.4.2 Zero-Degree Calorimeters (ZDCs)

The purpose of the ZDCs is to detect neutral beam fragments from collisions. The ZDCs are installed in the four RHIC experiments and each ZDC covers 2 mrad of forward angular cone which corresponds to  $\eta > 6.0$ . In PHENIX two ZDCs are located 18 m downstream and upstream from the interaction point along the beam axis. In front of the ZDCs, the DX dipole magnets are installed. Charged particles emitted from collisions are deflected out of the ZDC acceptance by the magnets. The ZDCs are hadron calorimeters. A single ZDC consists of three modules and each module consists of Tungsten alloy plates and ribbons of commercial optical fibers in a sampling layer. The coincidence signal from the ZDCs is used for the minimum bias trigger of beam interactions, and it uses as an other type of event triggers and the luminosity monitor. The total energy (multiplicity) of neutrons measured by the ZDCs is to be correlated with event geometry therefore the information is useful to determine the centrality in each events.

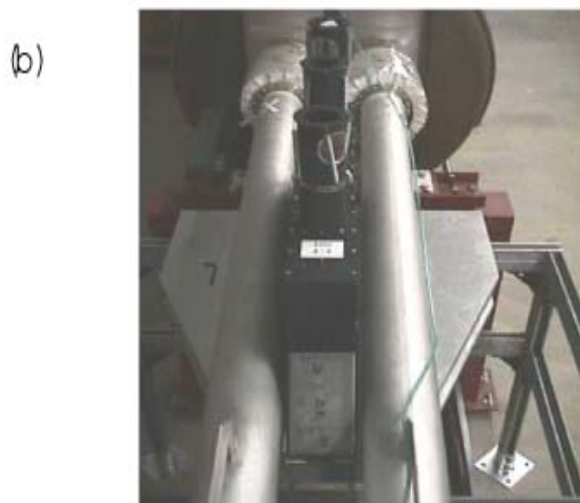
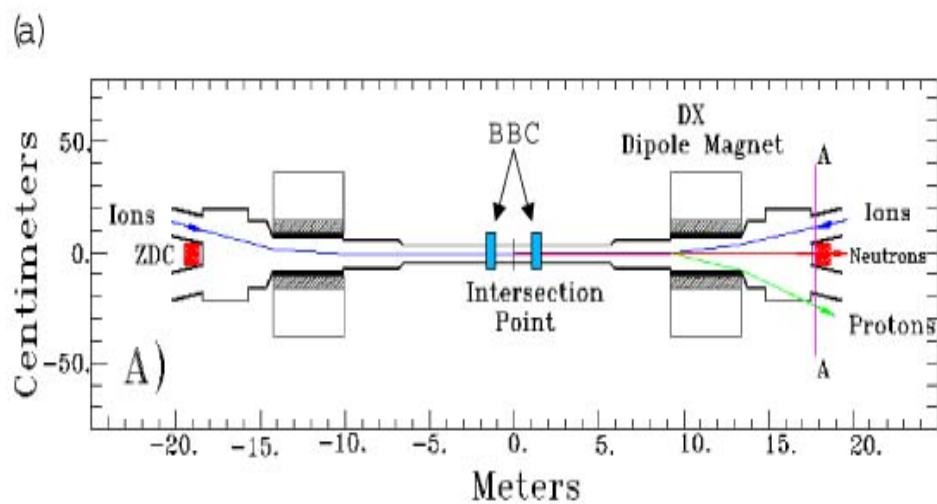


Figure 2.7: (a) Top view of the beam geometry and ZDC location. (b) A picture of ZDC.

## 2.5 Central arms detectors

### 2.5.1 Drift Chambers (DCs)

The main role of DCs is to measure charged particle's momentum and provide position information that is used to link tracks through the various PHENIX detector subsystems. The DCs are located in the region from 2 to 2.4 m from the z axis and 2 m along the beam direction.

In order to have good tracking efficiency for the highest multiplicities at Au-Au collisions, the DC is designed to satisfy the below requests.

- single wire resolution better than 150 in  $r-\phi$
- single wire two track separation better than 1.5 mm.
- single wire efficiency better than 99%
- spatial resolution in the z direction better than 2 mm.

Each DC consists of two independent gas volumes located in the west and east arms. A gas mixture of 50 % Ar and 50 % Ethan is chosen for the operation based on (1) uniform drift velocity at the electric field  $E \sim 1$  kV/cm, (2) high gas gain (3) low diffusion coefficients. The volume of the each detector is defined by a cylindrical titanium frame defining the azimuthal and beam-axis limits of the detector volume. Each frame consists of 20 identical keystones. The lay out of one of the keystone is shown in Fig. 2.8. Each keystone has six types of wire modules: X1, U1, V1, X2, U2 and V2. The modules contain 4 sense planes and 4 cathode planes forming cells with a 2-2.5 cm drift space in the  $\phi$  direction. The X1 and X2 wire modules give the track measurements in  $r - \phi$ . In addition, the modules have two sets of small angle U,V wire planes used in the pattern recognition. U1, V1, U2, and V2 measure the z coordinate. These wires have stereo angles of 6 relative to the X wires to minimize track ambiguities by matching the z resolution of the pad chamber.

Following performances are obtained.

- single wire efficiency 95-98 %
- spatial resolution 100-120 mkm
- angular resolution  $d\alpha/\alpha \sim 1$  mrad

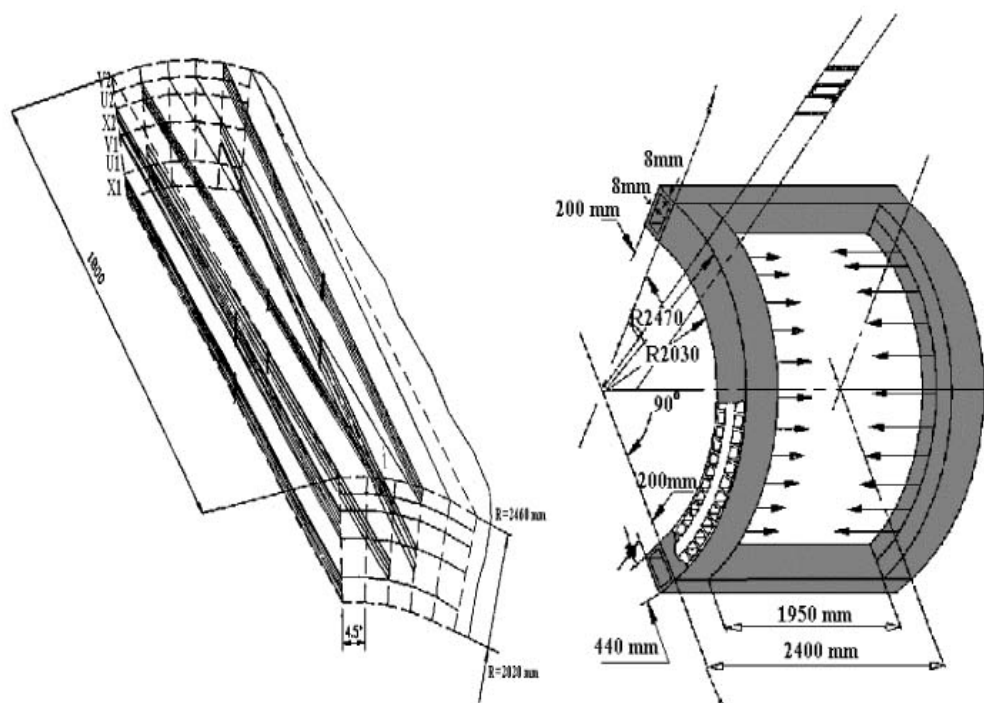


Figure 2.8: (left) The layout of wire position of DCs. (right) Constriction of a DC frame.

### 2.5.2 Pad Chambers (PC)

PCs are multi-wire proportional chambers which consist of a single plane of wires inside a gas volume bounded by two cathode pad planes. One cathode pad is separated into an array of pixels. Nine pixels are connected together electronically to form the pad, the basic element of the detector. A cell is defined by three pixels and the area is  $0.84 \times 0.84 \text{ cm}^2$ . This provides a position resolution of  $\pm 1.7 \text{ mm}$  along  $z$  and  $2.5 \text{ mm}$  in  $r - \phi$ .

The central arms have three layers of PCs (called PC1, PC2 and PC3). PC1 is located between the DC and RICH on the East and West arms. Also on both arms, PC3 is installed just in front of EMCal. PC2 behind the RICH is in West arm only. PC1 determined the three-dimensional momentum vector by providing the  $z$  coordinate at the exit of the DC. The information of the DC and PC1 provides direction vectors through the outer detectors of subsystems (RICH, PC2, PC3, EMCal and TOF). PC2 and PC3 are used to reject particles produced by either secondary interactions and particle decays outside the aperture of the DC and PC1 or low-momentum primary tracks that curve around PC1 in the magnetic field and hit PC2 and PC3. The recognition of three points on a track through the whole detector ensures that the response from electron identifying detectors (RICH and EMCal) and the momentum from the DC is correlated for particle identification.

### 2.5.3 Ring Imaging Cherenkov Counters (RICHs)

The RICH is the primary device for identifying electrons among a very large number of charged particles. The basic idea of RICH is a Cherenkov radiation. Cherenkov radiation arises when a charged particle in a material medium moves faster than the speed of light in that same medium. The speed of light in a medium is given by

$$v = c/n, \quad (2.1)$$

where  $c$  is light velocity and  $n$  is the index of the medium. Therefore a particle emits Cherenkov radiation when it has a velocity

$$v_{particle} > c/n. \quad (2.2)$$

Cherenkov photons are emitted as a circular cone shape with an angle  $\theta_c$  defined as;

$$\cos \theta_c = \frac{1}{\beta n} \quad (2.3)$$

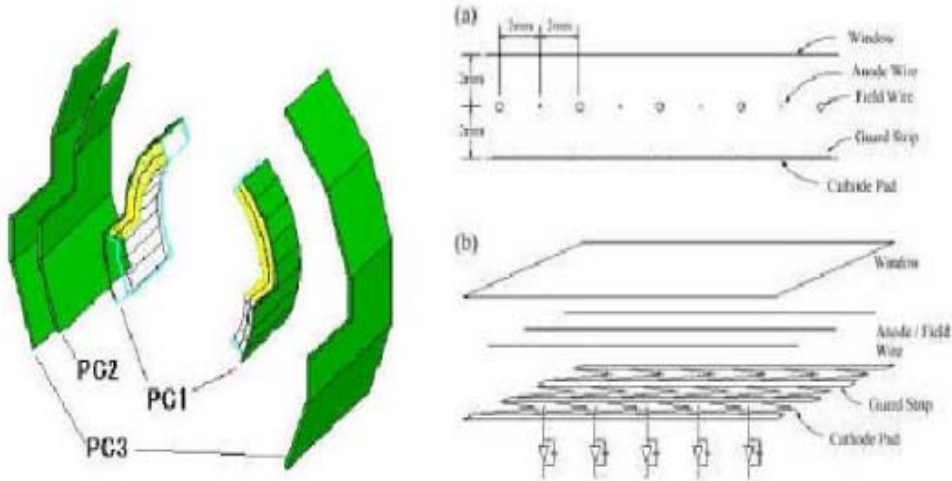


Figure 2.9: A picture of the Pad Chamber system in PHENIX.

where  $\beta$  is  $v_{particle}/c$  and it is a threshold for Cherenkov radiation. A particle which has a faster velocity than the light emits photons, and the emitted photons are optically focused on the photon detectors, on which Cherenkov photons are detected on a ring in the RICH.

Figure 2.10 shows a cutway drawing of the RICH. Each RICH has a volume of  $40 \text{ m}^3$ , with an entrance window area of  $8.9 \text{ m}^2$  and an exit window area of  $21.6 \text{ m}^2$ . Each detector contains 48 composite mirror panels which are formed two intersecting spherical surfaces. The total reflecting area is  $20 \text{ m}^2$ . The reflectivity of the mirrors is about 83 % at 200 nm, rising to 90 % at 250 nm. Cherenkov light radiated in the RICH is focused onto two arrays of 1280 UV photomultipliers (Hamamats H3171S). The phototubes are fitted with 2 diameter Winston cones and have magnetic shields. The phototube UV glass windows absorb photons of wavelengths below 200 nm. Each phototube array is located on either side of the RICH entrance window.

During Run4,  $\text{CO}_2$  ( $n = 1.000410$ ) was used as the Cherenkov radiator. It has a pion Cherenkov threshold of  $4.65 \text{ GeV}/c$  and produces an average of 12 photons per ring for  $\beta = 1$  particle. The ring diameter for  $\text{CO}_2$  gas is about  $11.8 \text{ cm}$ .

The  $\pi/e$  discrimination capabilities of the RICH are determined by three factors.

- the value of the pion Cherenkov threshold



- the statistical fluctuations in the number of photoelectrons produced by an electron in RICH
- the background counting rates in the RICH

The combination of the RICH and EMCAL allows a separation of  $\pi/e$  to less than  $10^{-4}$  at  $p < 4.7 \text{ GeV}/c$ .

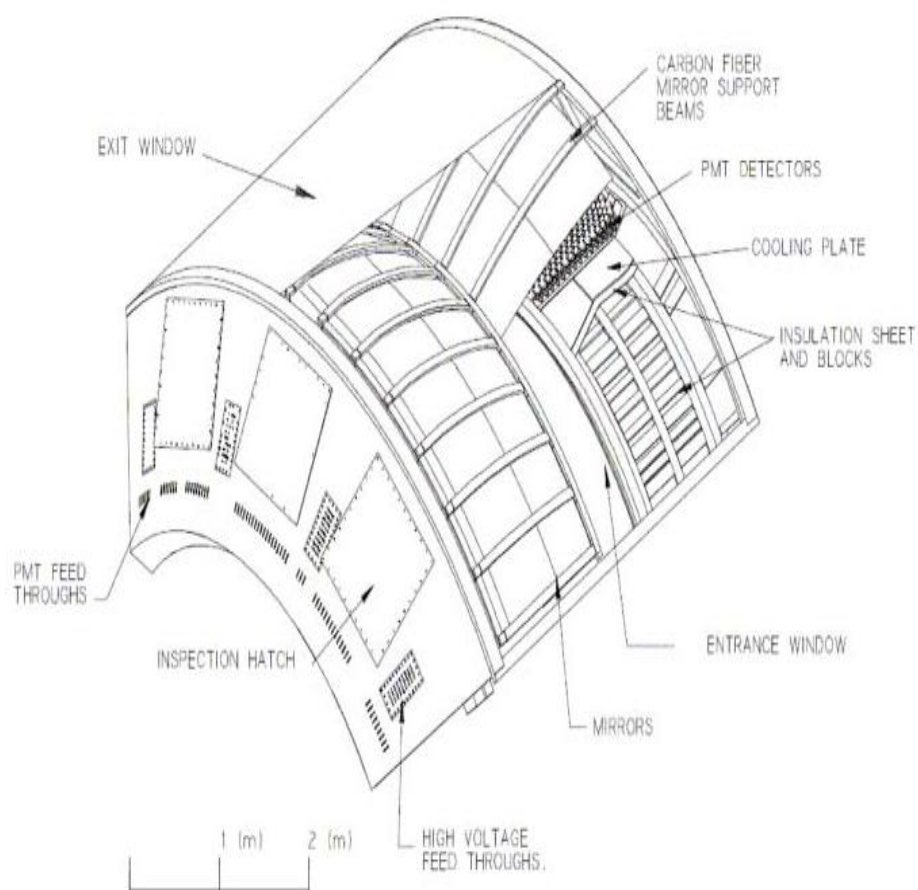


Figure 2.10: A cutaway view of one arm of the PHENIX RICH detector.

### 2.5.4 Electro-Magnetic Calorimeters (EMCals)

The EMCal is used to measure the spatial position and energy of electrons and photons. It covers the full central arm acceptance of  $70^\circ < \theta < 110^\circ$  with each of the two walls subtending  $90^\circ$  in azimuth. There are eight sectors of the EMCals in the East and West arm. The West arm has four sectors of Pb-scintillator sampling calorimeter, and the East arm has two sectors of Pb-scintillator and two of Pb-glass Cherenkov calorimeter. The Pb-scintillator electromagnetic calorimeter is a shashlik type sampling calorimeter made of alternating tiles of Pb and scintillator consisting of 15,552 individual towers. Figure 2.11 shows a Pb-scintillator electromagnetic calorimeter module consisting of four towers. The Pb-scintillator electromagnetic calorimeter has a nominal energy resolution of  $8.1\% / \sqrt{E}$  (GeV)  $\oplus 2.1\%$ . A Pb-glass calorimeter sector consists 192 super modules. Each super module comprises 24 Pb-glass modules. The Pb-scintillator electromagnetic calorimeter has a nominal energy resolution of  $6\% / \sqrt{E}$  (GeV).

The EMCal is designed to identify and measure the total energy of electrons and photons. Electrons deposit all of their energy in the the EMCals , therefore the energy  $E$  measured by the EMCals and the momentum  $p$  measured by the DCs should match, i.e.  $E/p \approx 1.0$  for electrons. On the other hand hadrons deposit only a small fraction of their total energy in the calorimeter.

### 2.5.5 Time of flight (TOF)

The TOF provides flight time of particles. Using the flight time of particles, the particles are identified by calculating the mass as;

$$m^2 = p^2 \left( \left( \frac{T_{flight} c}{L} \right)^2 - 1 \right), \quad (2.4)$$

where  $L$  is a flight path length which is the distance between TOF and vertex position in the magnetic field and  $T_{flight}$  is a flight of the particles. It is designed to have a timing resolution of 100 ps in order to separate particles in the high momentum range, i.e.  $\pi/K$  separation up to 2.4 GeV/c and  $K/p$  separation up to 4.0 GeV/c.

The TOF is located at a radial distance of 5.06 m from the interaction point, between PC3 and the EMCal in the east arm, and it covers  $|\eta| < 0.35$  and  $\Delta \phi = 45$  in azimuthal angle. The TOF system consists of 10 panels of TOF walls and the wall consists of 96 TOF elements. One TOF element consists a plastic scintillator slat and PMTs are equipped at the both ends of the scintillator. The Schematic diagram of the components of a single TOF panel are illustrated in Fig. 2.12.

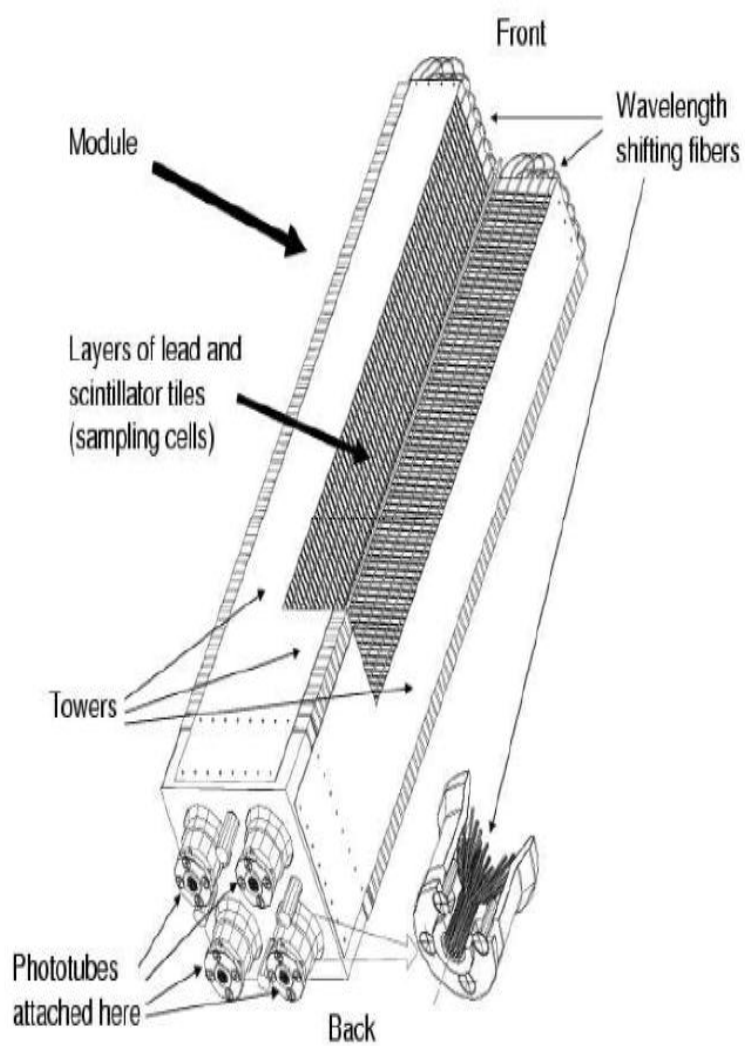


Figure 2.11: Interior view of a Pb-scintillator calorimeter module showing a stack of scintillator and lead plates, wavelength shifting fiber readout and leak fiber inserted in the central hole.

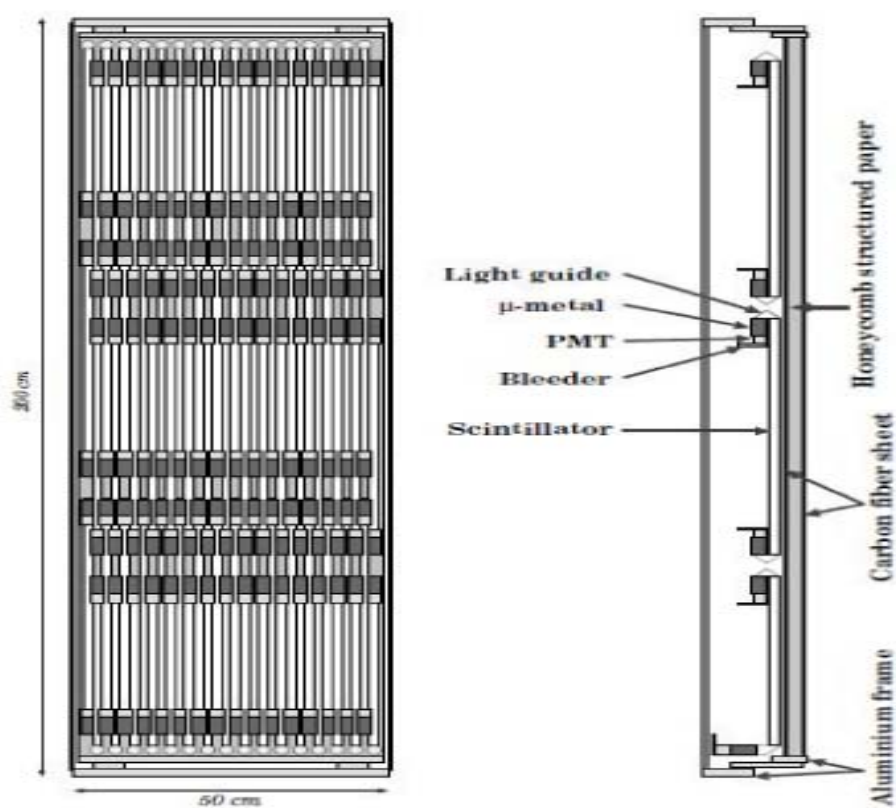


Figure 2.12: Schematic diagram of the components of a single TOF panel which consists of 96 plastic scintillation counters with PMTs at both ends, light guides and supports.

# Chapter 3

## Data analysis

The analysis of the elliptic flow for electrons originating from heavy quarks is based on the experimental data of Au+Au collisions at  $\sqrt{s_{NN}} = 200$  GeV in the fourth year of RHIC run (2004 ~ 2005) at RHIC. About 700M minimum bias events are used in this analysis after the vertex cut is applied. In this chapter, we present the event selection, track reconstruction, electron identification, reaction plane determination and determination of the electrons from heavy quarks.

### 3.1 Event selection

The collisions which meet following conditions are used in this analysis. The first condition is the number of hits in the BBC and the ZDC. For the BBC, a coincidence between the north and south BBC with at least two PMTs fired in each BBC is required. For the ZDC, at least one forward neutron has to be register in each of two ZDCs. In addition, a cut for the collision vertex point along the beam line is also required. The collision vertex point is determined by the timing difference of the BBCs. A event vertex position along the beam axis ( $Z_{vertex}$ ) is reconstructed from the time information from BBCs as;

$$Z_{vertex} = \frac{(T_1 - T_2)c}{2}, \quad (3.1)$$

where  $c$  is the light velocity,  $T_1$  and  $T_2$  are the observed values of arrival time for prompt particles at the each side of BBC. The resolution is about  $\pm 0.6$  cm. Based on a simulation of the BBC, the efficiency for above condition is  $92 \pm 3$  % in Au+Au  $\sqrt{s_{NN}} = 200$  GeV. We required  $|z_{vertex}| < 20$  cm to eliminate electrons originating from the conversions at the central magnets [42].

## 3.2 Centrality determination

In collisions with non-zero impact parameter, charged particles produced by the collisions are detected by the BBC, and spectator neutrons which do not participate in the collisions are detected by the ZDC. For central collisions charged particles detected by the BBC are more than spectator neutrons detected by the ZDC. On the other hand, spectator neutrons measured by the ZDC are more than the charged particles detected by the BBC in peripheral collisions. Therefore combining information of the spectator neutrons measured by the ZDC and the charge sum information measured by the BBC provides the event centrality. Figure 3.1 shows the correlation between the charge sum of charged particles and the energy sum of spectator neutrons. For more peripheral collision, the spectator neutrons measured by the ZDC are decreased, *i.e.* spectator neutrons miss the ZDC. It is due to the intrinsic  $p_T$  from their Fermi motion inside the Au nuclei or they may bound in deuterons of heavier fragments and thus swept away by the magnet. It has been reported by the NA49 experiment that such spectator neutrons missing has an approximately linear relationship as a function of the impact parameter [45], and the missing is larger in peripheral collisions. The lines in the figure present the definition of centrality classes in the ZDC vs. BBC plot. The centrality classes are obtained by calculating the angle  $\phi$  of a given (BBC,ZDC) point with relative to  $(\text{BBC}_0, \text{ZDC}_0) = (0.2, 0.0)$  on the ZDC vs. BBC plane. The full  $\phi$  range which covers centrality 0 % to 92 % is divide to 92 with the same number of counts in each bins. The first bin is defined as centrality 0 %, therefore the  $n$  th bin represents centrality  $n - 1$  %. Thus we obtain the one-to-one correspondence between  $\phi$  cut and the centrality ranges in percentages.

## 3.3 Track Reconstruction and momentum determination

Charged particle tracks are reconstructed by using the hit information at the DCs (X1, X2, UV1 and UV2) and the PC1. In the process of the reconstruction, tracks that traverse both X1 and X2 wires are looked then the remaining tracks that traverse the X1 or X2 regions are looked. Using a combinatorial Hough transform (CHT), tracks are found from the hits information of X1 and X2 wires. In this method all possible combinations of hits at X1 and X2 wires are transferred into a feature space defined by the polar angle at the intersection of the track with a reference radius near the mid-point of the drift chamber,  $\phi$ , and the inclination of the track at that point  $\alpha$  which is proportional to the inverse of the transverse momentum. Figure 3.2 provides a schematic illustration of these variables. Assuming tracks are straight line in the DCs, tracks are appear as peaks in the Hough transform feature

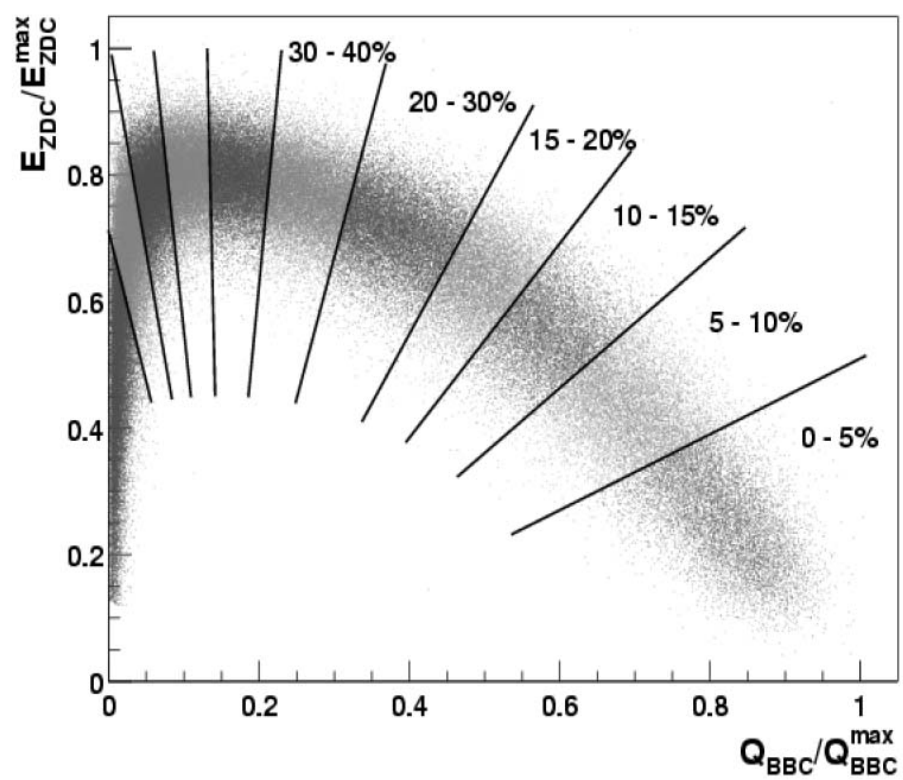


Figure 3.1: Correlation between the charge sum measured by BBC and energy of spectator neutrons measured by the ZDC. The lines in the figure present the definition of centrality classes in the ZDC vs. BBC plot.

space, because all hit pairs for a given track will have same  $\phi$  and  $\alpha$ .

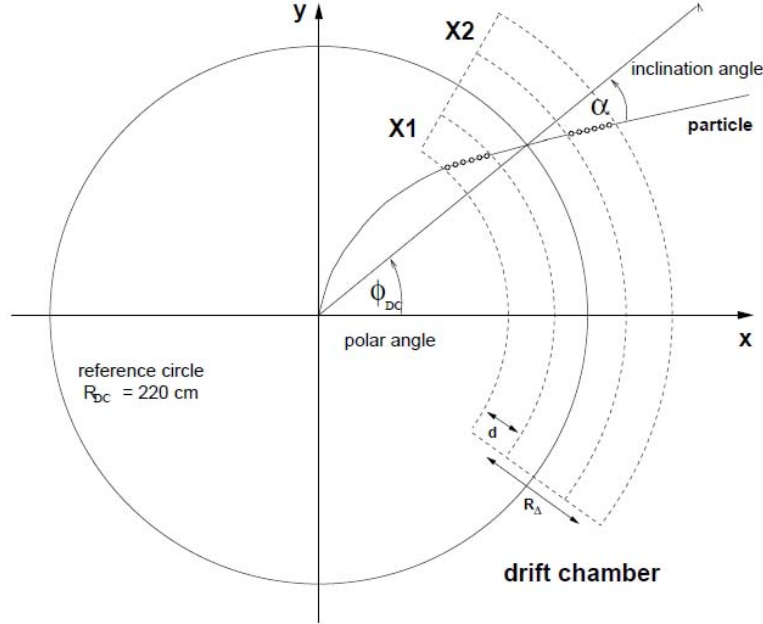


Figure 3.2: Definition of the Hough transform parameters ( $\phi$  and  $\alpha$ ) for the drift chamber track reconstruction. The X1 and X2 hits in the drift chamber are shown as small circles.

After the reconstruction of the track by using CHT method, then the  $z$  coordination of tracks is determined by using PC1 and UV wires. If there is a PC1 association, then a straight line connecting  $z_{ver}$  and PC1  $z$  fixes the direction of the track in  $z$ . If there is more than one PC1 association, the one with more associated UV hits is accepted to be the correct track. As a result of the reconstruction, variety possible tracks are made. These tracks are identified by the quality bits which are defined by the hit information at X1, X2, UV and PC1.

Tracks reconstructed by the DC-PC1 are then associated outer detectors (detectors after PC1). These detectors provide hits information at the detectors and the one with the closed distance to the track intersection point is identified as the hit associated with the track (track matching). Then the distance in  $\phi$  and  $z$  directions between the track projection point and the associated hit position are calculated. In this analysis, following the track matching is required.

- $\sqrt{EMCd_{z_{electrons}}^2 + EMCd_{\phi_{electrons}}^2} < 2.0,$



here  $EMCdz_{electrons}$  ( $EMCd\phi_{electrons}$ ) is a  $1\sigma$  deviation of the distance in  $z$  ( $\phi$ ) direction between the track projection point and the associated hit position at the EMC, after electron identification (See Chapter 3.4).

Momentums for charged particles are determined by measuring the track's angular deflections from a straight line,  $\alpha$ . The  $\alpha$  measured in the drift chamber is closely related to the field integral along the track trajectory. For tracks emitted perpendicular to the beam axis, this relation can be approximated by

$$\alpha = \frac{K}{p}, \quad (3.2)$$

where  $K=101$  mrad GeV is the field integral.

### 3.4 Electron identification

After reconstructing the tracks, electrons are identified with following processes. First the RICH PMTs associated with the track were searched. This is done by first reflecting the track about the RICH mirror as if it were a light ray, and then projecting the reflected track on the RICH PMT. The projection point is the center of the ring which was made by the Cherenkov radiation, therefore PMT hits near the projection point in the region ( $3.4 \text{ cm} < r < 8.4 \text{ cm}$ ) are searched (the expected ring radius is  $5.9 \text{ cm}$ ). The region is determined from the position resolution of the PMTs. If the hits are found, following parameters are calculated from the projection point and PMT hit information.

- Distance between ring center and track projection (disp)
- Number of hit PMTs (n0)
- Difference from the expected ring shape (chi2/npe0)

The minimum and maximum values of these parameters for electron identification are summarized in Table 3.1. In addition to the RICH parameters, following a parameter is calculated for the electron identification.

- shower shape in EMC (*prob*)

To reduce the background from hadrons and photon conversions far from the vertex, energy measured in the EMCal and momentum matching ( $E/p$ ) is required. Electrons deposit all of their energy in the EMCal; therefore the  $E/p$  is approximately 1.0 though the  $E/p$  of hadrons have a mip peak at  $\sim 0.3$  by hadronic interactions in EMCal. The momentum

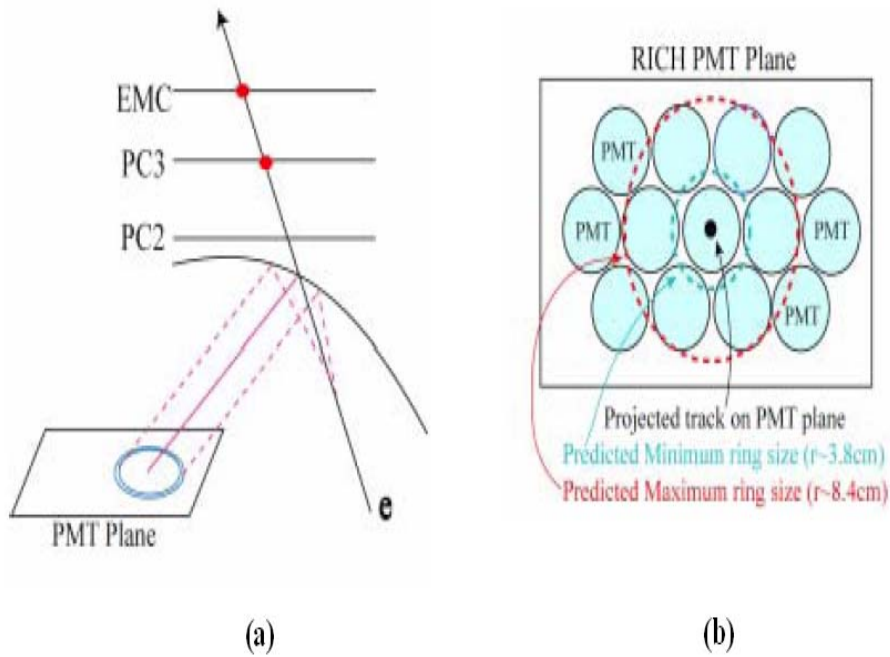


Figure 3.3: an illustration of electron identification by RICH. (a) Cherenkov photons are emitted by the electrons at RICH. (b) The Cherenkov photons are reflected by the mirrors and make a circle with 5.9 cm radius on the PMT arrays.

of electrons produced by the photon conversion outer of the vertex are overestimated their momentum, therefore the  $E/p$  is smaller than 1.0. Fig. 3.4 shows the Energy and momentum matching ( $(E - p)/p/\sigma$ ). Here the  $\sigma$  means a standard deviation of  $(E - p)/p$ . In this analysis, we require  $E/p$  matching is larger than  $-2\sigma$ . The dashed line in the figure is the background caused by the accidental association of tracks with RICH hits. The background is estimated by the "flip-and-swap" technique;

- destroy position correlations between tracks and rings by "inverting" RICH coordinates
- perform electron ID cuts with inverted RICH coordinates

The swapped background shape of  $E/p$  distributions agrees with the distribution for the identified hadrons (Fig.3.5) [46]. Figure 3.6 shows the  $p_T$  dependence of the ratio of the

Type	parameter
Event	Event vertex $ bbc_z  < 20cm$
Track matching	$\sqrt{EMCd z_{electrons}^2 + EMCd \phi_{electrons}^2} < 2.0\sigma$
RICH	$n0 \geq 3$ $chi2/npe0 < 10.0$ $disp < 5.0$
other	$-2.0 < \frac{E-p}{p} / \sigma$ $prob > 0.01$

Table 3.1: Summary of electron ID

signal and background. As shown in Fig. 3.6, the background is about 18 % at  $p_T = 0.5$  GeV/c and the contribution is getting smaller at higher  $p_T$  region.

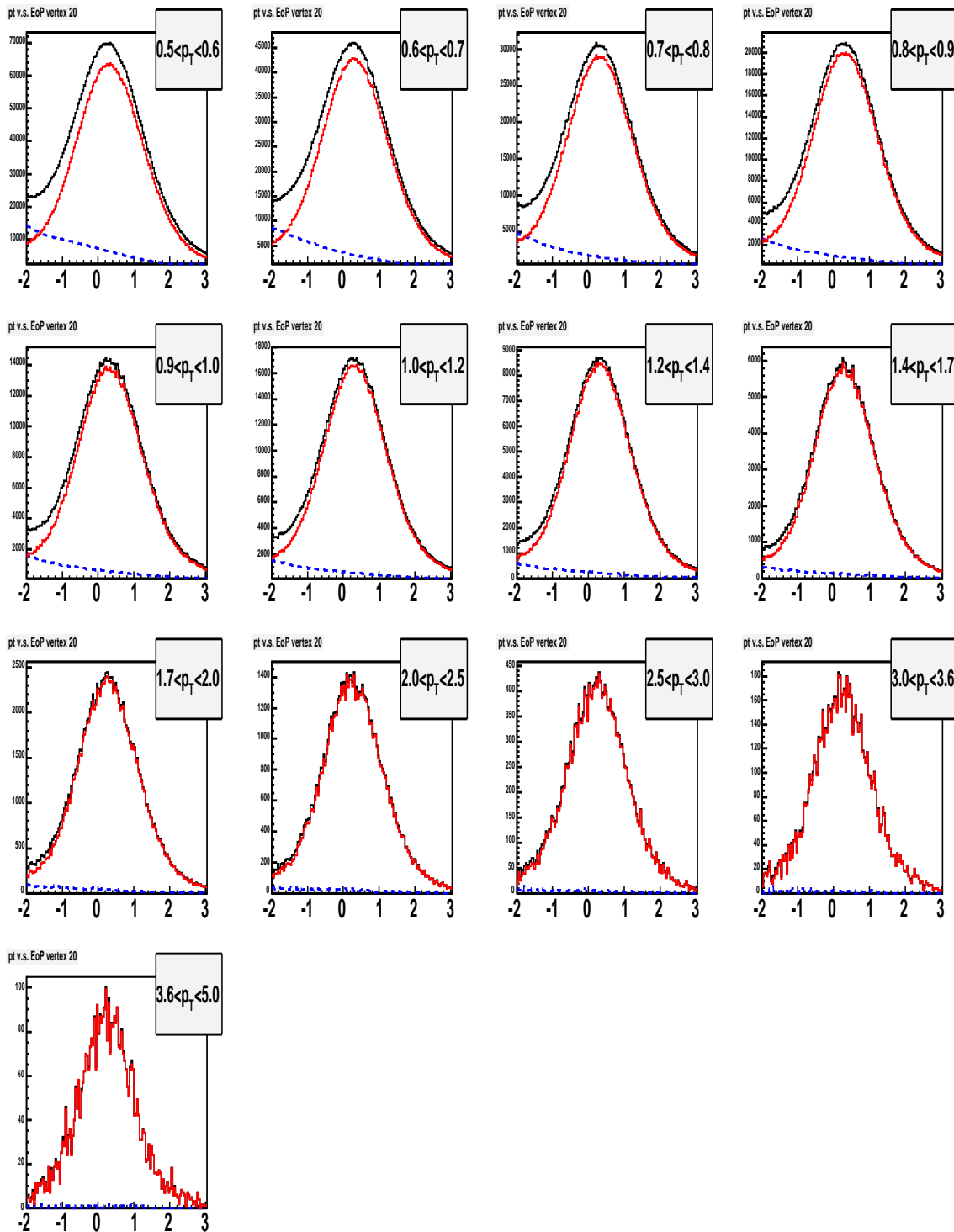


Figure 3.4:  $(E - p)/p/\sigma$  distributions in different  $p_T$  slices. The red line is for electrons after subtracting background (blue line) from electrons identified by RICH (black line).

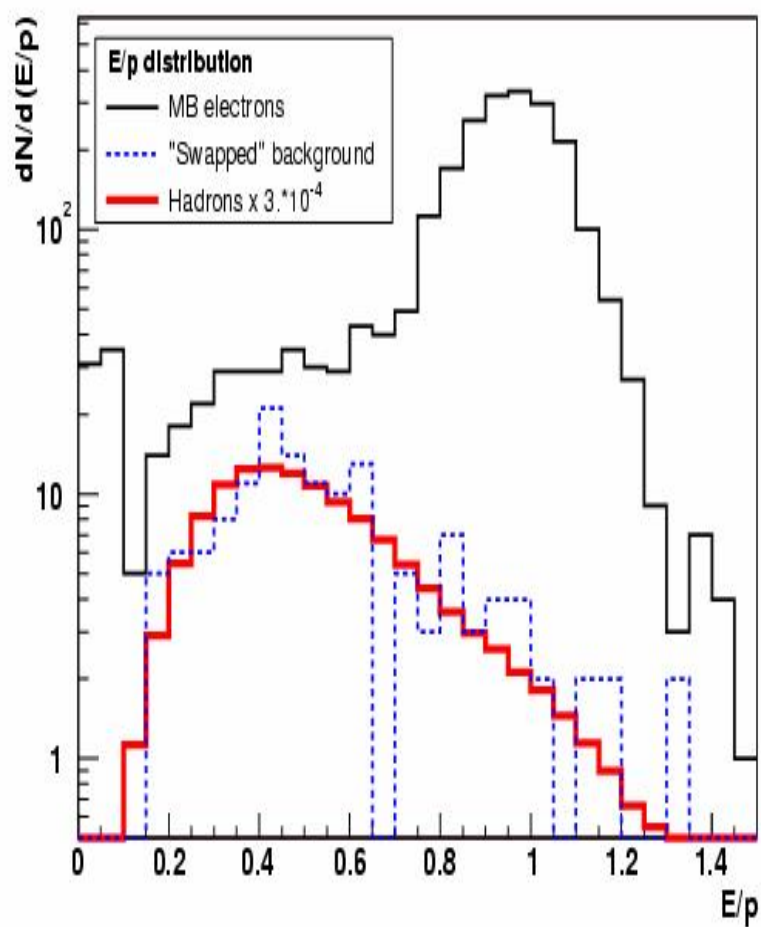


Figure 3.5:  $E/p$  distributions for electrons (black solid line), swapped background (dotted line), and hadrons (red solid line). The figure is taken from [46]

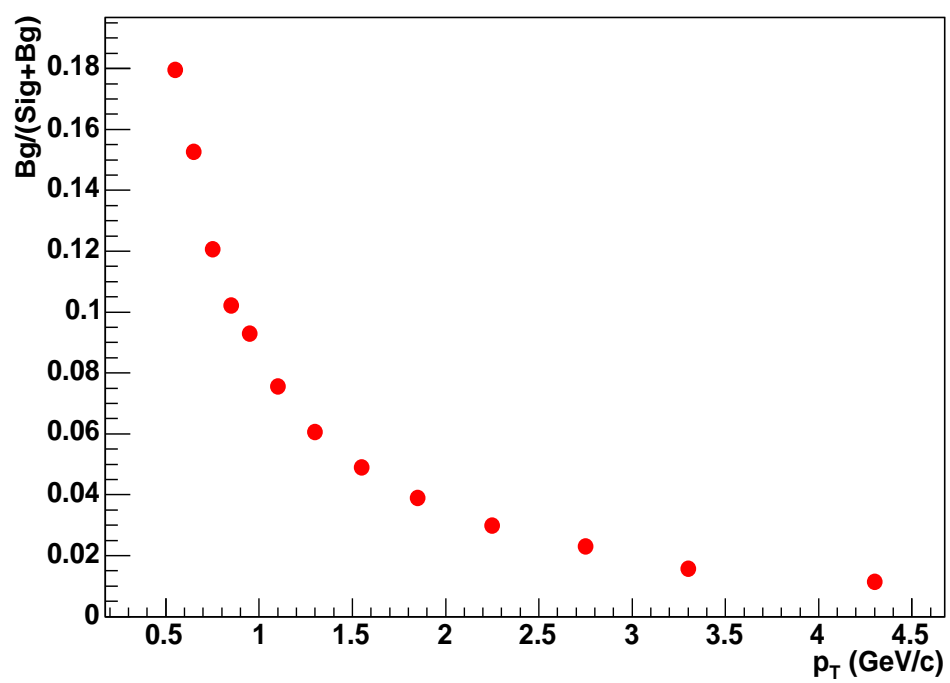


Figure 3.6: Signal to background ratio ( $B/(S+B)$ ) for electron signals as a function of  $p_T$ .

## 3.5 Azimuthal anisotropy analysis

### 3.5.1 Fourier Expansion of Azimuthal Distribution

The azimuthal anisotropy has been studied by using Fourier expansion of the azimuthal distributions. The azimuthal distribution of the produced particles,  $r(\phi)$ , can be written in the form of Fourier expansion [47];

$$r(\phi) = \frac{x_0}{2\pi} + \frac{1}{\pi} \sum_{n=1}^{\infty} [x_n \cos(n\phi) + y_n \sin(n\phi)], \quad (3.3)$$

For the case of a finite number of particles, the integrals become simple sums over particles:

$$x_n = \int_0^{2\pi} r(\phi) \cos(n\phi) d\phi = \sum_i r_i \cos(n\phi_i), \quad (3.4)$$

$$y_n = \int_0^{2\pi} r(\phi) \sin(n\phi) d\phi = \sum_i r_i \sin(n\phi_i), \quad (3.5)$$

where  $i$  runs over all particles generated by collisions, and  $\phi_i$  is the azimuthal angle of  $i$ -th particle. Here two variables,  $v_n$  and  $\psi_n$ , are defined as;

$$v_n = \sqrt{x_n^2 + y_n^2}, \quad (3.6)$$

$$\psi_n = \tan^{-1}(y_n/x_n)/n. \quad (3.7)$$

Here  $v_n$  means the strength of the  $n$ -th harmonic and  $\psi_n$  is called "reaction plane" corresponding to the direction of the nuclear impact parameter in a given collision (Fig. 1.6).

Using the azimuthal angle of the reaction plane ( $\psi_n$ ) and strength of  $n$ -th harmonic ( $v_n$ ), the coefficients  $x_n$  and  $y_n$  are written as;

$$x_n = v_n \cos(n\psi_n), \quad (3.8)$$

$$y_n = v_n \sin(n\psi_n). \quad (3.9)$$

From Eq. 3.8 and 3.9, Eq. 3.3 is written by using the  $v_n$  and  $\psi_n$ ;

$$r(\phi) = \frac{x_0}{2\pi} + \frac{1}{\pi} \sum_{n=1}^{\infty} [x_n \cos(n\phi) + y_n \sin(n\phi)] \quad (3.10)$$

$$= \frac{x_0}{2\pi} + \frac{1}{\pi} \sum_{n=1}^{\infty} [v_n \cos(n\psi_n) \cos(n\phi) + v_n \sin(n\psi_n) \sin(n\phi)] \quad (3.11)$$

$$= \frac{x_0}{2\pi} + \frac{1}{\pi} \sum_{n=1}^{\infty} [v_n \cos(n(\phi - \psi_n))]. \quad (3.12)$$

Especially the first harmonic ( $n=1$ ) and second harmonic ( $n=2$ ) coefficients called "directed flow" and "elliptic flow", respectively.

### 3.5.2 Reaction Plane method

The azimuthal angle distribution of the particle emission measured with respect to the reaction plane is called the “reaction plane method”. In the reaction plane method the azimuthal anisotropy is defined by

$$\frac{dN}{d\phi} = N_0 \left\{ 1 + \sum_n 2v_n \cos(n(\phi - \Psi_{R.P.})) \right\}, \quad (3.13)$$

where  $N_0$  is a normalization constant,  $\phi$  is the azimuthal angle of particles, and  $\Psi_{R.P.}$  is the azimuthal angle of the reaction plane. The harmonic coefficients,  $v_n$ , indicate the strength of the  $n^{\text{th}}$  anisotropy. The value of  $v_n$  is calculated by

$$v_n = \langle \cos(n(\phi - \Psi_{R.P.})) \rangle. \quad (3.14)$$

In experiment the true reaction plane is not able to determine directly, therefore the reaction plane is determined by using the anisotropy flow itself [48]. It means that the event plane can be determined independently for each harmonic of the anisotropic flow. Figure 3.7 is an illustration of the reaction plane determination. The flow vector  $Q_n$  and the reaction plane angle  $\Psi$  are defined as

$$Q_n \cos(n\Psi_n) = \sum_i w_i \cos(n\phi_i), \quad (3.15)$$

$$Q_n \sin(n\Psi_n) = \sum_i w_i \sin(n\phi_i). \quad (3.16)$$

Therefore the azimuthal angle of the reaction plane for the  $n^{\text{th}}$  harmonic is determined by

$$\Psi_n^{\text{meas.}} = \left( \tan^{-1} \frac{\sum_i w_i \sin(n\phi_i)}{\sum_i w_i \cos(n\phi_i)} \right) / n, \quad (3.17)$$

where  $\phi_i$  is the azimuthal angle of each particle used in the reaction plane determination and  $w_i$  is the corresponding weight. Due to the finite reaction plane resolution, coefficients in the Fourier expansion of the azimuthal distribution with respect to the “measured” reaction plane ( $v_n^{\text{meas.}}$ ) are smaller than coefficients measured with respect to the “real” reaction plane ( $v_n$ ). The relation between  $v_2$  measured with respect to the “measured” reaction plane and “real” reaction plane is

$$\begin{aligned} v_n^{\text{meas.}} &= \langle \cos(n(\phi_i - \Psi_{\text{meas.}})) \rangle \\ &= \langle \cos(n(\phi_i - \Psi_{\text{meas.}} + \Psi_{\text{true}} - \Psi_{\text{true}})) \rangle \\ &= \langle \cos(n(\phi_i - \Psi_{\text{true}})) \cos(n(\Psi_{\text{meas.}} - \Psi_{\text{true}})) \rangle \\ &+ \langle \sin(n(\phi_i - \Psi_{\text{true}})) \sin(n(\Psi_{\text{meas.}} - \Psi_{\text{true}})) \rangle \\ &= v_n \langle \cos(n(\Psi_{\text{meas.}} - \Psi_{\text{true}})) \rangle. \end{aligned} \quad (3.18)$$



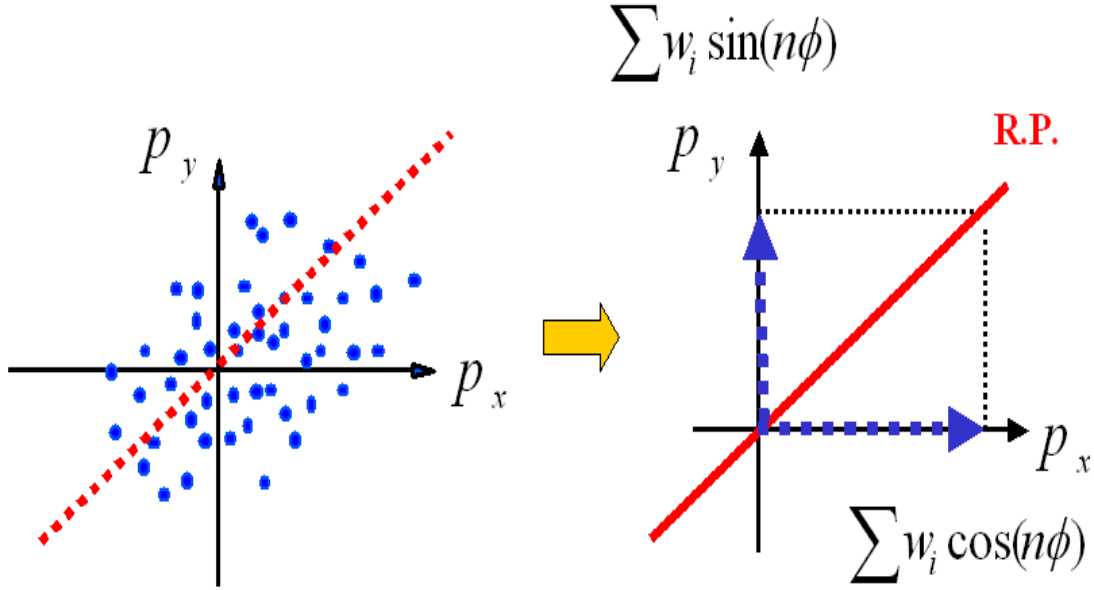


Figure 3.7: Illustration of the reaction plane determination. The true reaction plane can not measure directly therefore the plane is determined by using anisotropic flow itself.

Therefore the value of  $v_n$  is given as;

$$v_n = \frac{v_n^{\text{meas.}}}{\langle \cos(n(\psi_{\text{meas.}} - \psi_{\text{true}})) \rangle}. \quad (3.19)$$

The value of  $\langle \cos(n(\psi_{\text{meas.}} - \psi_{\text{true}})) \rangle$  is characterized as the “resolution” of the reaction plane [47].

### 3.5.3 Reaction Plane Determination

In this analysis the  $v_2$  is estimated by using the reaction plane determined by the second harmonic ( $n = 2$ ), since a better accuracy of  $v_n$  is obtained by using the same harmonic’s reaction plane [48]. The reaction plane is determined by using both BBCs. In the PHENIX experiment the reaction plane is also determined by using the central arm detectors. One of the key issues of the reaction plane determination is non-flow effects such as jets, resonance decays and HBT. This can be avoided by taking two remote rapidity intervals [49]. Since each BBC is roughly three units of pseudo rapidity away from the central arms, it is expected that the non-flow effects are smaller there than that in the central arm detectors [19].

Using the BBC information, the reaction plane is given by

$$\psi = \left( \tan^{-1} \frac{Q_y}{Q_x} \right) / 2, \quad (3.20)$$

$$Q_x = \sum_{i=1}^{64} q_i \cos(2\phi_i), \quad (3.21)$$

$$Q_y = \sum_{i=1}^{64} q_i \sin(2\phi_i), \quad (3.22)$$

where  $\phi_i$  is the azimuthal angle of each PMT and  $q_i$  is the charge information of each PMT. Due to the random distribution of the impact parameter direction in the collisions, the reac-

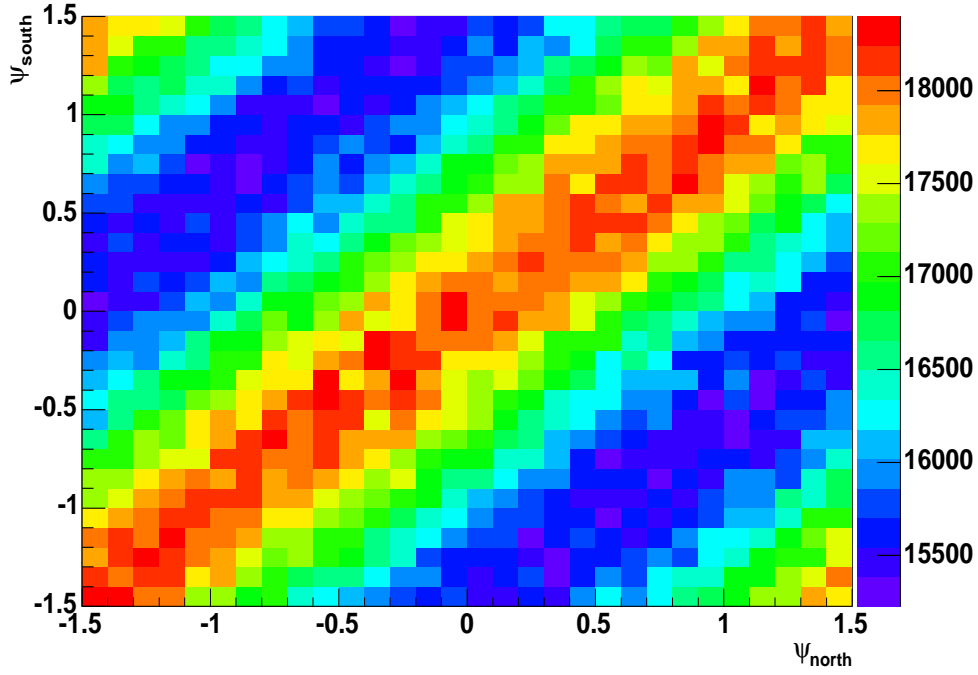


Figure 3.8: Azimuthal angle correlation of the measured reaction plane North side and South side of BBC.

tion plane should have an isotropic azimuthal distribution. Because of the possible azimuthal asymmetries in the BBC response, however, the measured reaction plane distribution is anisotropic. We use the following two step methods to correct the reaction plane. First the distribution of  $Q_x$  and  $Q_y$  are recentered by subtracting  $\langle Q_x \rangle$  and  $\langle Q_y \rangle$  over all events:

$$Q_x^{corr.} = \frac{Q_x - \langle Q_x \rangle}{\sigma_{Q_x}}, \quad (3.23)$$

$$Q_y^{corr.} = \frac{Q_y - \langle Q_y \rangle}{\sigma_{Q_y}}, \quad (3.24)$$

here  $\langle Q_{x,y} \rangle$  is the mean of  $Q_{x,y}$  and  $\sigma_{Q_{x,y}}$  is the width of  $Q_{x,y}$ . This method does not remove higher harmonic components for the reaction plane determination, and we apply an

additional correction method, the reaction plane flattening [50]. In this method, a flattening reaction plane is accomplished by using a shift,

$$n\psi^{\text{flat}} = n\psi_{\text{obs.}} + \Delta\psi, \quad (3.25)$$

where  $\Delta\psi$  is the correction factor for the reaction plane.  $\Delta\psi$  is determined by

$$\Delta\psi = \sum_n A_n \cos(2n\psi_{\text{obs.}}) + B_n \sin(2n\psi_{\text{obs.}}). \quad (3.26)$$

$A_n$  and  $B_n$  are defined by requiring the  $n^{\text{th}}$  Fourier moment of the new reaction plane ( $\psi^{\text{flat}}$ ) to vanish,

$$A_n = -\frac{2}{n} \langle \sin(2n\psi_{\text{obs.}}) \rangle, \quad (3.27)$$

$$B_n = \frac{2}{n} \langle \cos(2n\psi_{\text{obs.}}) \rangle. \quad (3.28)$$

Figure 3.8 shows the azimuthal angle correlation of the reaction plane between measured North side and South side of BBC. The plane is after applying the flattening corrections. A combined reaction plane, which is defined by weighted averaging the reaction plane angles obtained by the south side BBC and the north side BBC, is used to measure the  $v_2$  in this analysis.

### 3.5.4 Reaction Plane Resolution

As described in 3.5.2,  $v_2$  measured with respect to the “measured” reaction plane is corrected with the reaction plane resolution (Eq. 3.19). The true reaction plane can not be measured directly, therefore the reaction plane resolution is necessary. The reaction plane resolution [48, 49] is expressed as;

$$\langle \cos(n(\psi_{\text{meas.}} - \psi_{\text{true}})) \rangle = \frac{\sqrt{\pi}}{2\sqrt{2}} \chi_m \exp(-\chi^2/4) [I_0(\chi_m^2/4) + I_1(\chi_m^2/4)]. \quad (3.29)$$

where  $\chi_m = v_m/\sigma$  ( $= v_m\sqrt{2N}$ ) and  $I$  is the modified Bessel function. Figure 3.9 is shown the centrality dependence of the combined reaction plane resolution.

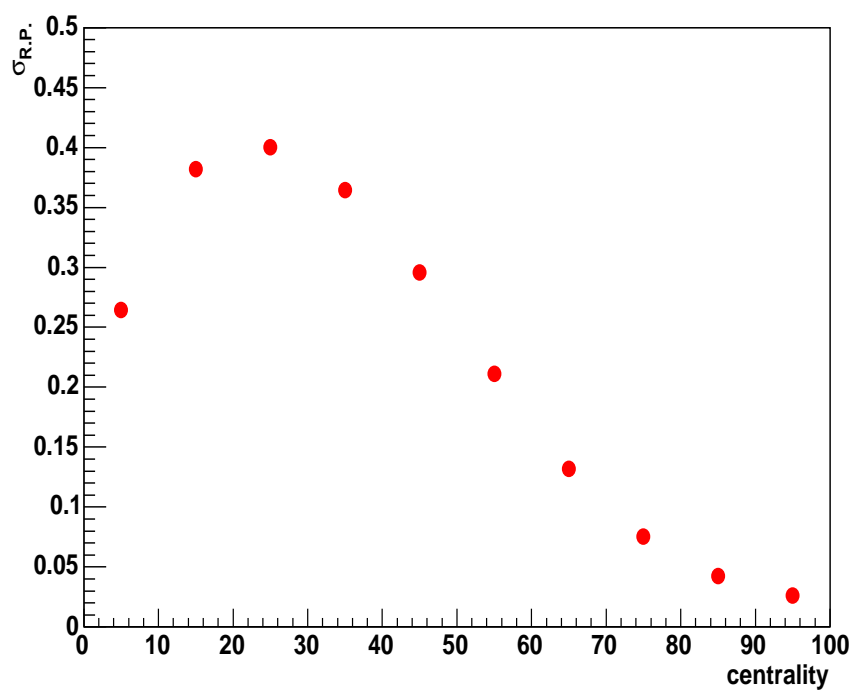


Figure 3.9: Centrality dependence of the combined reaction plane resolution that is determined by the BBCs.

## 3.6 Determination of non-photonic electron at PHENIX

### 3.6.1 Electron sources

As shown in Fig. 3.4, clear signals of electrons are obtained. The electrons produced by the collisions come from various sources.

1. Dalitz decays of  $\pi^0$ ,  $\eta$ ,  $\omega$ ,  $\phi$
2. Di-electron decays of  $\rho$ ,  $\omega$ ,  $\phi$
3. photon conversion
4. thermal di-leptons
5. Kaon decays ( $K_{e3}$ )
6. Heavy flavor decays (charm and beauty)

In this analysis, electrons from sources (1)-(4) are called “photonic” electron and (5),(6) are called “non-photonic” electron. The sources (1)-(5) are considered to be background. The key issue of the charm study via electron is the background subtraction. PHENIX has used two independent techniques “cocktail” [51] and “photon converter” [42] methods to subtract the electron backgrounds and get electrons from heavy flavor decays.

### 3.6.2 Cocktail method

In the cocktail method, background electrons are determined as a cocktail of electrons from background sources. Those background electrons are calculated with a Monte Carlo event generator of hadron decay. The most important background is the  $\pi^0$  decay ( $\pi^0$  Dalitz and photon conversion from  $\pi^0$  decay). For the study, the measured  $\pi^0$   $p_T$  spectra by PHENIX was used as an input for the generator. The other light mesons’s contribution,  $\eta$ ,  $\rho$ ,  $\omega$  and  $\phi$ , are also calculated. The spectral shapes of those light hadrons ( $h$ ) are obtained from the pion spectra by  $m_T$  scaling ( $p_T \rightarrow \sqrt{p_T^2 + M_h^2 - M_\pi^2}$ ). In addition, spectra of light mesons are normalized respected to the  $\pi^0$  as:  $\eta/\pi^0 = 0.48 \pm 0.03$  [52],  $\rho^0/\pi^0 = 1.0 \pm 0.3$ ,  $\omega/\pi^0 = 0.90 \pm 0.06$  [53],  $\phi/\pi^0 = 0.25 \pm 0.08$ . The background from  $\eta$  is the second largest contribution and the spectra determined by the above method is consistent with measured  $\eta$  spectra at PHENIX above 2.0 GeV/c. The internal and external conversion of direct photons are included in the cocktail using the measured direct photon spectrum at PHENIX. Kaon backgrounds in non-photonic electrons are also included in the cocktail. The backgrounds

are obtained by using measured Kaon spectrum. Figure 3.10 shows the background electron spectrum which is calculated by the hadron decay generator.

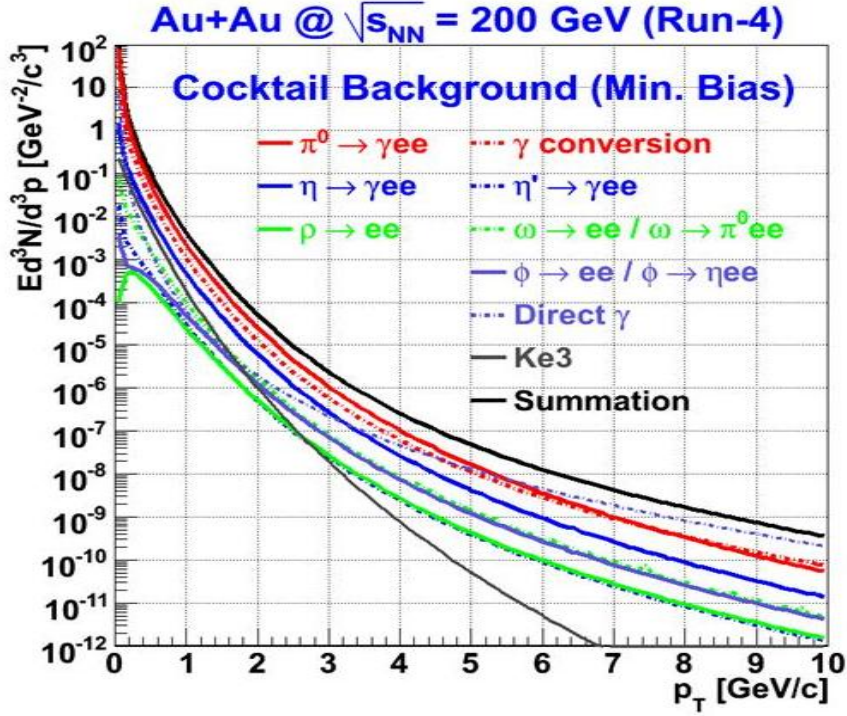


Figure 3.10:  $p_T$  distribution of the background electrons [54][55]. The background electrons are calculated by the hadron decay generator.

### 3.6.3 Photon converter method

In the photon converter method, electrons from photonic sources are experimentally determined by using a photon converter. The photon converter is a brass which has 1.7 % radiation length and is installed near the interaction point. The converter increases the yields of background by a fixed factor ( $R_\gamma \sim 2.3$ ), therefore we can separate signal and background electrons by comparing the electron spectra with and without the converter. The yield of electrons with and without converter can be written as,

$$\begin{aligned} N_e^{conv-in} &= R_\gamma N_e^\gamma + N_e^{non-\gamma}, \\ N_e^{conv-out} &= N_e^\gamma + N_e^{non-\gamma}, \end{aligned} \quad (3.30)$$

where  $R_\gamma$  is the ratio of the number of photonic electrons with and without the converter. The value of  $N_e^\gamma$  is the number of photonic electrons which come from Dalitz decays of

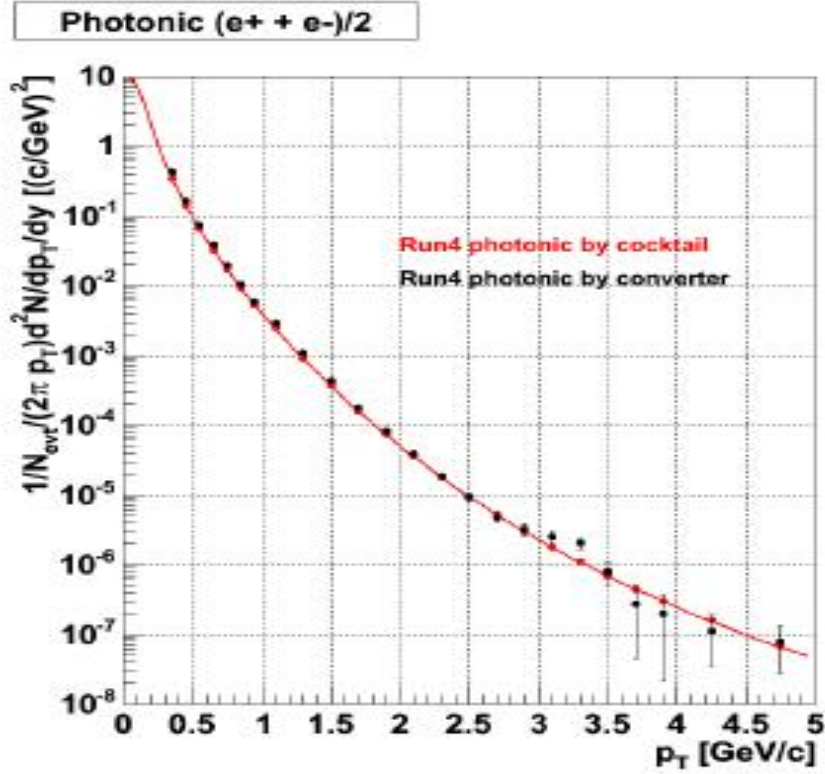


Figure 3.11: Invariant yield spectra of the photonic electron. The curve in the figure is the spectra from cocktail method and the closed circles is from the converter method.

light neutral mesons and photon conversions, and  $N_e^{non-\gamma}$  is the number of the non-photonic electrons mainly from heavy flavor decays. From Eq. 3.31 the yield of the photonic electron is obtained as;

$$N_e^\gamma = \frac{N_e^{conv-in} - N_e^{conv-out}}{R_\gamma - 1}. \quad (3.31)$$

Figure 3.11 shows the invariant yield of the photonic electrons in Au+Au collisions at  $\sqrt{s_{NN}} = 200$  GeV in the minimum bias events. The curve in the figure is the spectra from cocktail method. The photonic electron spectrum obtained both methods are consistent. Thus photonic backgrounds in the PHENIX is well understood.

### 3.6.4 Ratio of the non-photonic to photonic electrons $R_{NP}$

The yield of non-photonic electrons is determined by subtracting the yield of photonic electron from the inclusive electron yield,  $N_e^{conv-out} - N_e^\gamma$ . Figure 3.12 shows the invariant yield of the non-photonic electron [55]. At low  $p_T$  ( $p_T < 1.6$  GeV/c), photonic electrons determined by the converter method was subtracted, and determined with cocktail method was subtracted at high  $p_T$ . Figure 3.13 shows the transverse momentum dependence of the ratio of photonic and non-photonic electron ( $R_{NP} = N_e^{non-\gamma}/N_e^\gamma$ ). Above  $p_T = 1.5$  GeV/c,  $R_{NP}$  is larger than 1.0. It means that more than 50 % of electrons are originated from the non-photonic sources above  $p_T = 1.5$  GeV/c at PHENIX.

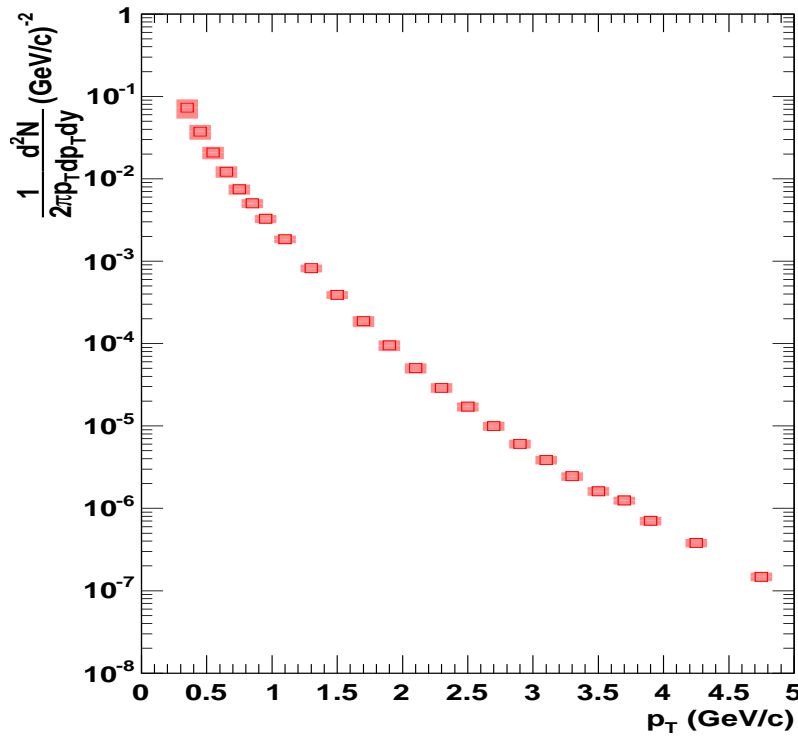


Figure 3.12: Invariant yield of the non-photonic electron measured in Au+Au collisions at  $\sqrt{s_{NN}} = 200$  GeV [55].



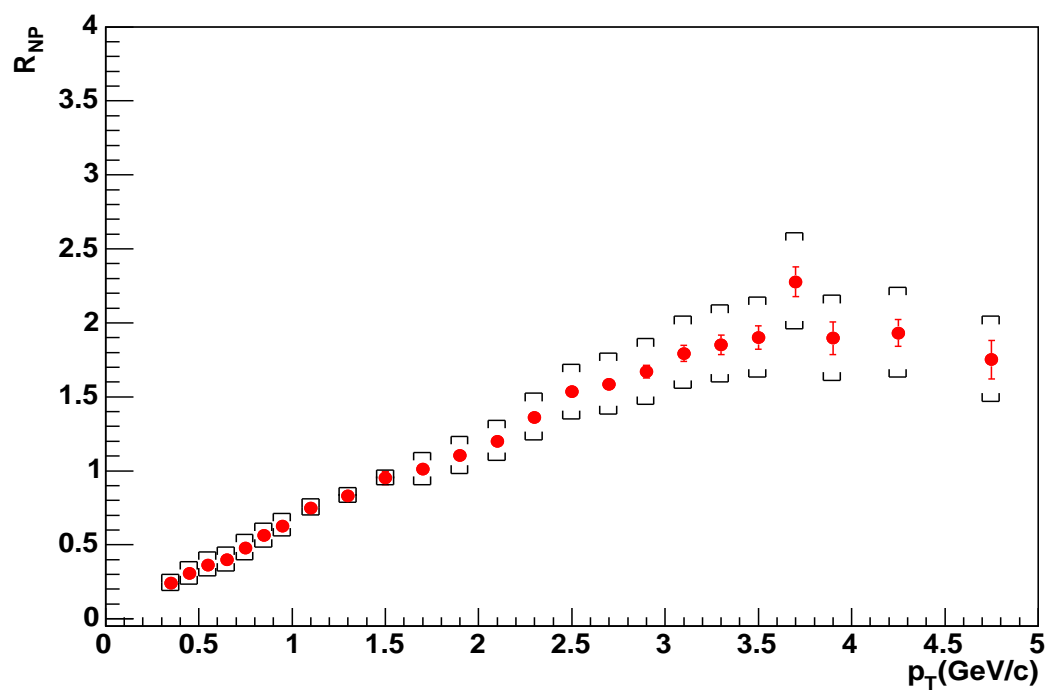


Figure 3.13: Transverse momentum dependence of the ratio of the number of non-photon electrons to the number of photon electrons ( $R_{NP} = N_e^{non-\gamma}/N_e^\gamma$ ).

# Chapter 4

## Experimental Results

In this chapter, we present a method to calculate the non-photonic electron  $v_2$  and show its transverse momentum dependence at mid-rapidity in  $\sqrt{s_{NN}} = 200$  GeV Au+Au collisions.

### 4.1 Inclusive Electron $v_2$

The measurement of inclusive electron  $v_2$  is the first step for the non-photonic electron  $v_2$  determination. Using the measured reaction plane with the BBCs, the inclusive electron  $v_2$  was calculated from Eq. 3.14,  $v_2 = \langle \cos(2(\phi - \Psi_{R.P.}^{meas.})) \rangle$ . As is described in the previous chapter,  $v_2$  measured with the reaction plane determined by experiment is smeared due to the finite reaction plane resolution. In this analysis, the inclusive electron  $v_2$  is measured with 10 % step of centrality bins and corrected for the reaction plane resolution as shown in Fig.3.9. Figure 4.1 shows the transverse momentum dependence of the inclusive electron  $v_2$  measured with 10 % step of centrality bins. The  $v_2$  was already corrected for the reaction plane resolution. As also described in the previous section, less than 10 % of the background remains due to accidental RICH associations. Such background was subtracted as;

$$\frac{dN}{d(\phi - \Psi_{R.P.})} = \frac{dN_{cand}^e}{d(\phi - \Psi_{R.P.})} - \frac{dN_{back}^e}{d(\phi - \Psi_{R.P.})}, \quad (4.1)$$

where  $N_{cand}^e$  is the number of electrons identified by RICH and  $N_{back}^e$  is the number of the backgrounds. The number of the backgrounds are obtained by "flip-and-swap" technique described in Chapter 3.4. The transverse momentum dependence of the inclusive electron  $v_2$  in Fig. 4.1 is obtained after subtracting the backgrounds. The inclusive electron  $v_2$  for the minimum bias events is calculated by the weighted average of the  $v_2$  measured with 10

% step of centrality bin as;

$$v_2^{min.bias}(p_T) = \frac{\sum_{cent} w(cent, p_T) v_2(cent, p_T)}{\sum_{cent} w(cent, p_T)}, \quad (4.2)$$

here  $v_2(cent, p_T)$  means the  $v_2$  measured with 10 % step of the centrality bin and  $w_{cent}(p_T)$  is the corresponding weight. The weight is determined by using the electron signals in each  $p_T$  bin, after the background subtractions. Figure 4.2 shows the inclusive electron  $v_2$  for the minimum bias event.

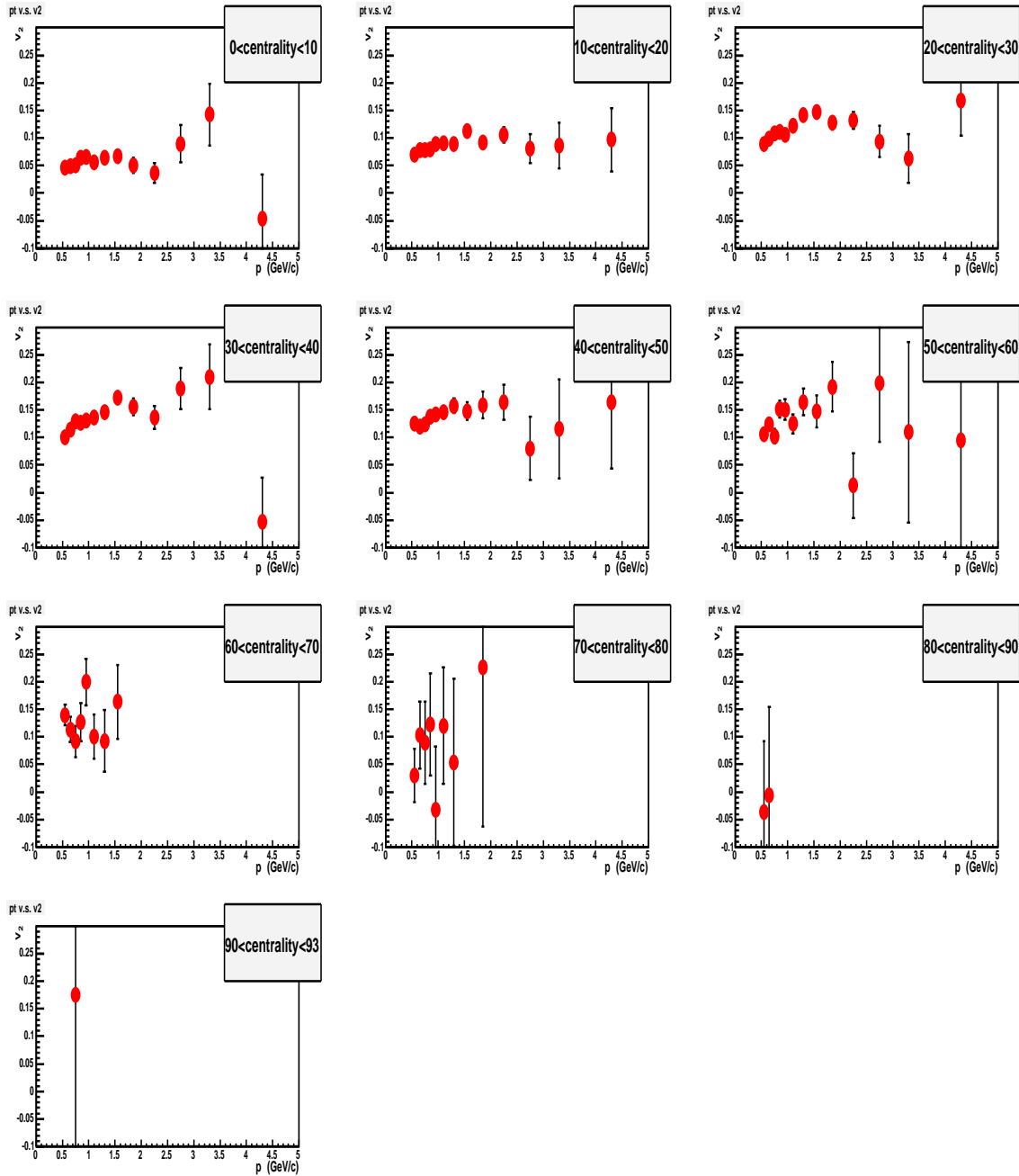


Figure 4.1: Transverse momentum dependence of the inclusive electron  $v_2$  measured with 10 % step of the centrality bin. The  $v_2$  was already corrected for the reaction plane resolution.

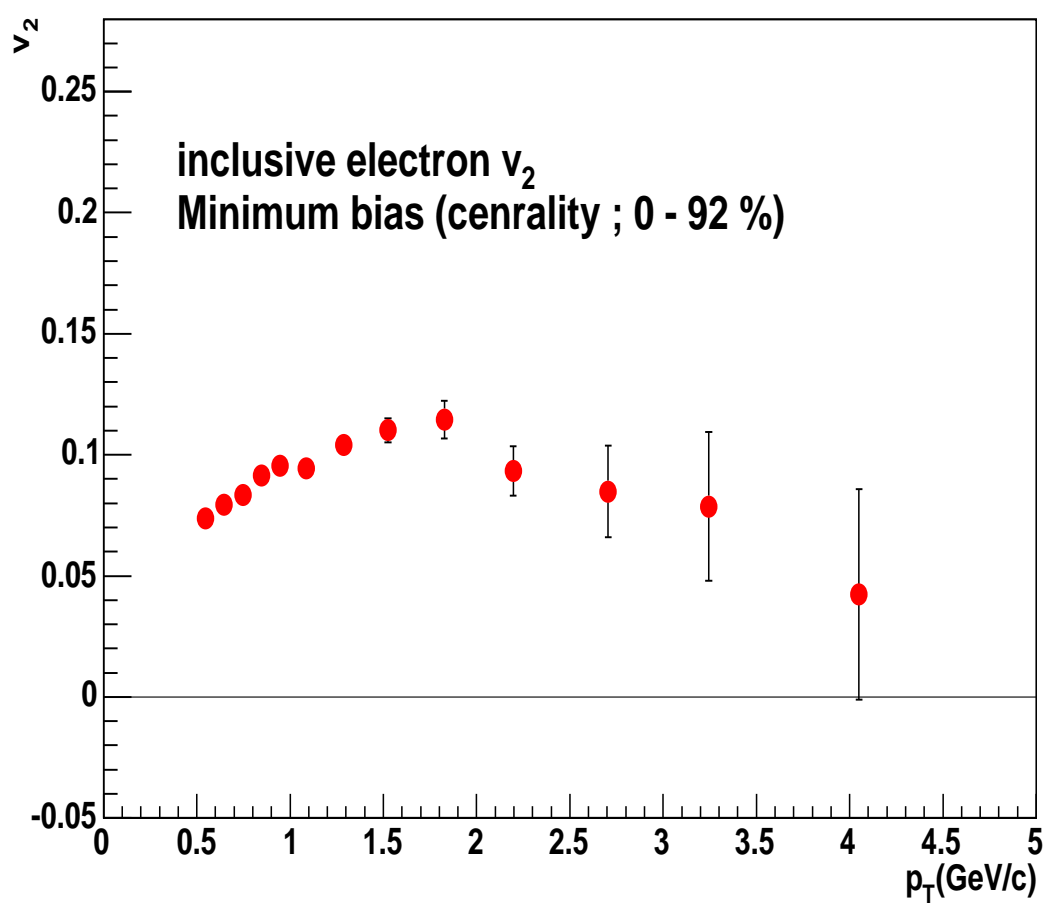


Figure 4.2: Inclusive electron  $v_2$  for the the minimum bias events as a function of  $p_T$ .

## 4.2 Non-photonic electron $v_2$

### 4.2.1 Method of non-photonic electron $v_2$ determination

The azimuthal distribution of electrons ( $dN_e/d\phi$ ) is the sum of the azimuthal distributions of photonic electrons ( $dN_e^\gamma/d\phi$ ) and non-photonic electrons ( $dN_e^{non-\gamma}/d\phi$ ):

$$\frac{dN_e}{d\phi} = \frac{dN_e^\gamma}{d\phi} + \frac{dN_e^{non-\gamma}}{d\phi}. \quad (4.3)$$

The second harmonic of the Fourier expansion of each azimuthal distribution is given as;

$$\begin{aligned} N_e(1 + 2v_{2e} \cos(2\phi)) &= N_e^\gamma(1 + 2v_{2e}^\gamma \cos(2\phi)) + N_e^{non-\gamma}(1 + 2v_{2e}^{non-\gamma} \cos(2\phi)) \\ &= (N_e^\gamma + N_e^{non-\gamma}) \left( 1 + 2 \frac{N_e^\gamma v_{2e}^\gamma + N_e^{non-\gamma} v_{2e}^{non-\gamma}}{N_e^\gamma + N_e^{non-\gamma}} \cos(2\phi) \right) \end{aligned} \quad (4.4)$$

where  $v_{2e}$  is the  $v_2$  of the inclusive electron,  $v_{2e}^\gamma$  is the  $v_2$  of the photonic electrons and  $v_{2e}^{non-\gamma}$  is the  $v_2$  of the non-photonic electrons. From Eq. 4.4, the relation between the number of electrons and the  $v_2$  are given as;

$$N_e v_{2e} = N_e^\gamma v_{2e}^\gamma + N_e^{non-\gamma} v_{2e}^{non-\gamma}. \quad (4.5)$$

Here  $N_e$  is sum of  $N_e^\gamma$  and  $N_e^{non-\gamma}$  ( $N_e = N_e^\gamma + N_e^{non-\gamma}$ ).

In this analysis the non-photonic electron  $v_2$  is calculated by two methods. The first method calculates the photonic electron  $v_2$  as a cocktail of contributions from photonic sources and subtracts it from inclusive data (Cocktail method). From Eq. 4.5, the non-photonic electron  $v_2$  can be expressed as

$$v_{2e}^{non-\gamma} = \frac{(1 + R_{NP})v_{2e} - v_{2e}^\gamma}{R_{NP}}, \quad (4.6)$$

where  $R_{NP}$  is defined as  $N_e^{non-\gamma}/N_e^\gamma$ . In the cocktail method, the photonic electron  $v_2$  is given as;

$$v_{2e}^\gamma = \sum \frac{N_{X \rightarrow e}}{N_e^\gamma} v_{2X \rightarrow e} \quad (4.7)$$

where  $X$  represents species of the parent particle,  $N_{X \rightarrow e}$  is the number of electrons decayed from the parent particle and  $v_{2X \rightarrow e}$  is the decay electron  $v_2$ . The decay electron  $v_2$  ( $v_{2X \rightarrow e}$ ) is calculated by using the measured parent  $p_T$  distributions and  $v_2$ .

The second method calculates the non-photonic electron  $v_2$  by using the inclusive electron  $v_2$  measured with and without the thin converter material (Converter method). The yield

of electrons with and without the converter can be written as,

$$\begin{aligned} N_e^{conv-in} &= R_\gamma N_e^\gamma + N_e^{non-\gamma}, \\ N_e^{conv-out} &= N_e^\gamma + N_e^{non-\gamma}, \end{aligned} \quad (4.8)$$

where  $R_\gamma$  is the ratio of the number of photonic electrons with and without the converter. From Eq. 4.8, the relation between the number of electrons and the  $v_2$  are given as;

$$\begin{aligned} N_e^{conv-in} v_{2e}^{conv-in} &= R_\gamma N_e^\gamma v_{2e}^\gamma + N_e^{non-\gamma} v_{2e}^{non-\gamma}, \\ N_e^{conv-out} v_{2e}^{conv-out} &= N_e^\gamma v_{2e}^\gamma + N_e^{non-\gamma} v_{2e}^{non-\gamma}, \end{aligned} \quad (4.9)$$

where  $v_{2e}^{conv-in}$  is the inclusive electron  $v_2$  measured with the converter and  $v_{2e}^{conv-out}$  is the inclusive electron  $v_2$  measured without the converter. From Eq. 4.9,  $v_{2e}^{non-\gamma}$  is obtained as;

$$v_{2e}^{non-\gamma} = \frac{R_\gamma(1 + R_{NP})v_{2e}^{conv-out} - (R_\gamma + R_{NP})v_{2e}^{conv-in}}{R_{NP}(R_\gamma - 1)}. \quad (4.10)$$

The photonic electron  $v_2$ ,  $v_{2e}^\gamma$ , is also obtained as;

$$v_{2e}^\gamma = \frac{(1 + R_{NP})v_{2e}^{conv-out} - (R_\gamma + R_{NP})v_{2e}^{conv-in}}{(1 - R_\gamma)}. \quad (4.11)$$

## 4.2.2 Determination of photonic electron $v_2$ by the cocktail method

In cocktail method, the photonic electron  $v_2$  is calculated as a cocktail of decay electron  $v_2$  from photonic sources. The most largest contribution to the photonic electrons is  $\pi^0$  Dalitz decay. It is about 60% contribution for the photonic electrons. The second largest contribution is  $\gamma$  conversion, mainly from  $\pi^0 \rightarrow \gamma\gamma$ , in material within the acceptance. The contribution from  $\gamma$  conversion is about 30%. The other important component is  $\eta$  Dalitz decay and direct  $\gamma$  decay.  $\eta$  Dalitz decay contribution is about 10% of the photonic component and the  $v_2$  is smaller than  $\pi^0$   $v_2$  at low  $p_T$ , therefore it is important to determined photonic electron  $v_2$  at low  $p_T$  region. Direct  $\gamma$  decay is negligibly small at low  $p_T$  region but more than 10% of the photonic electrons come from the direct  $\gamma$  at  $p_T > 3.5$  GeV/c. It is larger contribution than  $\eta$  Dalitz decay at the high  $p_T$  region. The reason why direct  $\gamma$  is also important in the cocktail calculation is the direct  $\gamma$   $v_2$  is much smaller than other  $v_2$ . In this calculation,  $\pi^0$ ,  $\eta$  and direct  $\gamma$  decays were taken into account. The other component is about a few %, therefore the contributions were ignored. The contribution of  $\pi^0$  Dalitz,  $\gamma$  conversion,  $\eta$  Dalitz decay and direct  $\gamma$  for photonic electron as a function of  $p_T$  is shown in Fig 4.3. The contributions are calculated from Fig.3.10. The details of decay electron  $v_2$  calculation from  $\pi^0$ ,  $\eta$  and direct  $\gamma$  decays are described in following sections.

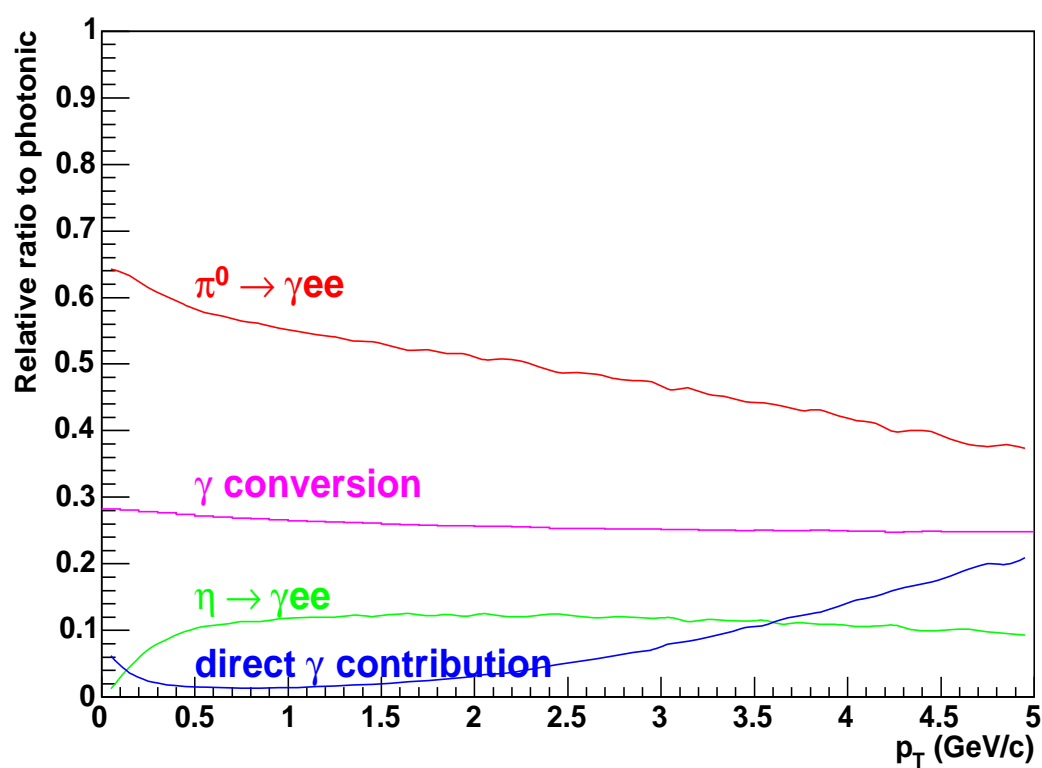


Figure 4.3: Relative contributions of electron sources ( $\pi^0$  Dalitz,  $\gamma$  conversion,  $\eta$  Dalitz and direct  $\gamma$ ) to the photonic electrons. The data is obtained from Fig 3.10.



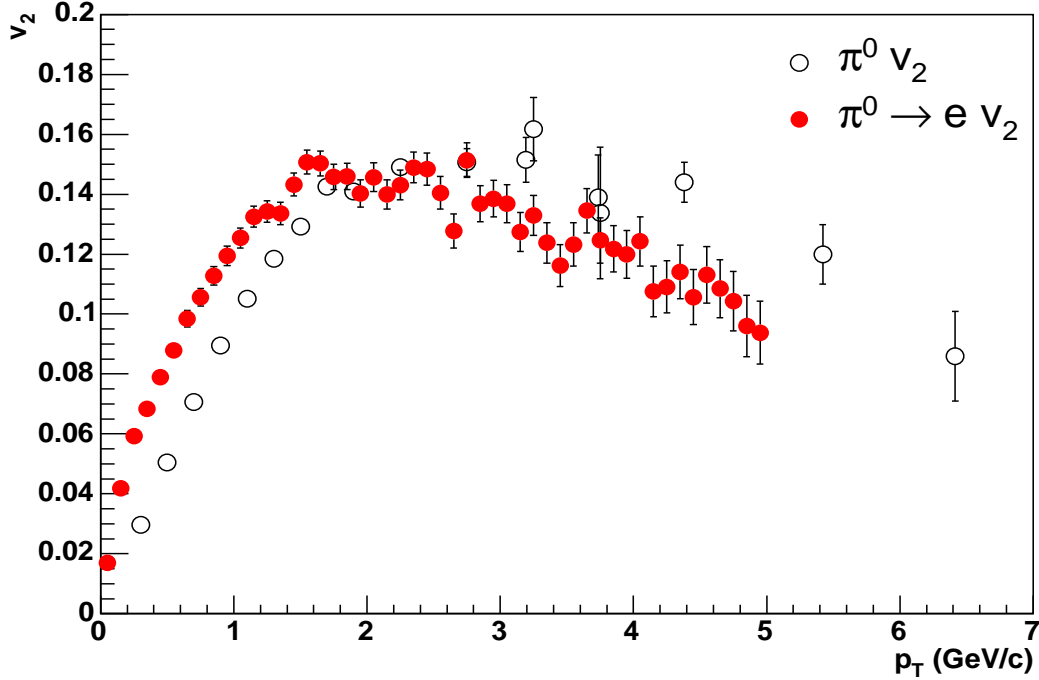


Figure 4.4:  $p_T$  dependence of electron  $v_2$  from  $\pi^0$  decay.

### electron $v_2$ from $\pi^0$

To calculate the decay electron  $v_2$  from  $\pi^0$ ,  $p_T$  spectra and  $v_2$  for the parent particles are needed. The PHENIX has been measured  $\pi^0$   $p_T$  spectrum [56] and we used this spectrum as an input for the  $\pi^0$  simulation. The input  $\pi^0$   $v_2$  was obtained from combined measured  $v_2$  for charged  $\pi$  [57] and  $\pi^0$  [58]. The simulation result of the  $\pi^0$  Dalitz decay is shown in Fig. 4.4. At low  $p_T$ , the decay electron  $v_2$  is larger than the parent  $v_2$ . Due to the fact that the decay opening angle of the  $\pi^0$  decay is small, the electron has about the same azimuthal angle as the parent, while at the same time the electron  $p_T$  is smaller than the  $\pi^0$   $p_T$ . Therefore the electron  $v_2$  at a given  $p_T$  corresponds to the larger  $v_2$  of the  $\pi^0$  at higher  $p_T$ . Thus the electron  $v_2$  is larger than the parent  $v_2$ . The  $v_2$  of conversion electrons of  $\pi^0$  decay photon should be almost exactly the same. Their  $v_2$  is originated from the  $v_2$  of  $\pi^0$ . And the angular correlation between the  $\pi^0$  direction and electron direction should be almost the same for Dalitz and the conversion photons. Therefore this result was used when we calculated the electron  $v_2$  from the photon conversion.

Component	$T_f(\text{MeV})$	$\rho_0$	$\rho_a$	$s_2$
mean	$168 \pm 19$	$0.794 \pm 0.026$	$0.067 \pm 0.008$	$0.071 \pm 0.007$
upper sys.	$140 \pm 19$	$0.776 \pm 0.026$	$0.056 \pm 0.008$	$0.067 \pm 0.007$
lower sys.	$225 \pm 22$	$0.856 \pm 0.026$	$0.094 \pm 0.011$	$0.080 \pm 0.007$

Table 4.1: Blastwave fitting result

### electron $v_2$ from $\eta$ Dalitz decay

For  $\eta \rightarrow e$  simulation, the input  $\eta$  spectrum for the simulation was obtained by using the measured  $\eta$  spectrum at PHENIX experiment [52]. The measurement is above 1.0 GeV/c therefore low  $p_T$  spectrum shape is evaluated by  $m_T$  scaling ( $p_T \rightarrow \sqrt{p_T^2 + M_\eta^2 - M_{\pi^0}^2}$ ) of the  $\pi^0$  spectrum, and the absolute normalization is scaled to match the measured  $\eta$  spectrum. In this analysis kaon  $v_2$  is used as input  $\eta$   $v_2$  because  $\eta$   $v_2$  has not been measured in RHIC. The reason why kaon  $v_2$  is used as an input for  $\eta$  simulation is described following. At low  $p_T$  region,  $v_2$  shows the clear mass dependence [19]. Therefore we estimated the mass effect by using a simple hydrodynamical mode, Blast wave model, which well describes the measured identified charged particle  $v_2$  at low  $p_T$  region [20]. In the Blast wave model,  $v_2$  is given as

$$v_2(p_T) = \frac{\int_0^{2\pi} d\phi_b \cos(2\phi_b) I_2(\alpha_t) K_1(\beta_t) (1 + 2s_2 \cos(2\phi_b))}{\int_0^{2\pi} d\phi_b I_0(\alpha_t) K_1(\beta_t) (1 + 2s_2 \cos(2\phi_b))}, \quad (4.12)$$

where  $I_0$ ,  $I_2$  and  $K_1$  are the modified Bessel functions, and  $\alpha_t(\phi_b) = (p_t/T_f) \sinh(\rho(\phi_b))$  and  $\beta_t = (m_t/T_f) \cosh(\rho(\phi_b))$ .  $\rho(\phi_b)$  is defined by  $\rho(\phi_b) = \rho_0 + \rho_a \cos(2\phi_b)$  where  $\phi_b$  is the azimuthal angle. The parameters ( $\rho_0$ ,  $\rho_a$  and  $s_2$ ) were obtained by fitting measured  $\pi$ , K, p  $v_2$  at in PHENIX [19]. The fitting parameters are shown in Table 4.1. The result of  $\eta$   $v_2$  calculated by the Blast wave model is shown as a red line in Fig. 4.5. The dashed lines are uncertainty of  $\eta$   $v_2$  which is calculated by the Blast wave model. It was obtained by fitting the systematic uncertainties of  $\pi^0$ , K and p  $v_2$  with Eq. 4.12. The mass effect between kaon and  $\eta$   $v_2$  is small and consistent within the uncertainty. At high  $p_T$  region, meson  $v_2$  can be same from the quark coalescence model prediction therefore  $\eta$   $v_2$  assumes to be the same  $v_2$  as kaon  $v_2$  at high  $p_T$  region.

The transverse momentum dependence of charged kaon  $v_2$  has measured up to around  $p_T = 3.0$  GeV/c and  $K_S^0$   $v_2$  has measured up to around  $p_T = 6.0$  GeV/c [22]. The K and  $K_S^0$   $v_2$  is consistent around 3.0 GeV/c, therefore the combined kaon and  $K_S^0$   $v_2$  was used as an input in this simulation. The result of electron  $v_2$  from  $\eta$  Dalitz is shown in Fig. 4.6.

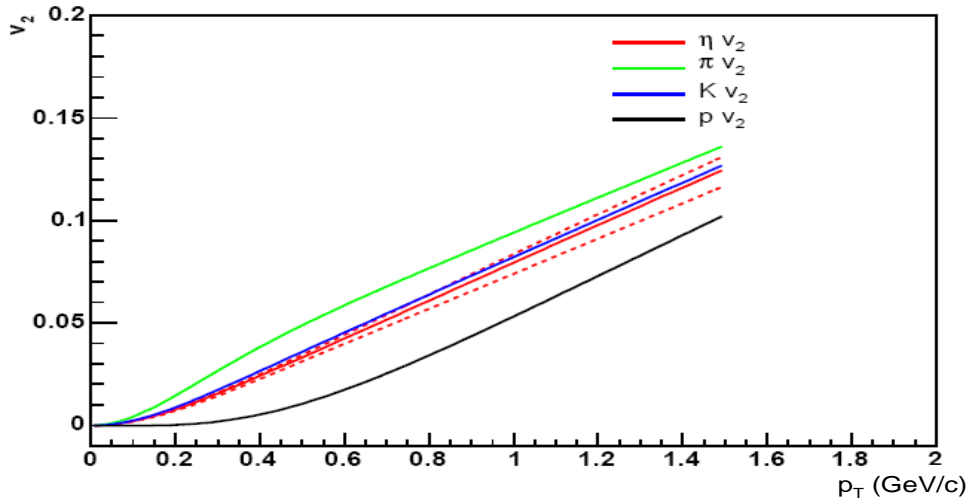


Figure 4.5:  $\eta v_2$  calculated by the Blast wave model. The dashed lines are the systematic uncertainties from the systematic uncertainty of  $\pi$ , kaon, proton  $v_2$ .

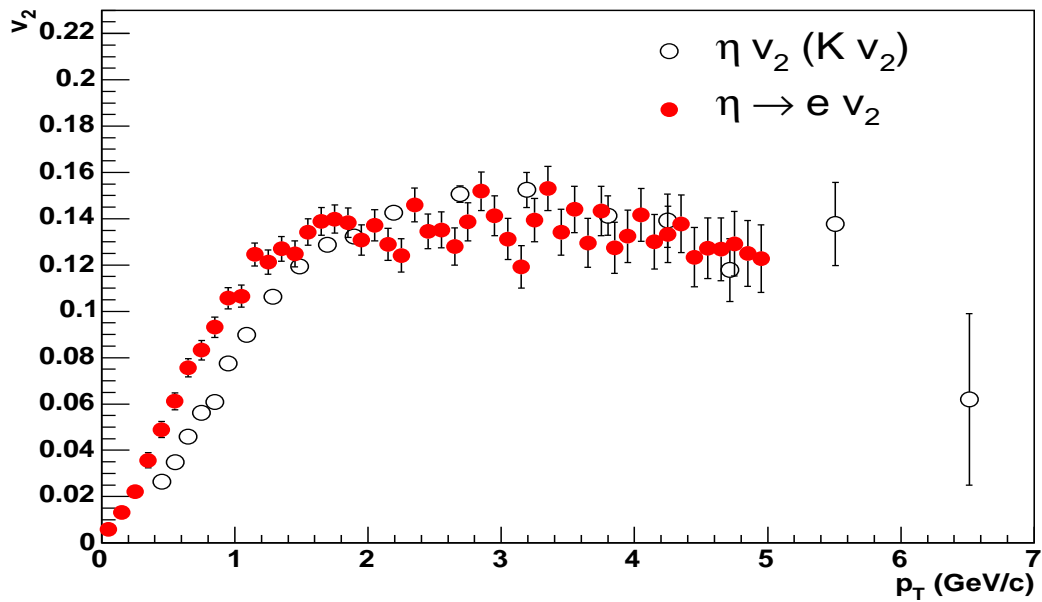


Figure 4.6:  $p_T$  dependence of electron  $v_2$  from  $\eta$  decay.  $\eta v_2$  was assumed same as kaon in this calculation.

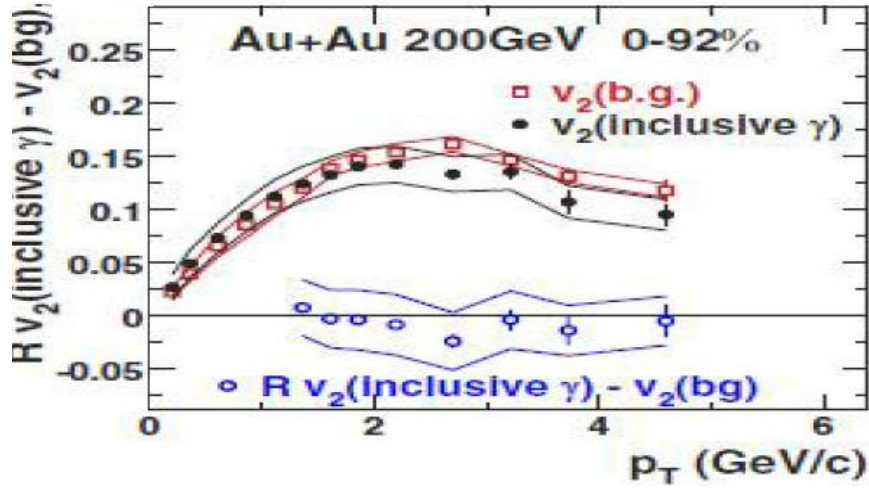


Figure 4.7: Direct  $\gamma v_2$  as a function of  $p_T$  measured at PHENIX. The closed circles are inclusive  $\gamma v_2$  and the open squares are background  $\gamma v_2$  mainly from  $\pi^0$  decay. The open circles corresponds to the direct  $\gamma v_2$  [59].

#### electron $v_2$ from direct $\gamma$

As shown in Fig. 4.3, direct  $\gamma$  contribution is larger contribution than  $\eta$  Dalitz decay at high  $p_T$  region. At  $p_T > 3.5$  GeV/c, more than 10% photonic electrons come from the direct  $\gamma$ . The direct  $\gamma v_2$  is expected zero because they do not interact with medium created by the collisions. The direct  $\gamma v_2$  has been measured at PHENIX [59]. Figure 4.7 shows the result of direct  $\gamma v_2$  measurement at PHENIX. In the analysis direct  $\gamma v_2$  was obtained by the same method, the cocktail method, of the non-photonic electron  $v_2$  measurement. First inclusive  $\gamma v_2$  was measured then background  $v_2$ ,  $\gamma v_2$  mainly from  $\pi^0$  decay, calculated by the simulation was subtracted from the inclusive  $\gamma v_2$ . The open symbols in the figure are corresponded to the direct  $\gamma v_2$ . The current result of direct  $\gamma v_2$  has large error bars but the result is consistent with zero. As shown previous in the simulations, the decay electron  $v_2$  correlates with the parent  $v_2$ . Therefore electrons from direct  $\gamma$  which has zero  $v_2$ , should have also zero  $v_2$ .

**photonic electron  $v_2$** 

Using the decay electron  $v_2$  calculated from above simulations and the relative contributions to photonic electron, photonic electron  $v_2$  was obtained. The result is shown in Fig. 4.8 as lines. The solid line is the mean of  $v_2$  and the dashed lines are  $1 \sigma$  systematic uncertainty of the cocktail method. The uncertainty from photonic electron  $v_2$  includes the systematic uncertainty of all parent  $v_2$  for the calculation. The  $\pi$   $v_2$  and  $K$   $v_2$  has about 5 % uncertainty without the reaction plane uncertainty. We apply this value to the uncertainty of the photonic electron  $v_2$ . For direct  $\gamma$   $v_2$ , we applied  $\Delta v_2 = \pm 0.1$  for the uncertainty.

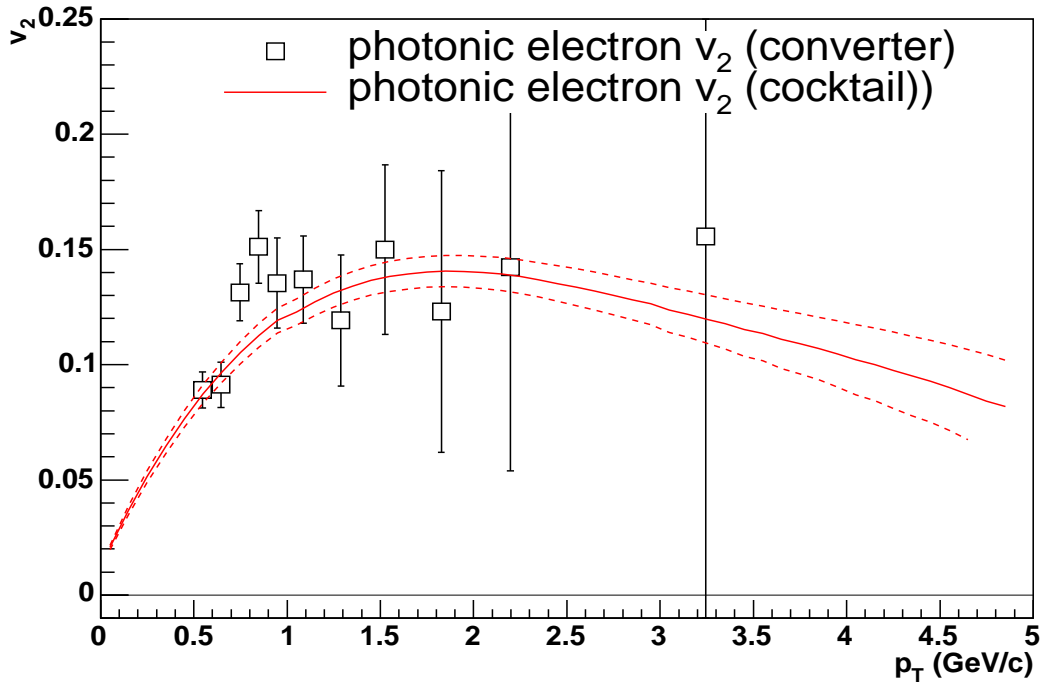


Figure 4.8:  $p_T$  dependence of photonic electron  $v_2$  obtained by the cocktail and converter method. The lines on the figure are photonic electron  $v_2$  calculated by the cocktail method. The solid line is the mean of  $v_2$  and the dashed lines are the systematic uncertainty of the cocktail method. The photonic electron  $v_2$  from converter is shown as boxes.

### Comparison of photonic electron $v_2$ by converter method

The photonic electron  $v_2$  was also determined by the converter method. Non-photonic electron and photonic electron  $v_2$  can be separated by using the inclusive electron  $v_2$  measured with ( $v_{2e}^{conv-in}$ ) and without ( $v_{2e}^{conv-out}$ ) converter as;

$$v_{2e}^{non-\gamma} = \frac{R_\gamma(1 + R_{NP})v_{2e}^{conv-out} - (R_\gamma + R_{NP})v_{2e}^{conv-in}}{R_{NP}(R_\gamma - 1)} \quad (4.13)$$

$$v_{2e}^\gamma = \frac{(1 + R_{NP})v_{2e}^{conv-out} - (R_\gamma + R_{NP})v_{2e}^{conv-in}}{(1 - R_\gamma)}. \quad (4.14)$$

Figure 4.9 shows the inclusive electron  $v_2$  with/without the converter. If the photonic electron  $v_2$  and non-photonic electron  $v_2$  is same, the  $v_2$  measured with/without the converter should be same. Due to the small statistics of the converter run,  $v_2$  measured with converter has a large statistical uncertainty. But it seems like  $v_2$  measured with the converter is larger than  $v_2$  measured without the converter. It indicates that non-photonic electron  $v_2$  is different from the photonic electron  $v_2$ . The photonic electron  $v_2$  obtained by the converter method is shown as open boxes in Fig. 4.8. The lines on the figure are photonic electron  $v_2$  calculated by the cocktail method. The photonic electron  $v_2$  obtained by the converter method has a large statistical error due to the small statistics of the converter run but the photonic electron  $v_2$  obtained by two methods are well consistent.

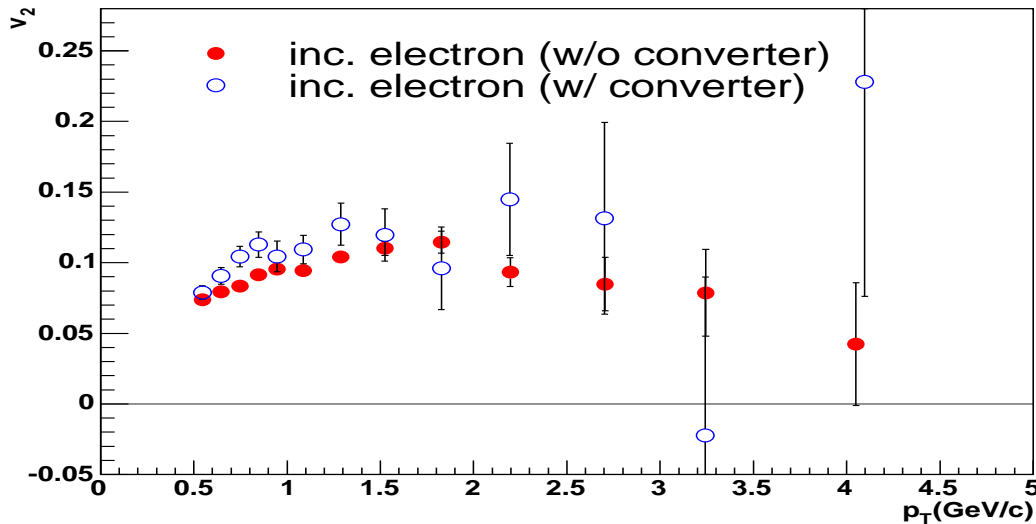


Figure 4.9: Inclusive electron  $v_2$  measured with/without converter (Minimum bias event).

### 4.2.3 Kaon decay background subtraction

Figure 4.10 shows the transverse momentum dependence of the non-photonic electron  $v_2$  after subtraction of the  $v_2$  of the photonic electron  $v_2$ . Due to the large statistical error of the photonic electron measured by the converter method, we used the  $v_2$  measured by the cocktail method in this analysis. At low  $p_T$  region the non-photonic electron contribution is small, therefore the inclusive electron  $v_2$  is similar to the background  $v_2$ . On the other hand, the inclusive electron  $v_2$  is getting similar to the non-photonic electron  $v_2$  with increasing  $p_T$  due to the good signal to background ratio at high  $p_T$ .

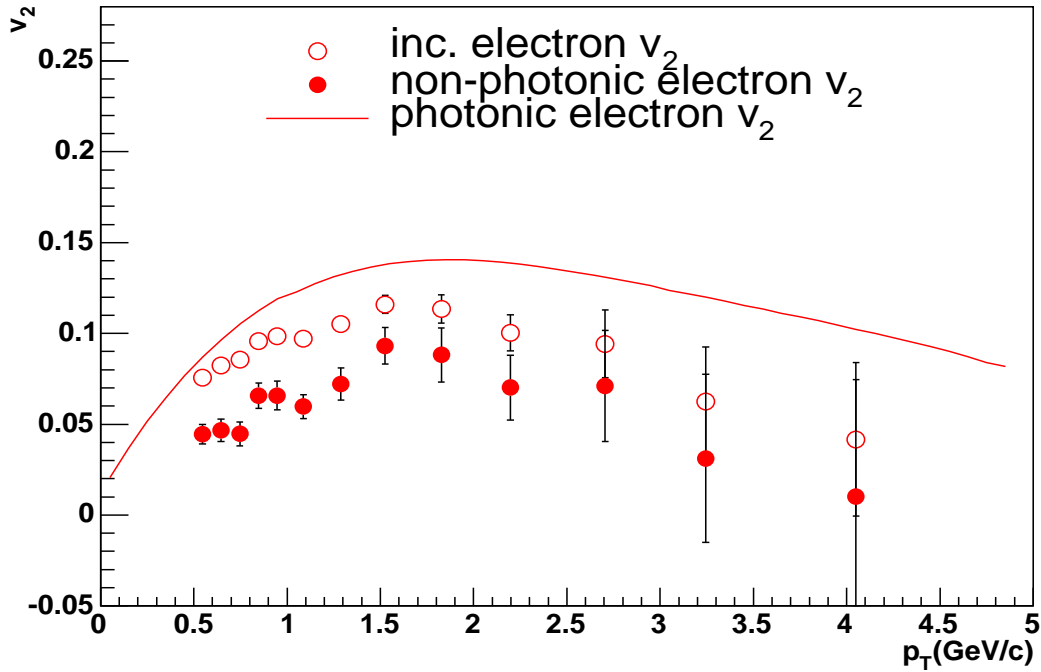


Figure 4.10:  $p_T$  dependence of the non-photonic electron  $v_2$  (closed circles) together with the inclusive electron  $v_2$  (open circles) and photonic electron  $v_2$  (solid line).

The background from kaon decays ( $K \rightarrow \pi e \nu$ ) still remains in the non-photonic electron  $v_2$  (Fig. 4.11). The contribution of kaon decays to the non-photonic electron yield is 18% at  $p_T = 0.5$  GeV/c and decreases to less than 5% for  $p_T > 1.0$  GeV/c [42]. In the analysis, the kaon decay contribution is also subtracted. The input kaon  $v_2$  is obtained from measured kaon  $v_2$  and  $K_S^0 v_2$  as described in the  $\eta v_2$  simulation study. The input kaon spectrum for the simulation is shown as a solid line in Fig. 4.12. At low  $p_T$  we used measured kaon spectrum

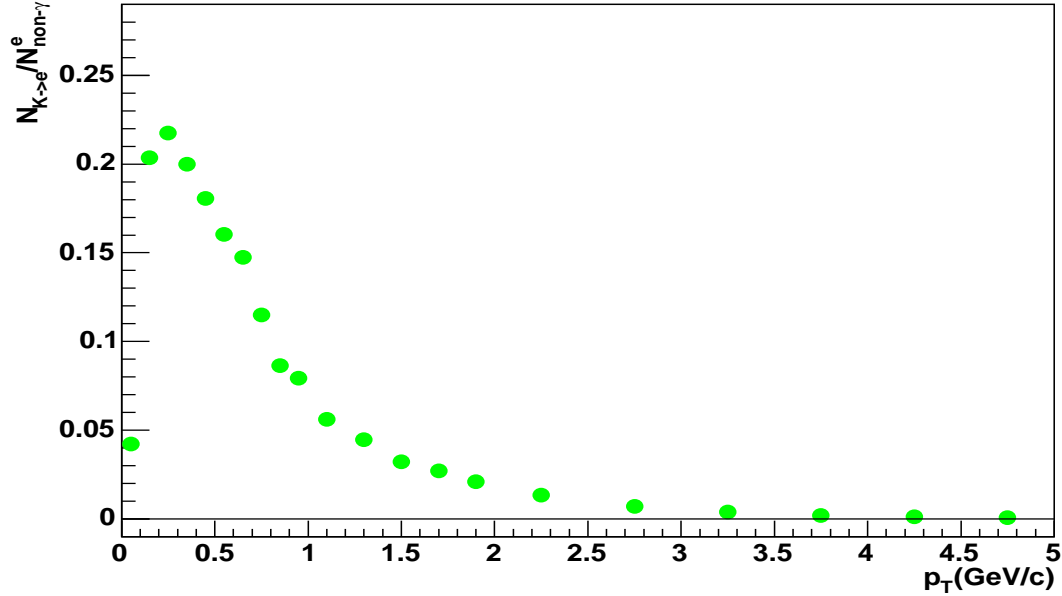


Figure 4.11: Contribution of kaon decays to the non-photon electron yield. The contribution is 18% at  $p_T = 0.5$  GeV/c and decreases to less than 5% for  $p_T > 1.0$  GeV/c.

[60] as the input for the simulation. At high  $p_T$  kaon spectrum has not been measured in heavy ion collisions, we assumed that the spectrum is same as  $\pi^0$  spectrum. We scaled the  $\pi^0$  spectra to connect around  $p_T = 2.0$  GeV/c with the measured kaon spectrum. To study the shape dependence of decay electron  $v_2$ , we also calculated the electron  $v_2$  assumed the kaon spectrum shape is an exponential function at  $p_T > 2.0$  GeV/c. The results are shown in Fig.4.13. The  $v_2$  which was calculated from the exponential shape is shown as blue points and the scaled  $\pi^0$  spectra is shown as red points. The difference between the decay electron  $v_2$  in the different assumptions at high  $p_T$  kaon spectrum is negligibly small.



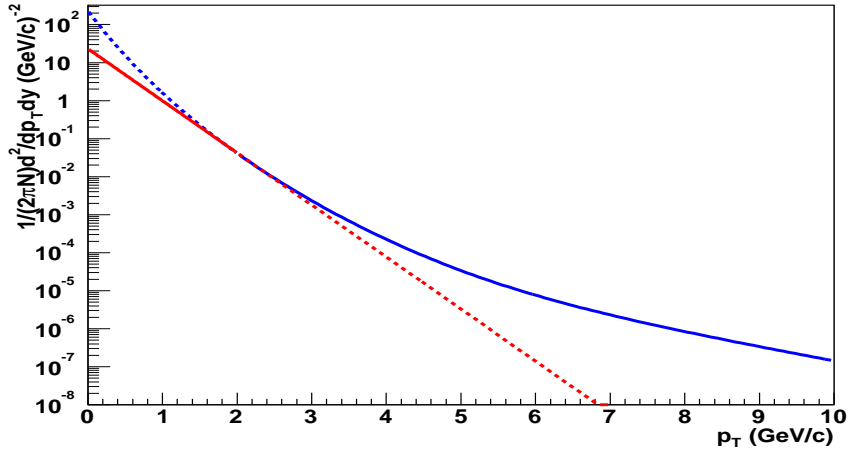


Figure 4.12: Input kaon  $p_T$  spectra for the kaon decay study simulation (the solid line). The spectrum at  $p_T > 2.0$  GeV/ $c$  we assumed that the shape is same as  $\pi^0$  spectrum. The  $p_T$  spectrum is obtained by the scaled  $\pi^0$  spectra connected around  $p_T = 2.0$  GeV/ $c$  to the low  $p_T$  kaon spectrum with the scale factor 0.55.

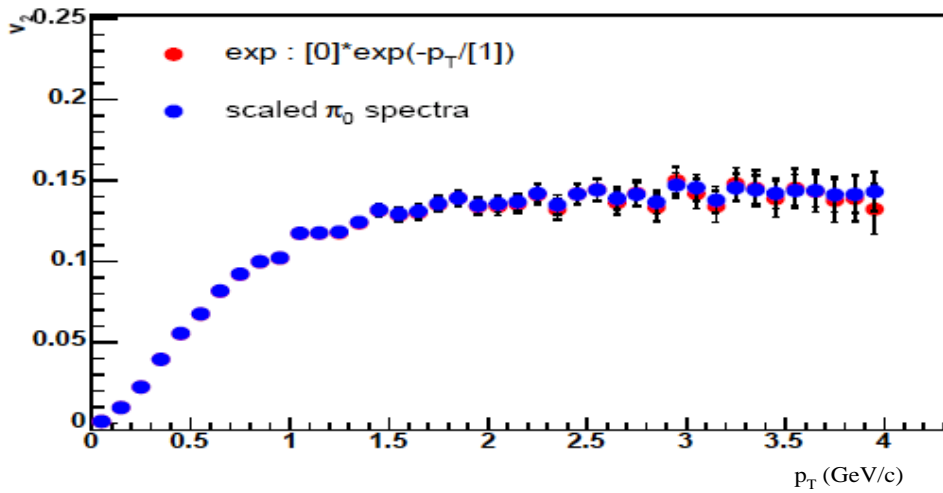


Figure 4.13:  $p_T$  shape dependence of electron  $v_2$  from kaon decay. The  $v_2$  which is calculated from the exponential shape (the dashed red line in Fig. 4.12) is shown as red points and the scaled  $\pi^0$  spectra (the blue line in Fig. 4.12) is shown as blue points. No shape dependence is seen in the electron  $v_2$ .

### 4.3 Systematic uncertainties

The systematic uncertainties of non-photonic electron  $\nu_2$  are summarized below.

- Reaction plane

The systematic uncertainty of the reaction plane is estimated by the measurements of the inclusive electron  $\nu_2$  with North side, South side and the combined reaction plane. The top side in the Fig. 4.14 show the inclusive electron  $\nu_2$  measured with three type of the reaction plane. The bottom plots is relative ratio respect to the  $\nu_2$  measured with combined reaction plane. The relative ratio is about 5 % and we apply it as the uncertainty from the reaction plane.

- Electron identification

The systematic uncertainty from the electron identification is estimated by measuring the inclusive electron  $\nu_2$  with the slightly changed the electron identification cut from the standard one. In this analysis we changed the parameters of  $E/p$  ( $E - p/p/\sigma$ ),  $n0$  and  $\chi^2/npe0$ . Figure 4.15 shows the comparison with the inclusive electron  $\nu_2$  measured with the standard cuts and with the slightly changed those cuts condition (these  $\nu_2$  are not corrected by reaction plane resolution). We apply the relative ratio respect to the standard cut as the uncertainty from the electron cut. The relative ratio of the  $E/p$  is about 2%, the  $n0$  is about 2% and the  $\chi^2/npe0$  is 1%. Therefore the total systematic uncertainty from electron identification is 3 %.

- Background  $\nu_2$

As described in the previous section, the uncertainties from photonic electron  $\nu_2$  come from  $\pi^0$  ( $\pi$ )  $\nu_2$  and kaon  $\nu_2$ . The  $\pi$  and K  $\nu_2$  has about 5 % uncertainty without the reaction plane. We apply this value to the uncertainty of the photonic electron  $\nu_2$ . We also apply 5 % for the  $\nu_2$  for kaon decay subtraction uncertainty.

- $R_{NP}$

The systematic uncertainty of the  $R_{NP}$  comes from the uncertainties of inclusive electron spectra and the subtracted background spectra [55]. The systematic uncertainty of the inclusive electron spectra includes the uncertainties in the geometrical acceptance, the reconstruction efficiency and the occupancy correction. The uncertainty in the converter subtraction,  $R_\gamma$  determination, and the cocktail subtraction are mainly originated from the systematic uncertainty of the input pion spectrum for the calculation.

The total systematic uncertainty is obtained by quadratic sum of above uncertainties.

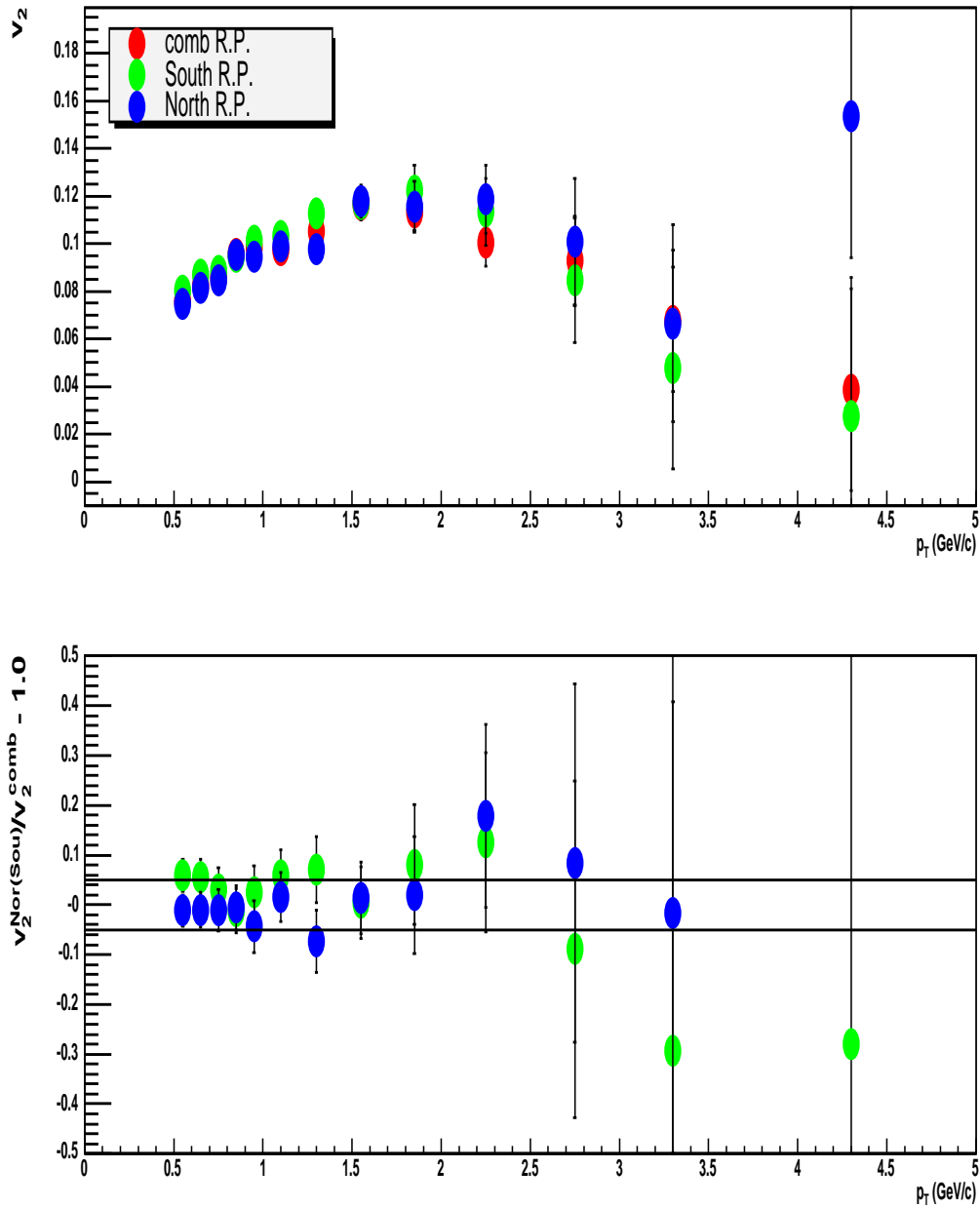


Figure 4.14: (Top) The inclusive electron  $v_2$  measured with three type of the reaction plane. (Bottom) The relative ratio respect to the  $v_2$  measured with combined reaction plane ( $v_2^{N(S)}/v_2^{comb}$ ).

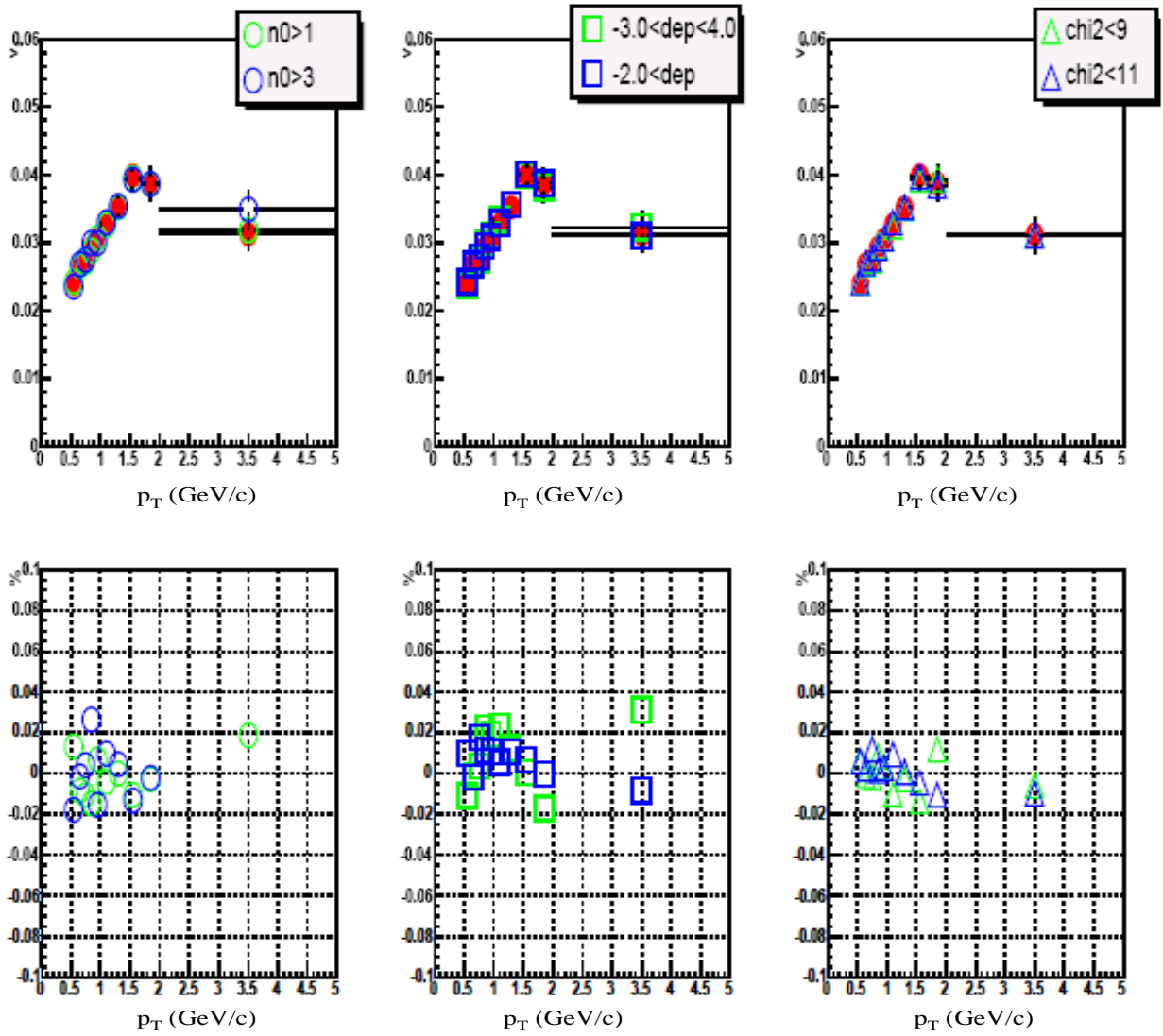


Figure 4.15: Systematic uncertainty from the electron identification is estimated by measuring the inclusive electron  $v_2$  with slightly change the condition of the standard electron identification cut (top). The relative ratio of the  $E/p$  is about 2%, the  $n_0$  is about 2% and the  $\chi^2/n_{pe0}$  is 1 % (bottom).

## 4.4 Result

Figure 4.16 shows the transverse momentum dependence of the non-photonic electron  $v_2$  in Au+Au collisions at  $\sqrt{s_{NN}} = 200$  GeV for the minimum bias events. The kaon decay contributions are subtracted in the figure. The vertical solid lines mean statistical error and the brackets mean  $1 \sigma$  systematic uncertainty of the non-photonic electron  $v_2$ .

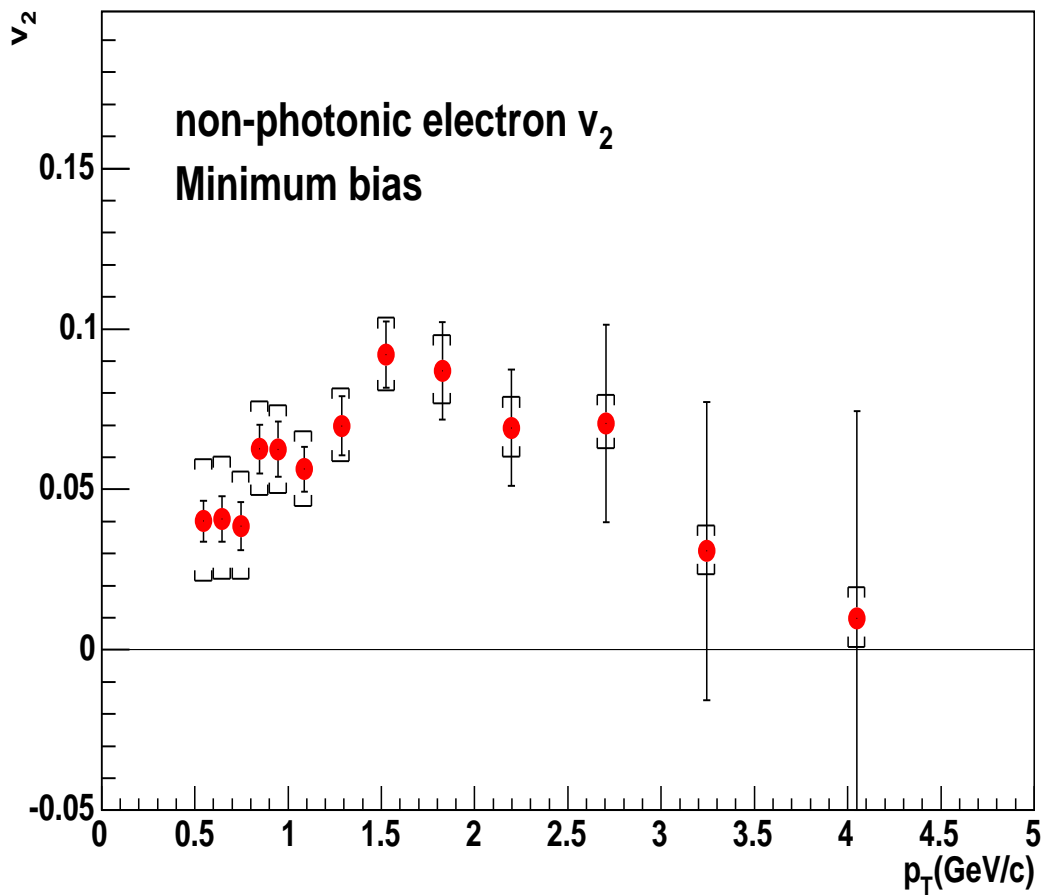


Figure 4.16: Transverse momentum dependence of non-photonic electron  $v_2$  in Au+Au collisions at  $\sqrt{s_{NN}} = 200$  GeV for the minimum bias events. The vertical solid lines mean statistical error and the brackets mean  $1 \sigma$  systematic uncertainty of the non-photonic electron  $v_2$ .

# Chapter 5

## Discussions

### 5.1 Non-photonic electrons

Charm quark production has been studied via the non-photonic electron yields in the PHENIX experiment. Since charm is only produced in the initial collisions via gluon fusions, the total yield should be scaled by the number of nucleon-nucleon binary collisions ( $N_{\text{coll}}$ ). The left figure in Fig. 5.1 shows  $dN/d\eta$  ( $0.8 < p_T < 4.0$  GeV/c)/ $N_{\text{coll}}$  of the non-photonic electron vs.  $N_{\text{coll}}$  for the minimum bias and five centrality bins together with  $p + p$  collisions [42]. The data are fitted with  $AN_{\text{coll}}^\alpha$  and it found  $\alpha = 0.938 \pm 0.075(\text{stat.}) \pm 0.018(\text{sys.})$ . The centrality dependence of the total non-photonic electron yield is consistent with  $N_{\text{coll}}$  scaling, as expected for the charm production. The right figure in Fig. 5.1 shows invariant yields of non-photonic electrons for minimum bias events and in five centrality classes, 0-10 %, 10-20 %, 20-40 %, 40-60 %, and 60-90 % [55]. The curves in the figure are the result of a FONLL calculation from heavy flavor decay ( $c$  and  $b$ ) [40] normalized to the  $p + p$  data [39]. For all centralities, the non-photonic electron spectra measured in Au+Au collisions agree well with  $p + p$  difference. As we discuss later, a suppression with respect to  $p + p$  reference develops towards high  $p_T$  in central collisions suggests energy loss of charm quarks in the dense matter. The dominant source of the  $p + p$  reference is charm decay (Fig. 1.14). We concluded that dominant source of electrons after background subtraction is "charm" quark.

Thus the non-photonic electron  $v_2$  can be reflected to the azimuthal anisotropy of charm quarks. As shown in the Fig. 4.16, a clear non-zero non-photonic electron  $v_2$  has been observed. We calculated the confidence level for the non-zero  $v_2$ . We assumed that the data of measured non-photonic electron  $v_2$  follows a Gaussian distribution and the  $\sigma$  was obtained by calculating quadratic sum of the statistical and systematic errors of the non-photonic electron  $v_2$  assumed these errors are independent. The result is shown in Fig.5.2

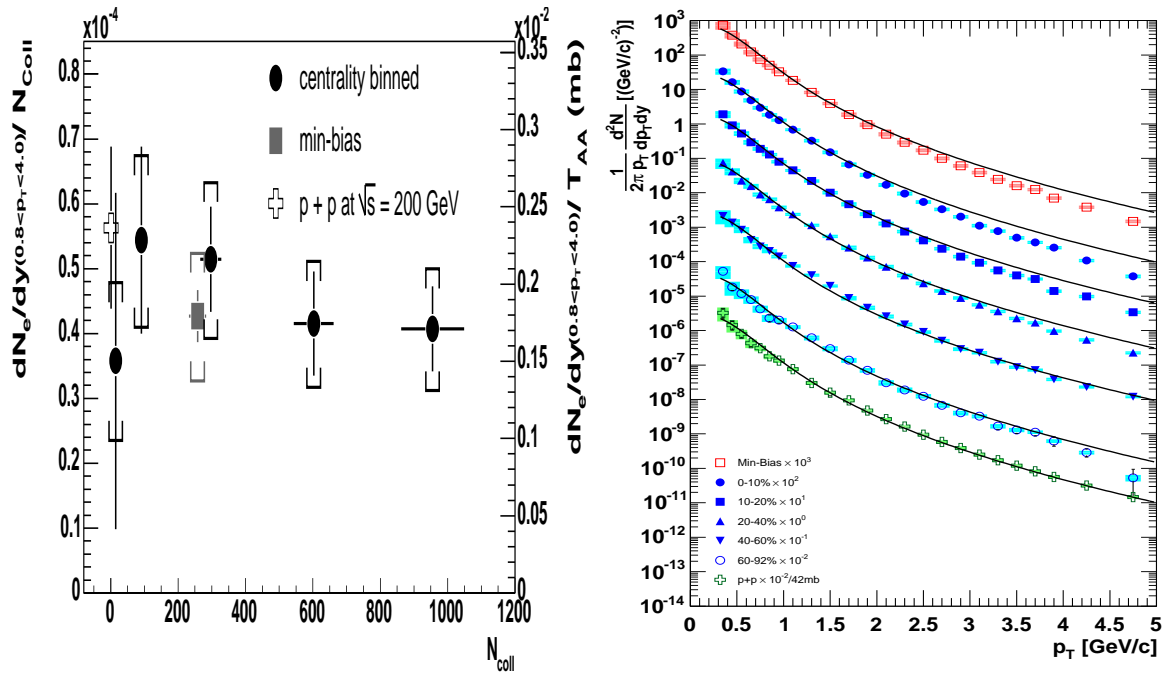


Figure 5.1: (Left) Non-photonic electron yield ( $0.8 < p_T < 4.0$  GeV/c) measured in Au+Au collisions at 200 GeV [42] scaled by  $N_{\text{coll}}$  as a function of  $N_{\text{coll}}$ . Normalizing by the nuclear overlap function obtained charm electron cross section per  $N + N$  collisions (right-hand scale). (Right) Invariant yields of electrons from heavy flavor decays for different Au+Au centrality [55], scaled by powers of ten for clarity. The solid lines are the result of a FOMLL calculation of heavy flavor decay normalized to the  $p + p$  data [39] for each centrality class.

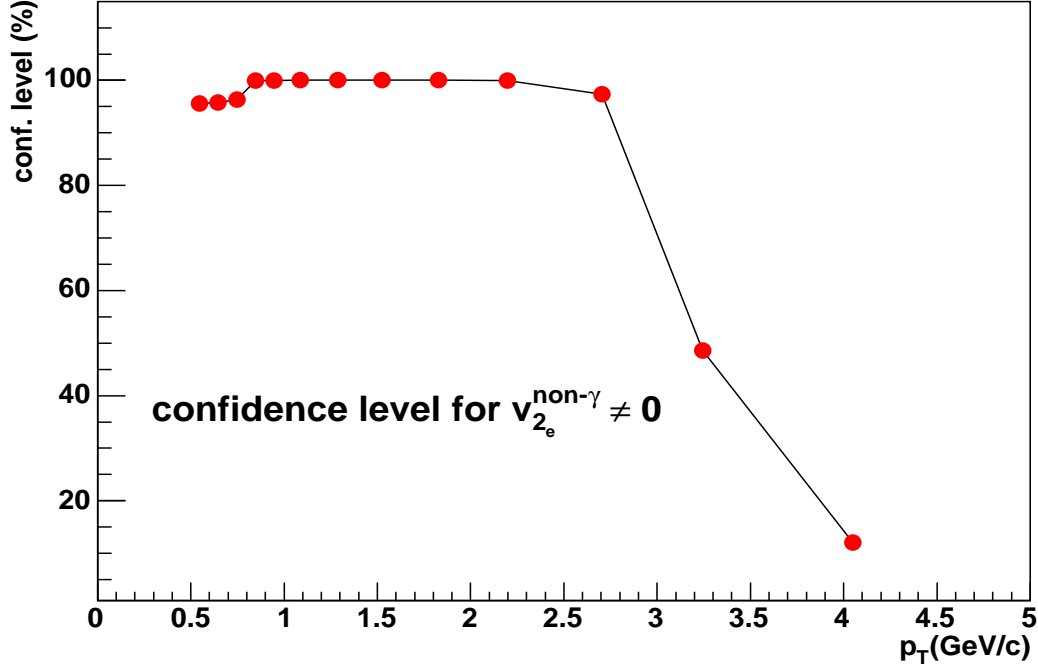


Figure 5.2:  $p_T$  dependence of the confidence level for the non-zero non-photonic electron  $v_2$ .

as a function of  $p_T$ . We found that the confidence level is more than 90 % for a non-zero non-photonic electron  $v_2$  below  $p_T < 2.7$  GeV/c. Figure 5.3 shows the comparison with non-photonic electron  $v_2$  and charged pion  $v_2$ . The trend of the non-photonic electron  $v_2$  is similar to the  $\pi$   $v_2$ , increasing with  $p_T$  up to about 1.5-2.0 GeV/c and then saturate or slightly reduces with increasing  $p_T$ ,

One of the interesting observation of the non-photonic electron  $v_2$  is that the  $v_2$  is smaller than the pion in whole  $p_T$  range. This feature of the non-photonic electron  $v_2$  is different from the other identified particle  $v_2$  at high  $p_T$ . As we showed in the introduction, the identified particle  $v_2$  ( $\pi$ , K, p) shows the mass dependence, the heavier particle has smaller  $v_2$  than the lighter particle, at low  $p_T$  region. But identified particles have same  $v_2$  ( $v_2 \sim 0.15$ ) around  $p_T = 1.5$  GeV/c. On the other hand, the maximum  $v_2$  of the non-photonic electron  $v_2$  is about 0.1 and it does not have same  $v_2$  as pion, kaon and proton. The solid line on the figure is a model calculation based on a quark coalescence model.<sup>1</sup> In the model, charm quark  $v_2$  is assumed same as u quark  $v_2$ . The model predicts that the maximum  $v_2$  for

<sup>1</sup>The solid line in the Fig. 5.3 is obtained with  $a = 1.0$  and  $b = 1.0$  in Eq. 5.7.



electron from charm decay is about 0.1 though charm quark has same  $v_2$  as u quark  $v_2$ . The details about the model is described later in this chapter.

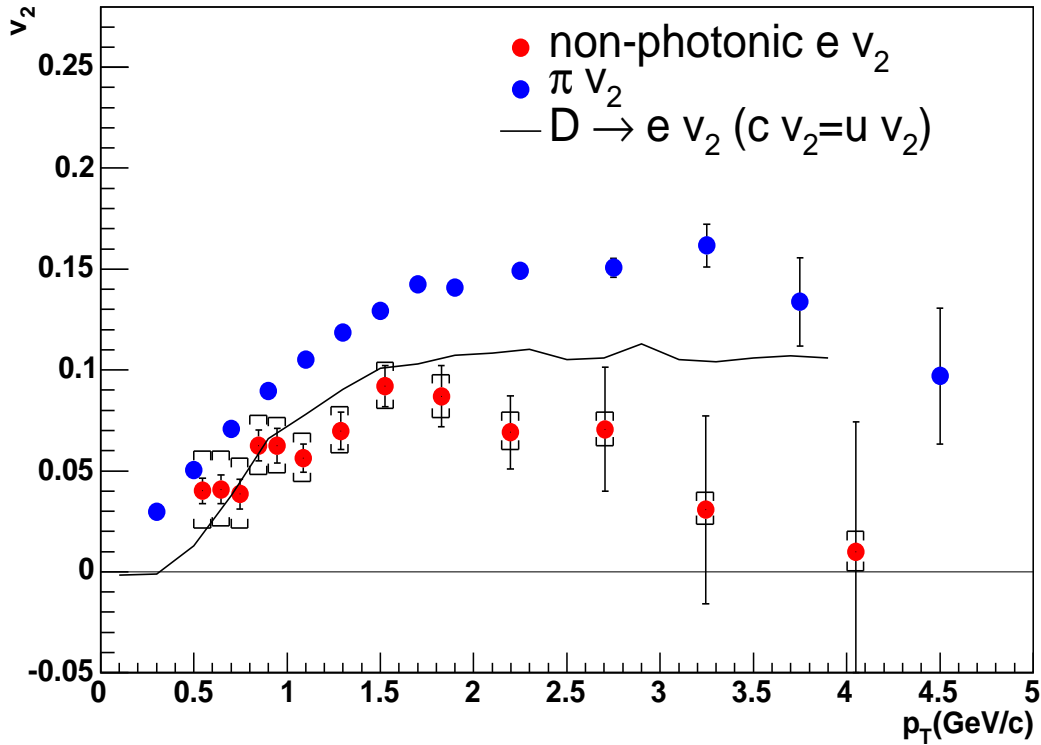


Figure 5.3: Comparison of the non-photonic electron  $v_2$  with pion  $v_2$ . The dashed line on the figure is the electron  $v_2$  from charm decay assuming charm has same  $v_2$  as u quark.

## 5.2 Kinematics of $D$ meson decay and $v_2$

As discussed in the previous section, the main source of the non-photonic electron is  $D$  meson. Thus the non-photonic electron  $v_2$  would be kinematically determined and allow us to study  $D$  meson  $v_2$ . The issue of the  $D$  meson  $v_2$  via electron measurement is that electrons originating from semileptonic decays of  $D$  mesons might have a significant angular deviation from the original  $D$  meson direction due to their large mass difference. If the angular deviation is large, the non-photonic electron does not reflect parent  $D$  meson  $v_2$  because electron  $v_2$  is largely smeared by the angular deviation. We studied the effect on  $v_2$  with a Monte Carlo simulation. The right hand figure in Fig. 5.4 shows the decay angle

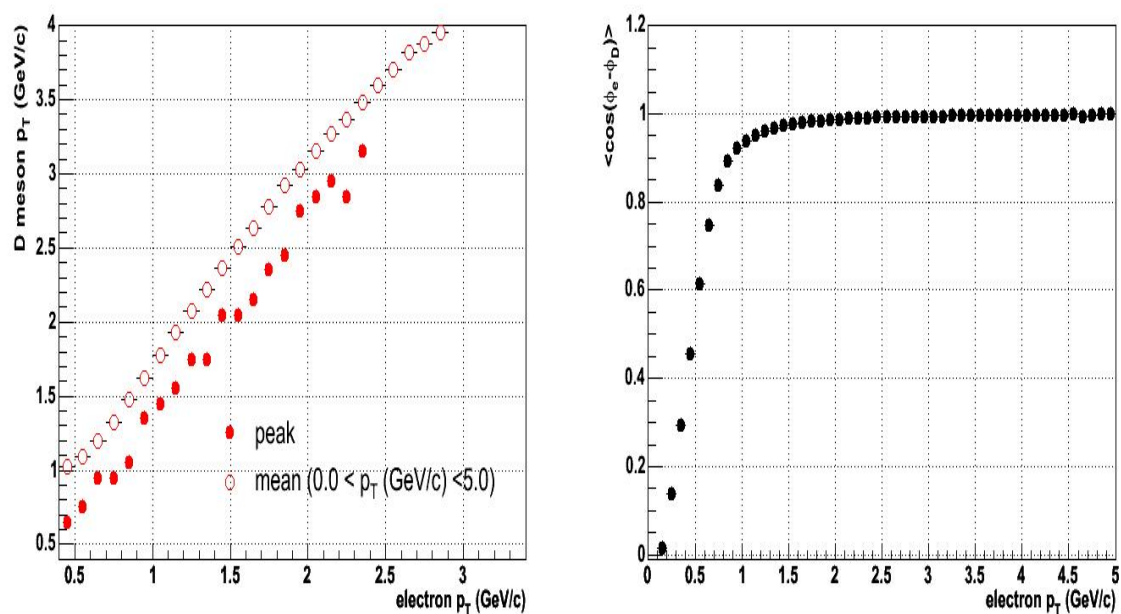


Figure 5.4: (Left) Momentum correlation between  $D$  meson and the decay electrons. The open circles represent the mean  $p_T$  of  $D$  meson momentum distribution for the given electron momentum and closed data points represent the peak of the  $D$  meson momentum distribution. (Right)  $p_T$  dependence of the decay angle correlation between  $D$  mesons and the decay electrons.

correlation between  $D$  mesons and the decay electrons ( $\cos(\phi_e - \phi_D)$ ) as a function of  $p_T$  of decay electrons. The result suggests that below  $p_T = 1.0$  GeV/ $c$  the angular deviation is large so that the decay electrons are not emitted to the same direction of parent  $D$  mesons. On the other hand, above 1.0 GeV/ $c$  the angular deviation is very small so that the decay electrons are emitted to the same direction of parent  $D$  mesons. Thus the non-photonic electron  $v_2$  above 1.0 GeV/ $c$  well reflects the  $v_2$  of  $D$  meson.

The corresponding electron momentum above 1.0 GeV/ $c$  is about 1.5 GeV/ $c$  to  $D$  meson (the left hand figure in Fig. 5.4). Thus a non-zero non-photonic electron  $v_2$  leads that the  $D$  meson  $v_2$  is also a non-zero at the intermediate  $p_T$  region. Furthermore,  $v_2$  of  $D$  meson via non-photonic electron  $v_2$  has been studied by a simple model calculations. We do not know the real shape of  $D$  meson  $v_2$ , therefore we assumed various  $p_T$  depend shape of  $D$  meson  $v_2$ . In this calculation we defined  $D$  meson  $v_2$  as;

$$v_2^D(p_T) = a \times f(p_T), \quad (5.1)$$

where  $f(p_T)$  is the  $p_T$  depend shape of  $D$  meson  $v_2$  and  $a$  is a scale factor for  $f(p_T)$ . We calculated  $v_2$  for the decay electrons from the  $D$  meson which have  $v_2$  defined as above equation with a Monte Carlo simulation. Then we determined the best scale parameter with chi-squared test with the measured non-photonic electron  $v_2$ ;

$$\chi^2 = \Sigma \{ (v_2^{non-\gamma} - v_2^{D \rightarrow e}) / \sigma_{v_2} \}^2, \quad (5.2)$$

where  $v_2^{non-\gamma}$  is the measured non-photonic electron  $v_2$ ,  $v_2^{D \rightarrow e}$  is the electron  $v_2$  obtained from the Monte Carlo simulation of the  $D$  meson decay, and  $\sigma$  is the statistical and systematic error of the measured non-photonic electron  $v_2$ . In the calculation  $\pi$ , K, p and  $\phi$   $v_2$  were used for the  $p_T$  depend shape of  $D$  meson  $v_2$ . These  $v_2$  are the measured  $v_2$  in Au+Au collisions at  $\sqrt{s_{NN}} = 200$  GeV. Recently PHENIX has published the results that identified particles  $v_2$  are well scaled with  $m_T - m$  [57]. We also tested  $D$  meson  $v_2$  with this transverse kinetic energy scaling law in this study. Figure 5.5 shows the  $\chi^2/ndf$  ( $ndf = 13$ ) as a function of the scale factor ( $a$ ) and Fig. 5.6 shows the  $1 \sigma$  bands for each of the five assumed  $v_2$  shapes. The  $\chi^2$  test shows that  $D$  meson  $v_2$  shape, which shows the saturation around  $p_T = 2.0$  GeV/ $c$  for meson ( $\pi$ , K,  $\phi$ ), well represent the shape for the non-photonic electron  $v_2$ . Therefore  $D$  meson might be prefer to have a meson like  $v_2$  shape (saturate around 2.0 GeV/ $c$ ). The best shape for the  $D$  meson  $v_2$  expected by the non-photonic electron  $v_2$  is a pion  $v_2$  shape. Figure 5.7 shows the  $D$  meson  $v_2$  obtained above method. The closed data points represent the most suitable  $D$  meson  $v_2$  ( $\chi^2$  minimum) from the calculation, and the shared band means  $\chi^2/ndf$  is less than 2.0. Based on the calculation, we found that  $D$  meson  $v_2$  expected from the non-photonic electron  $v_2$  is  $0.09 \pm 0.03$ . The open circles on

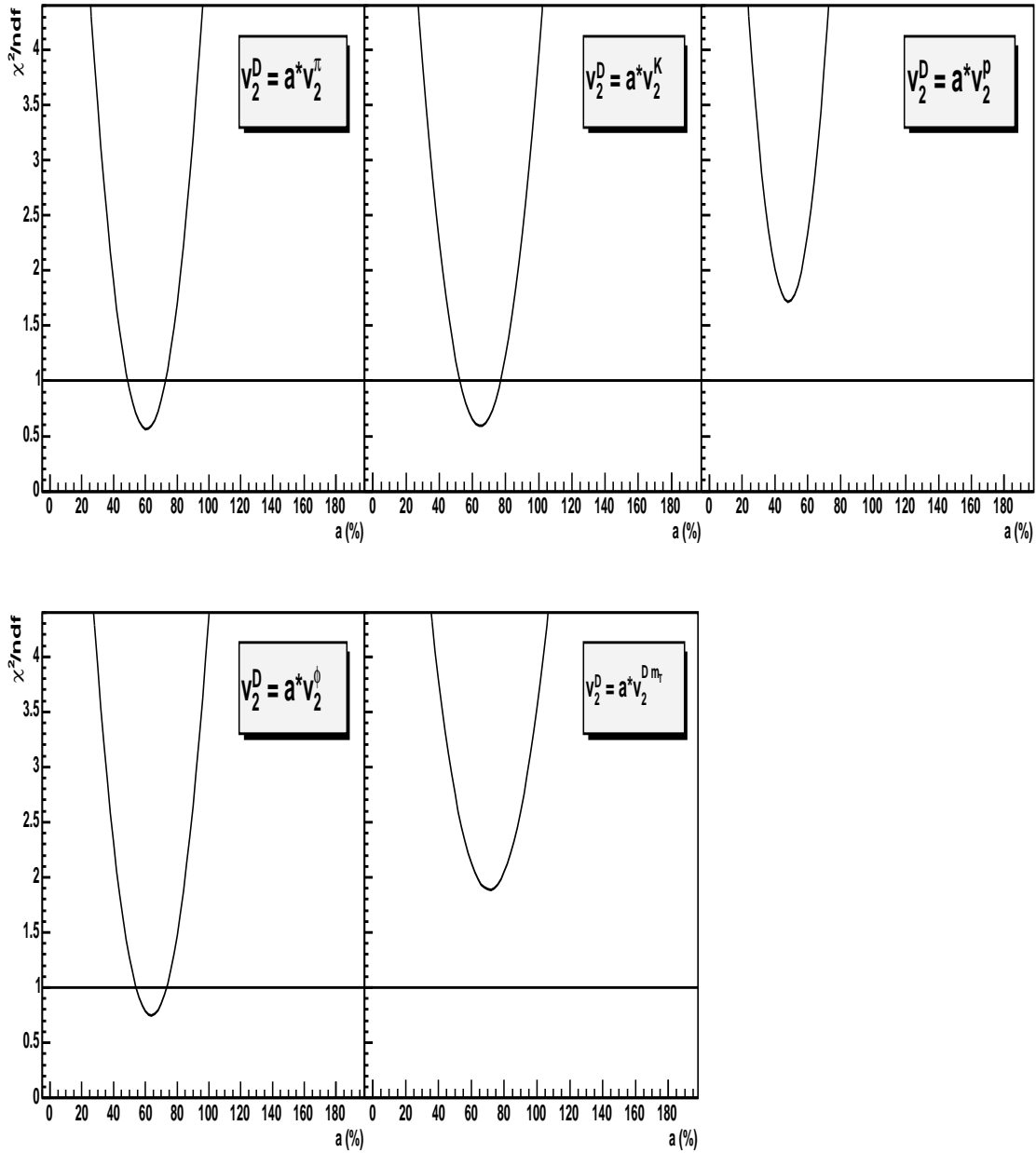


Figure 5.5: Results of the  $\chi^2$  test between measured non-photonic electron  $v_2$  and electron  $v_2$  calculated by the simulation assuming  $D$  meson  $v_2$  shape as a function of the scaled factor  $a(\%)$

the figure is  $\pi v_2$ . The result indicates that  $D$  meson  $v_2$  is smaller than  $\pi v_2$  below  $p_T < 3.5$  GeV/c.

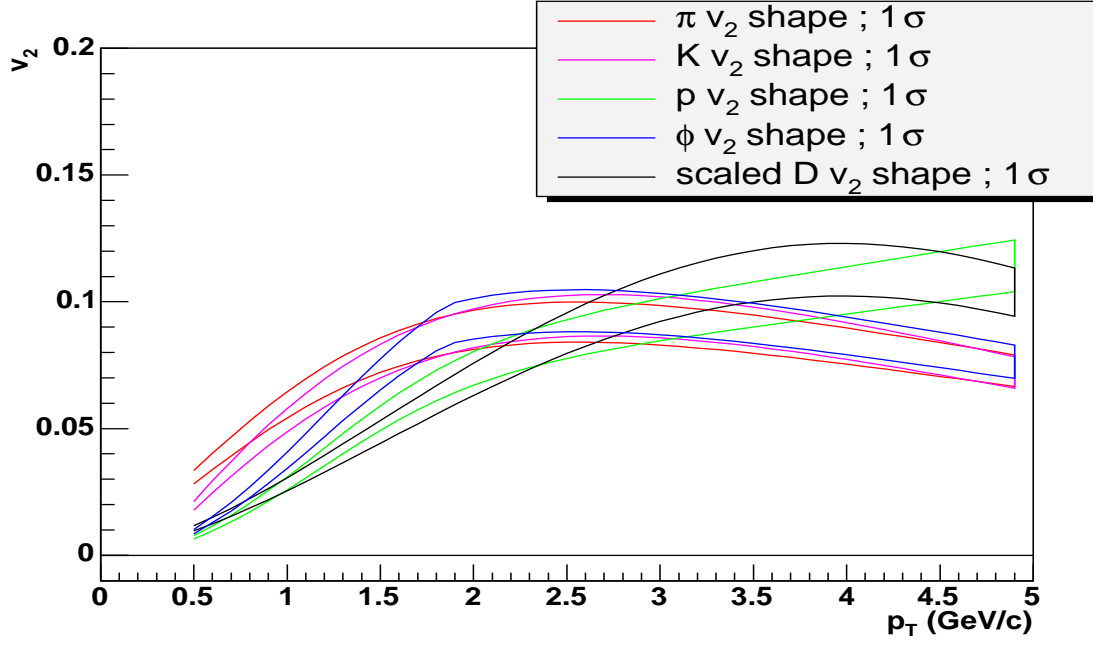


Figure 5.6:  $1\sigma$  bands for each of the five assumed  $D v_2$  shapes.

### 5.3 Charm quark $v_2$ assuming Quark Coalescence Model

Previous measurements of  $v_2$  for hadrons made of light quarks, such as pions and kaons, suggests that the  $v_2$  already formed in the partonic phase. It would indicate that a partonic collectivity has been developed for light quarks, such as  $u$  and  $d$ , in Au + Au collision at RHIC. If  $v_2$  for charm quarks is also a non-zero  $v_2$ , it would be a strong indication of the partonic thermalization not only for the light quarks but also for the heavy quarks in Au+Au collisions at RHIC. As described in Introduction, various measurements in Au+Au collisions at RHIC are well explained by the quark coalescence model. The model can be also useful for charm quark  $v_2$  study. As introduced in Chapter 1.5,  $v_2$  for mesons is expressed as;

$$v_{2,M}(p_T) = v_{2,q}(p_T/2), \quad (5.3)$$

in the quark coalescence framework if the effective masses of constituent quarks are similar. On the other hand, charm quark has much larger mass than the light quark ( $m_c \gg m_u$ ),

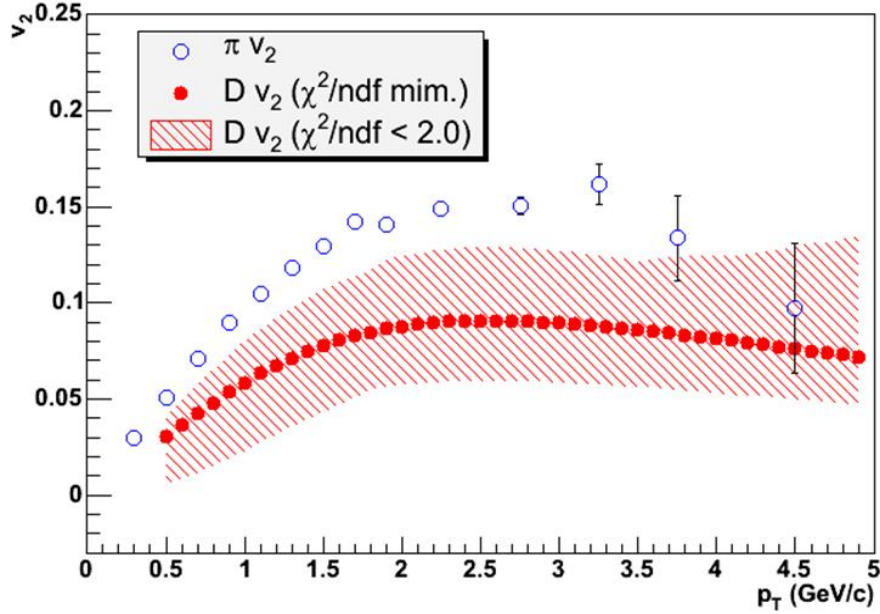


Figure 5.7:  $D$  meson  $v_2$  estimated by the measured non-photonic electron  $v_2$ . The closed data points represent the most suitable  $D$  meson  $v_2$  ( $\chi^2$  minimum) from the calculation. The dashed lines are  $\chi^2$  minimum+2 value for the determination. The open circles is  $\pi v_2$ .

therefore the most of  $D$  meson momentum is carried by the charm quark. As described in [61], the momentum fraction  $x$  in Eq. 1.9 is given as;

$$x = \frac{m_i}{m_M}, \quad (5.4)$$

here  $m_M$  is a mass of meson and  $m_i$  is an effective mass of quark. In case of  $D$  mesons, the momentum fraction  $x$  for  $u$  quark and  $c$  quark is given as  $x_u \sim 1/6$  and  $x_c \sim 5/6$ . The asymmetric momentum configuration arises because coalescence requires the constituents to have similar velocities, not momentum. Thus  $D$  meson  $v_2$  in the quark coalescence framework is written as;

$$v_{2D}(p_T) = v_{2,u}\left(\frac{1}{6}p_T\right) + v_{2,c}\left(\frac{5}{6}p_T\right). \quad (5.5)$$

Here  $v_{2,u}$  is  $u$  quark  $v_2$  and  $v_{2,c}$  is  $c$  quark  $v_2$ . A same  $p_T$  dependent shape for  $v_2$  of charm quark are assumed as for the light and strange quarks. Then we assumed  $v_2$  of  $c$  quark and

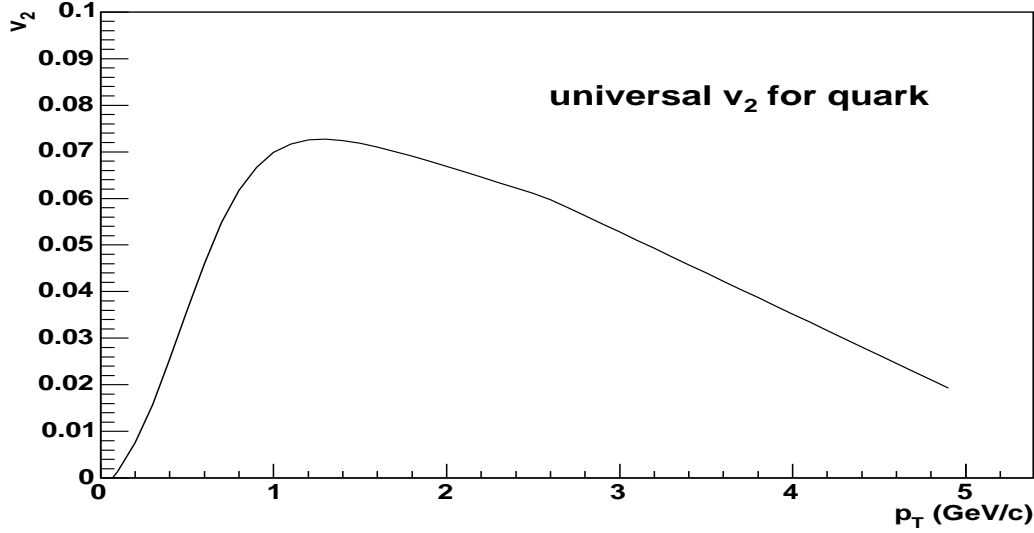


Figure 5.8: Universal  $v_2$  shape for quarks in the calculation.

$u$  quark as;

$$\begin{aligned} v_{2,u}(p_T) &= a \times v_{2,q}(p_T), \\ v_{2,c}(p_T) &= b \times v_{2,q}(p_T), \end{aligned} \quad (5.6)$$

where  $v_{2,q}(p_T)$  means the  $p_T$  dependent shape for quarks  $v_2$ . The shape is shown in Fig. 5.8. Thus  $D$  meson  $v_2$  is given as;

$$v_{2,D}(p_T) = \left(a \times v_{2,q}\left(\frac{1}{6}p_T\right)\right) + \left(b \times v_{2,q}\left(\frac{5}{6}p_T\right)\right). \quad (5.7)$$

We calculated the decay electron  $v_2$  from the  $D$  meson  $v_2$  with a Monte Carlo simulation and determined the parameters  $a$  and  $b$  to reproduce the measured non-photonic electron  $v_2$ . The parameters  $a$  and  $b$  are obtained by a simultaneously fitting not only for the non-photonic electron  $v_2$  but also for kaon and proton  $v_2$ . The fitting function for kaon and proton  $v_2$  is given as;

$$\begin{aligned} v_{2,K}(p_T) &= 2a \times v_{2,q}(p_T/2), \\ v_{2,p}(p_T) &= 3a \times v_{2,q}(p_T/3). \end{aligned} \quad (5.8)$$

If the charm quark  $v_2$  is zero, the parameter  $b$  is also zero. Figure 5.9 show the fitting result of non-photonic electron  $v_2$ , kaon  $v_2$  and proton  $v_2$ . The two parameter  $a$  and  $b$  obtained by the fitting are shown in Fig. 5.10. The contour lines are one sigma step. The most inner

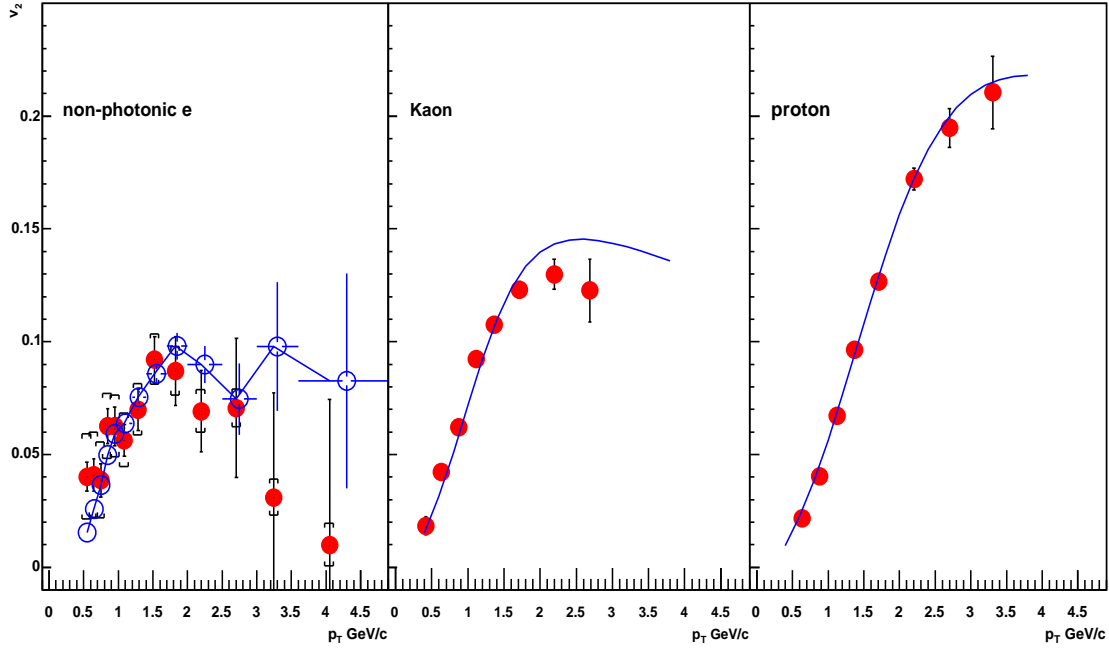


Figure 5.9: Fitting result of non-photonic electron  $v_2$ , kaon  $v_2$  and proton  $v_2$ . The open circles mean decay electron  $v_2$  from the  $D$  meson.

line means  $1 \sigma$  contour level and the most outer line means  $4 \sigma$  contour level. The best fitting parameter set is;  $a = 1.0$  and  $b = 0.96$  with  $\chi^2/\text{ndf} = 21.85/27$ . From the contour plot the parameter  $b$  for charm quark is consistent with the parameter  $a$  for  $u$  quark within the  $1 \sigma$  contour level. Thus  $v_2$  of charm quark is same as  $u$  quark within the  $1 \sigma$  contour level and the data suggest a non-zero charm quark  $v_2$  as regards assuming the universal quark  $v_2$  and applying the quark coalescence model. The strong elliptic anisotropy of charm quarks, which is similar to the light quark, indicates a collectivity of different mass quarks during the quark phase of the high density matter created in the ultra-relativistic heavy-ion collisions. Figure 5.11 shows the charm quark  $v_2$ ,  $v_{2,c} = b \times v_{2,q}(p_T)$ , from the calculation. The solid line is obtained from the  $1 \sigma$  contour level, and the dashed line is obtained  $2 \sigma$  contour level and the dotted + dashed line is obtained from  $4 \sigma$  contour level from the fitting.



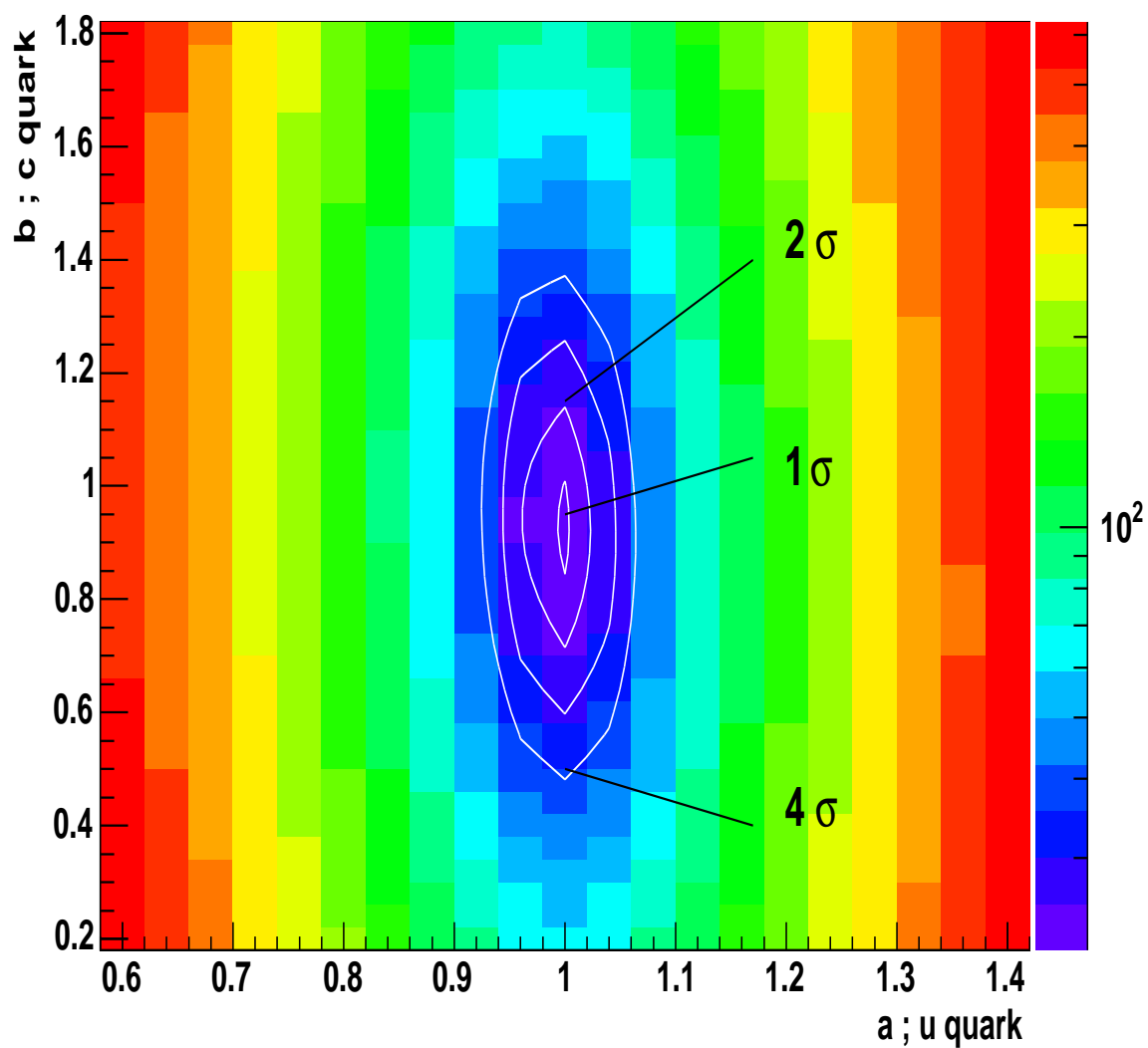


Figure 5.10: Contour plot of  $v_2$  of c quark and u quark which are defined as  $v_{2,u} = a \times v_{2,q}$  and  $v_{2,c} = b \times v_{2,q}$ . Here  $v_{2,q}$  is a quark  $v_2$  determined by the measured  $v_2$ . Parameters  $a$  and  $b$  are obtained by fitting the measured non-photonic electron  $v_2$ , Kaon  $v_2$  and proton  $v_2$ . The contour lines are one sigma step.

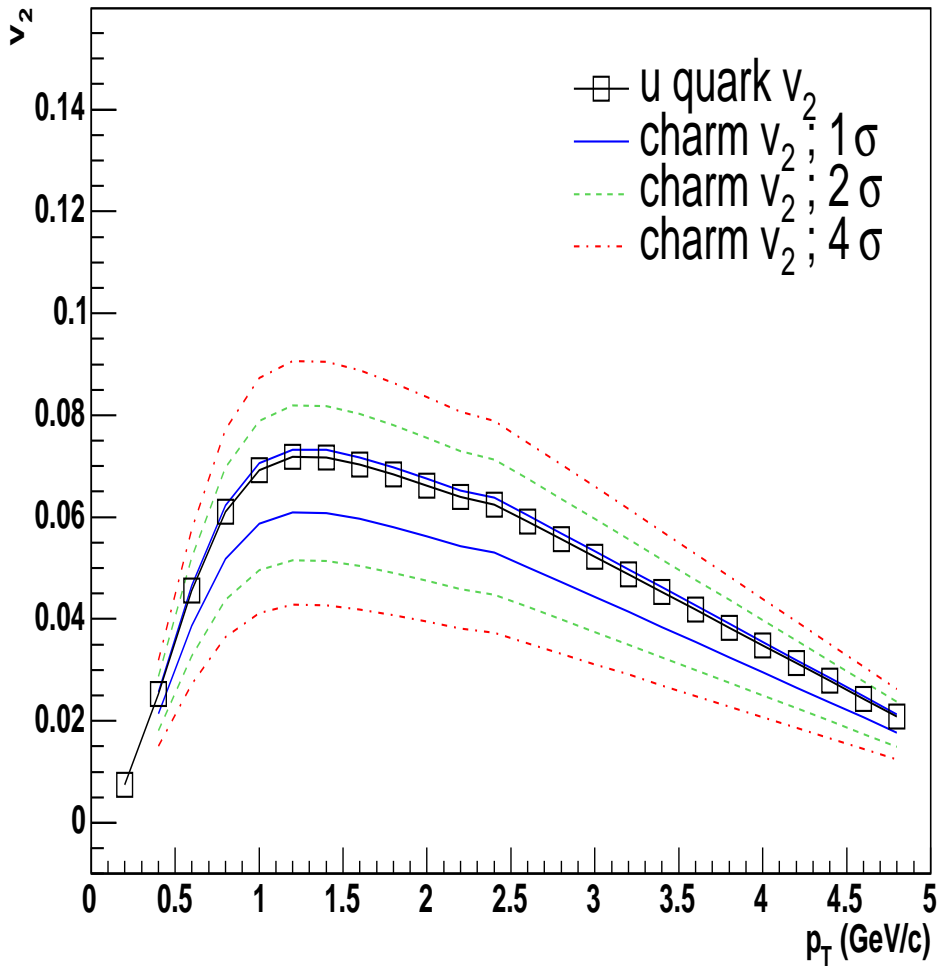


Figure 5.11: Charm quark  $v_2$  from the calculation based on the quark coalescence model. The solid lines are obtained from  $1\sigma$  contour level, the dashed lines are obtained  $2\sigma$  contour level and the dotted + dashed lines are obtained from  $4\sigma$  contour level by the fitting. The open boxes mean  $u$  quark  $v_2$ .

## 5.4 Bottom quark contribution to the non-photonic electron $v_2$

In the reported momentum region, the dominant source of the non-photonic electron is charm quark decay. On the other hand, bottom quark contributions to the non-photonic electrons would be larger than the charm quark at high  $p_T$  region. Current bottom quark contribution to the non-photonic electron is model dependent. Based on a pQCD (FONLL), electron from bottom quark decay is calculated and it predicts that the contribution is larger than that of charm quarks above  $4.5 \text{ GeV}/c$  ( $N_{b \rightarrow e}/N_{c \rightarrow e} > 1.0$  above  $p_T = 4.5 \text{ GeV}/c$ ). As shown in Fig. 1.14, the prediction consists with the non-photonic electron measured in  $p + p$  collisions at PHENIX experiment.

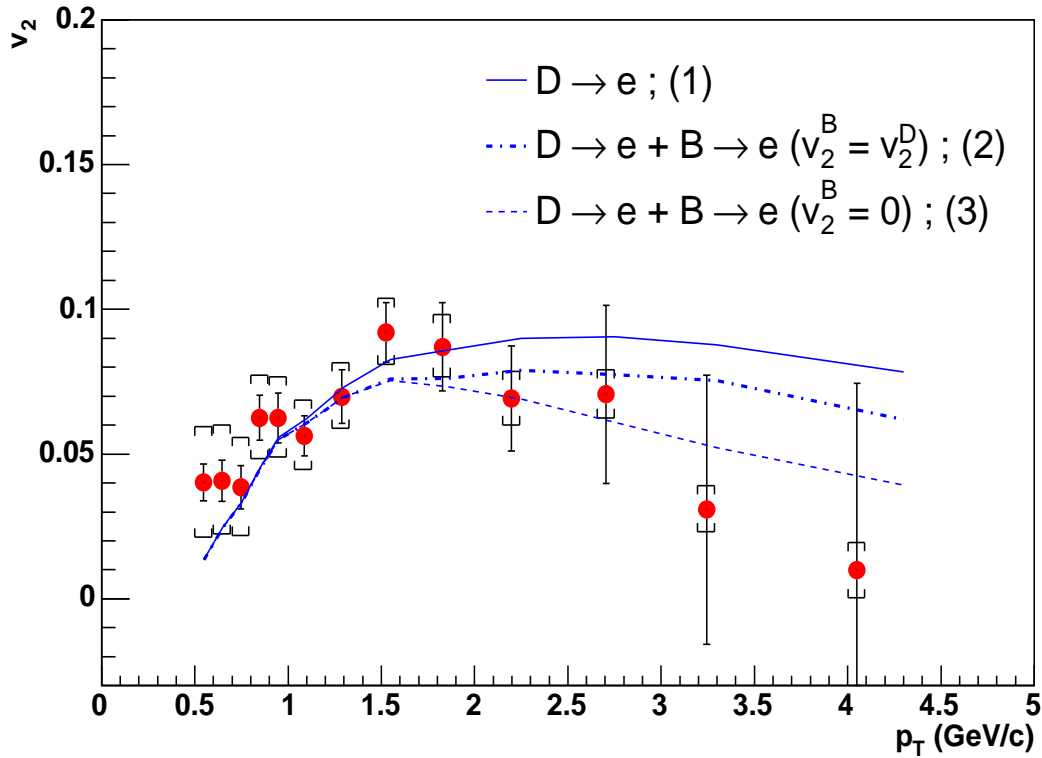


Figure 5.12: Electron  $v_2$  from  $D$  meson and  $B$  meson. The curve (1) is assumed no  $b$  quark contributions to the non-photonic electron (only take into account charm decay). The curve (2) is assumed that  $D$  meson and  $B$  meson  $v_2$  have same  $v_2$ . And the curve (3) is assumed that  $B$  meson  $v_2$  is zero.

We studied bottom quark contributions to the non-photonic electron  $v_2$ . The non-photonic electrons originating from bottom quarks mainly decay from  $B$  mesons which contain a bottom quark. In this study, we considered three extreme models for  $B$  meson. The first model assumes no  $B$  meson (no bottom quark) contribution to the non-photonic electron  $v_2$  (curve 1). The second model assumes that  $D$  meson and  $B$  meson have same  $v_2$  (curve 2). And the third model assumes that  $B$  meson  $v_2$  is zero (curve 3). This assumption arises from that  $B$  meson has much larger mass than  $D$  meson, thus the  $v_2$  of  $B$  is much smaller than  $D$  meson  $v_2$ . For the model (2) and (3), a ratio of electrons from charm and bottom ( $N_{b \rightarrow e}/N_{c \rightarrow e}$ ) is obtained from the pQCD calculation [40] in Fig. 1.14. The  $D$  ( $B$ ) meson  $v_2$  was used the  $v_2$  determined from the non-photonic electron  $v_2$  in Chapter 5.2 for the model (2). Figure 5.12 shows results of the model calculations. As we see, bottom quark contributions reduce the non-photonic electron  $v_2$  at high  $p_T$  region. The reason why the second model is smaller than the first model is that the decay electron  $v_2$  from  $B$  meson decay is largely smeared due to the large mass difference between  $B$  meson and electron. Current measured non-photonic electron  $v_2$  has large errors at high  $p_T$  and it consistent with the three models.

## 5.5 Comparison with charm quark thermalization model

One of the big questions in heavy ion collisions at RHIC is the thermalization of the charm quark. As we discussed, the measured non-photonic electron spectrum is consistent with pQCD calculation. On the other hand, it was pointed out in [10], electron spectrum also reproduce by the hydrodynamical models assuming the complete thermal equilibrium for charm hadrons. The curves in fig. 5.13 are the electron  $p_T$  spectra from the model calculations. The data in the figure is non-photonic electron spectrum measured at PHENIX in Au+Au collisions at  $\sqrt{s_{NN}} = 130$  GeV [51]. The solid curves are electron spectrum obtained by the initial pQCD charm production without final state interactions (PYTHIA) and the dashed curves are the spectrum by the complete thermal equilibrium for charm hadrons (hydro model). The difference between two models are very small at low  $p_T$  region. Thus the spectrum is not sensitive to the thermalization of charm quarks.

On the other hand, it has been predicted that the elliptic flow of electron from charm is very sensitive to the thermalization of charm quarks [62]. In the calculation  $D$  mesons are formed by the charm quark coalescence with thermal light quarks at the hadronization stage. For charm quark momentum spectra, two extreme scenarios are considered. The first scenario assumes no reinteractions after the production of charm-anticharm quark pairs at the initial state hard processes (calculated from PYTHIA). The second scenario assumes complete thermalization with the transverse flow of the bulk matter. Both scenarios pro-

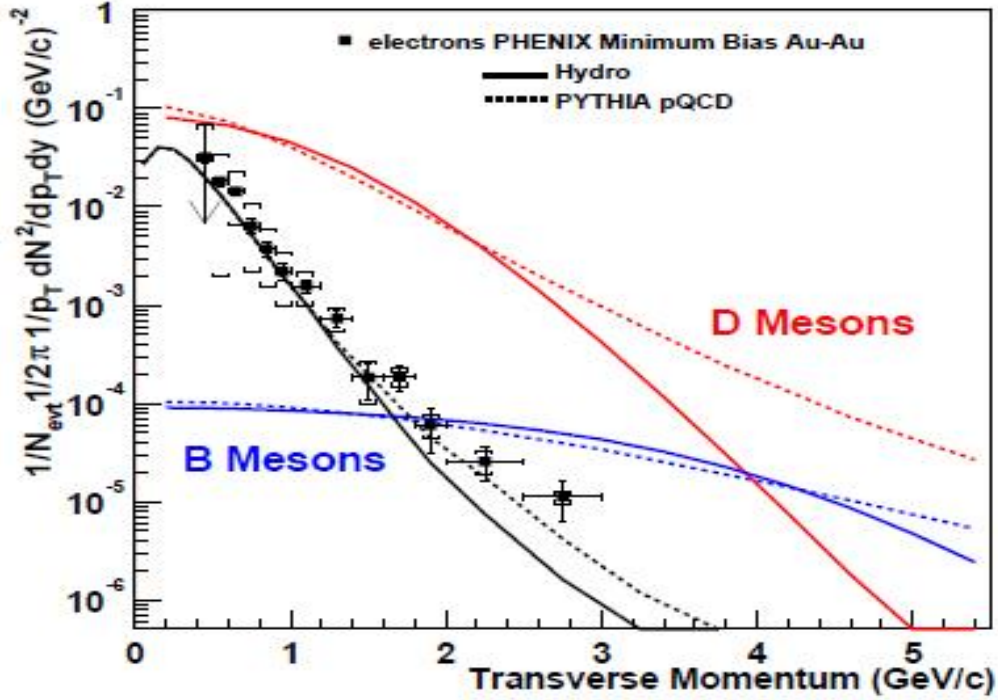


Figure 5.13: The electron spectra from the model calculations. The dashed curves are the PYTHIA calculation and solid curves are the results from the thermal hydrodynamic model. The data in the figure is non-photonic electron measured at PHENIX in Au+Au collisions at  $\sqrt{s_{NN}} = 130$  GeV [51]. The picture is taken from [10].

duce electron spectra from  $D$  meson decays which are consistent with non-photonic single electron spectra as published by PHENIX. In both scenarios,  $B$  meson contribution is not taken into account. Fig. 5.14 shows the  $v_2$  of decay electrons from  $D$  mesons in the "no reinteraction" scenario as a dashed line, while the solid line represents the "thermalization" scenario. Even if the charm quark  $v_2$  is zero, electron  $v_2$  for "no reinteraction" scenario is not zero due to the  $v_2$  of light quark component. The model predicts that the electrons from the thermalized model has two times larger  $v_2$  than the pQCD model. Thus the non-photonic electron  $v_2$  is sensitive the charm quark thermalization. The red data points are the measured non-photonic electron  $v_2$  values as presented in this thesis. The "thermalization + flow" scenario well reproduces the measured non-photonic electron  $v_2$  below 1.5 GeV/c.

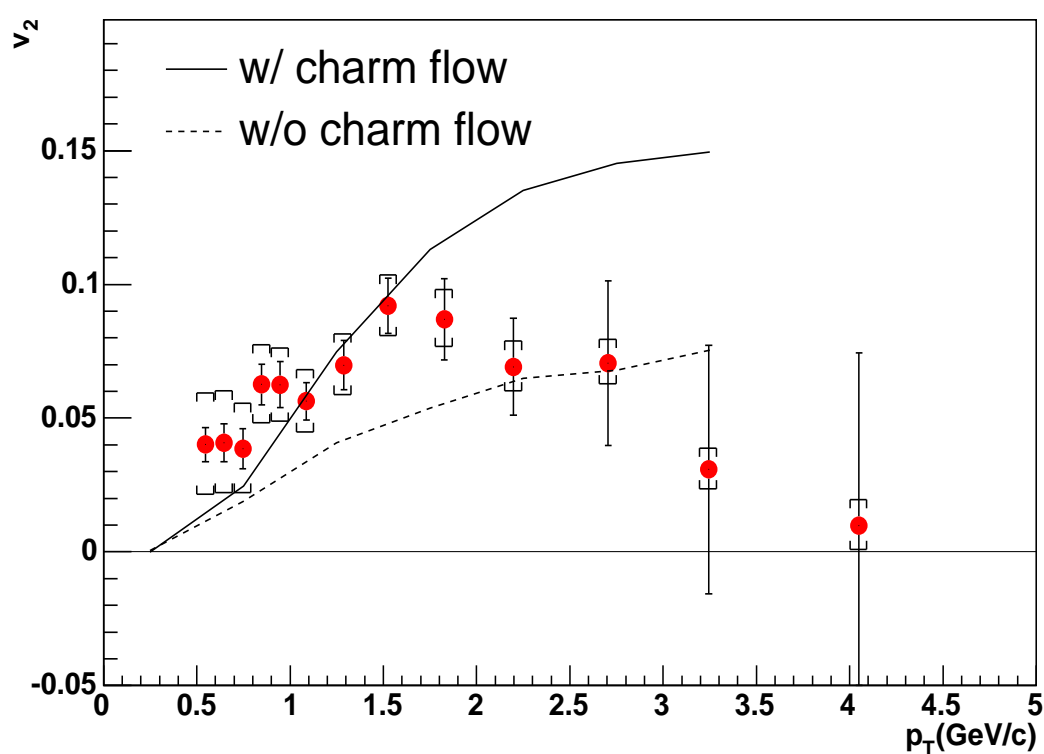


Figure 5.14: Comparison of the non-photonic electron  $v_2$  with two different charm flow scenarios [62]. The solid line corresponds to the no rescattering of the initially produced charm quarks (without flow), while the dashed line reflects the effect of complete thermalization (with flow).

## 5.6 Non-photonic electron $R_{AA}$ and $v_2$

As introduced in Chapter 1.4, neutral pions and charged hadrons are largely suppressed at high  $p_T$  region in Au+Au collisions compared with that in  $p + p$  collisions. Such the suppression is not observed in  $d$ +Au collisions, thus the suppression in Au+Au collisions is due to the final state interactions. This suppression is well represented a model which assumes partons energy loss in the dense matter. The suppression has been also observed the non-photonic electrons in Au+Au collisions. As we shown in the Fig. 5.1, the invariant  $p_T$  spectra of the non-photonic electron in Au+Au collisions agree well with  $p + p$  reference at low  $p_T$  in all centrality. On the other hand, a suppression with respect to  $p + p$  collisions develop at high  $p_T$ . The suppression is quantified the nuclear modification factor,  $R_{AA}$ , which is defined as;

$$R_{AA} = \frac{d\sigma_{Au+Au}}{\langle N_{binary} \rangle \times d\sigma_{p+p}}. \quad (5.9)$$

Figure 5.15 shows the  $R_{AA}$  for the non-photonic electrons as a function of  $p_T$  in most central collisions (centrality 0 - 10 %) measured in Au+Au collisions at  $\sqrt{s_{NN}} = 200$  GeV. We see the  $R_{AA}$  is unity ( $R_{AA} = 1.0$ ) at low  $p_T$ . This means that the yield of the non-photonic electron is scaled by the number of collisions ( $N_{coll}$ ). As we discussed, charm quarks are produced at the initial collisions and the total yield is scaled by the number of collisions ( $N_{coll}$ ). The result is consistent with charm quark production. On the other hand, the  $R_{AA}$  for the non-photonic electron is smaller than unity ( $R_{AA} < 1.0$ ) at high  $p_T$  region and it is same as the  $R_{AA}$  for the neutral pions ( $R_{AA} \sim 0.2$ ). Thus the suppression suggests that charm and bottom quarks also lose their energy in the dense matter same as light quarks. It should be noted that the energy loss of charm have little effect on the total charm yield.

This result leads that a very dense partonic matter, even if heavy quarks ( $c$  and  $b$ ) are stopped, is created in Au+Au collisions at RHIC energy. The curve in the figure is model calculation includes gluon radiations as a mechanism of the parton energy loss. The model assumes that an initial gluon density is 3500 ( $dN_g/dy = 3500$ ) [63]. Thus the  $R_{AA}$  for the non-photonic electron suggests that a large initial gluon density is achieved ( $dN_g/dy > 3500$ ) in Au+Au collisions. In such the dense partonic matter, a mean free path of charm quark would be smaller than the system size. We briefly estimated the mean free path of charm quark in the dense matter. Applying Bjorken formula Eq. 1.1, the parton density per volume would be given as;

$$n = \frac{1}{\tau A_{\perp}} \frac{dN_p}{dy}. \quad (5.10)$$

In this calculation, we used life time of QGP ( $\sim 5$  fm/c) for  $\tau$  and assumed an initial parton density per rapidity is  $dN_p/dy \sim dN_g/dy = 3500$ . Under the assumptions, the parton density

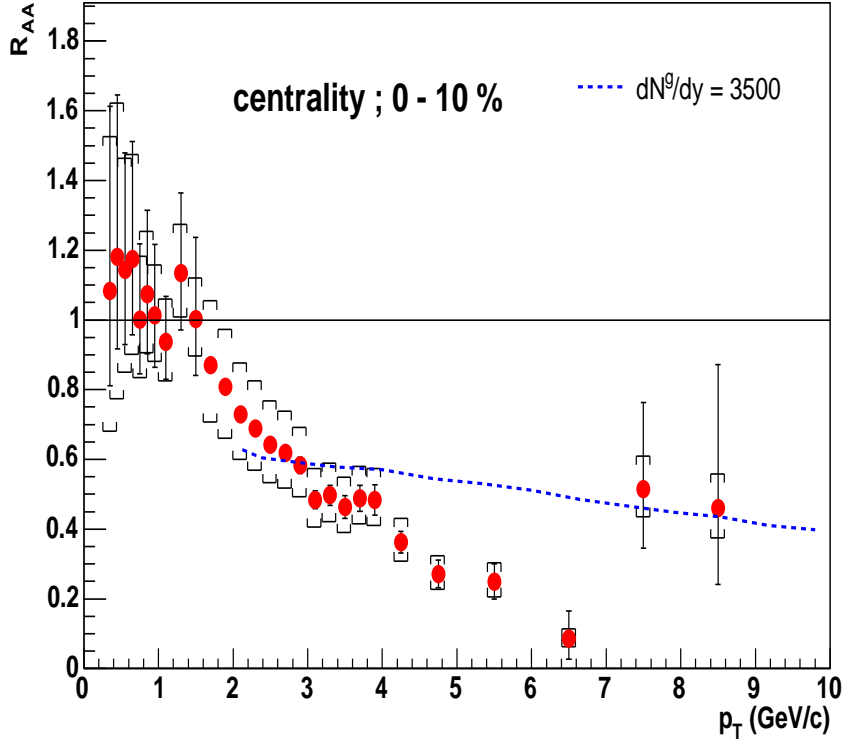


Figure 5.15:  $R_{AA}$  of the non-photonic electrons in 0-10 % central collisions compared with model calculations assuming the initial gluon densities is 3500 ( $dN^g/dy = 3500$ ).

per volume is  $n = 7 \text{ (fm}^{-3}\text{)}$ . The perturbative QCD estimated charm rescattering cross section is about 3 mb [64]. Then we got the mean free path of charm quark is about 0.5 fm. This value is smaller than the size of the system ( $R \sim 6 \text{ fm}$ ). The length of the mean free path is important parameter for  $v_2$ . If the path is larger than the system, the emission pattern in the azimuthal space is isotropic. On the other hand, the emission pattern in the azimuthal space is anisotropic if the path is smaller than the system. Thus we expect the azimuthal anisotropy of charm quarks. This result consistent with the non-zero charm quark  $v_2$  as we discussed in this chapter.

Measurements of  $v_2$  and  $R_{AA}$  for the non-photonic electron suggest that charm quark flow and energy loss in the matter created in Au+Au collisions. Large charm quark energy loss suggests that the matter created Au+Au collisions are very dense. Charm flow suggests that charm quarks are frequently scattered in the dense partonic matter. Thus we expect that thermalization of charm quark is achieved. If charm quark is really thermalized in



the matter, thermalization time of charm quark must be comparable to existence time of QGP ( $< 5$  fm/c). Information about thermalization time of charm quark is gained from the non-photonic electron  $v_2$  and  $R_{AA}$  compared with a model prediction. The curves on the figures are results of the model [65]. The main assumption in the model is elastic scattering mediated by resonance excitation of  $D$  meson and  $B$  meson in QGP. Theoretical evidence for the resonance state is provided by QCD calculations [66] [67]. The model simultaneously reproduce the measured non-photonic electron  $R_{AA}$  and  $v_2$ . It was pointed in [68], resonance state of  $D$  meson and  $B$  meson reduce charm quark thermalization times by a factor of  $\sim 3$  compared to pQCD and it is about a few fm/c. The thermalization time is comparable existence time of QGP. Thus the measured non-photonic electron  $R_{AA}$  and  $v_2$  suggest that charm quark thermalization is achieved in Au+Au collisions.

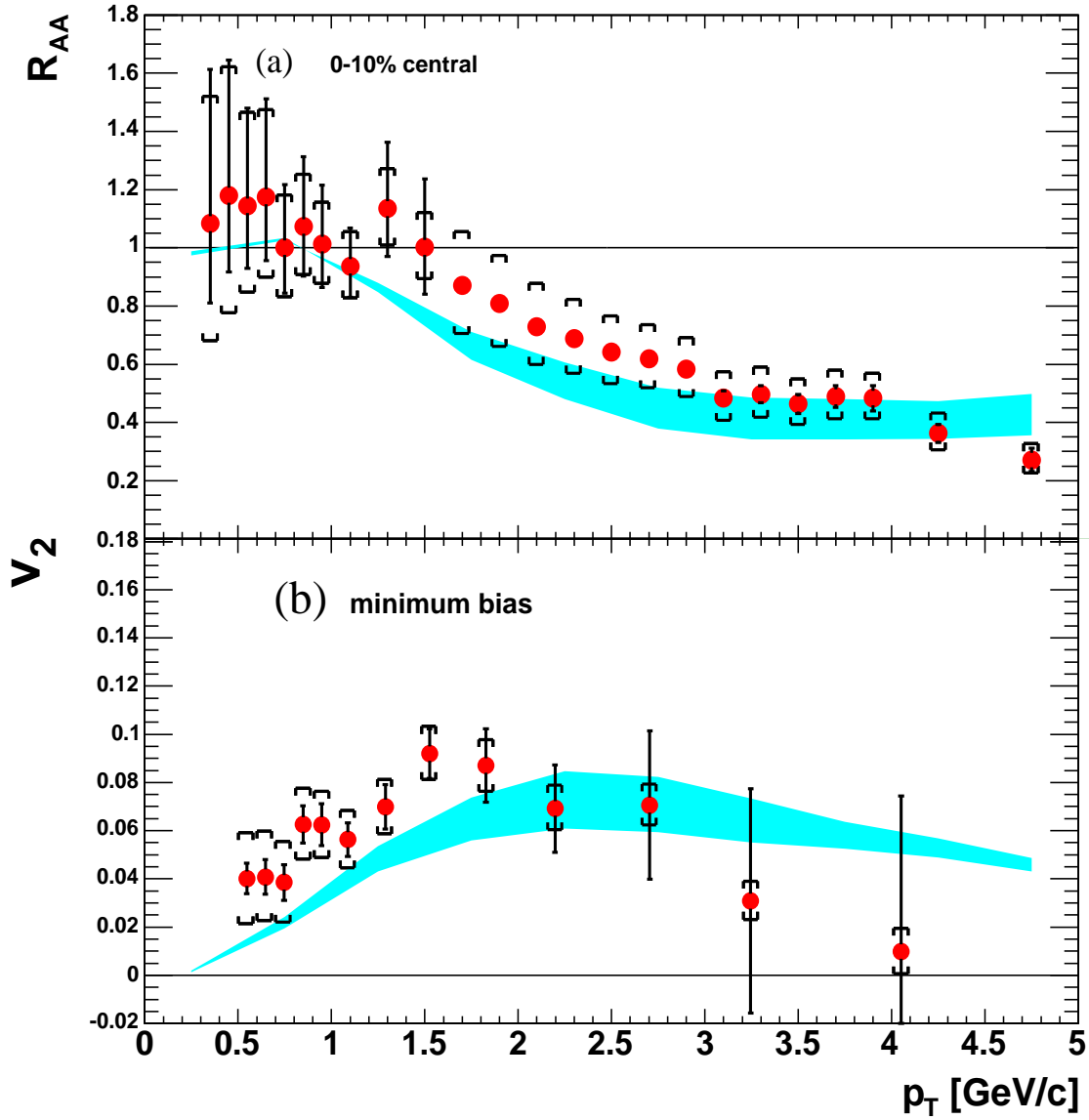


Figure 5.16: (a)  $R_{AA}$  of the non-photonic electron in 0-10 % central collisions. (b)  $v_2$  for the non-photonic electron in minimum bias collisions. The curves in the figure are model calculations assuming elastic scattering mediated by resonance excitation of  $D$  meson and  $B$  meson in QGP [65].

# Chapter 6

## Conclusions

In this thesis, we have studied the elliptic azimuthal anisotropy of charm quark via electron measurement. We first measured the transverse momentum dependence of the azimuthal anisotropy parameter  $v_2$ , the second harmonic of the azimuthal distribution, for electrons at mid-rapidity ( $|\eta| < 0.35$ ) with the PHENIX detector in Au+Au collisions at  $\sqrt{s_{NN}} = 200$  GeV. From the result, we have extracted electron  $v_2$  from heavy flavor decays by subtracting  $v_2$  of electrons from other sources such as photon conversions and Dalitz decay. This photonic electron  $v_2$  is determined with a Monte Carlo simulation using measured  $v_2$  and  $p_T$  distributions of these photonic sources. The yield of the non-photonic electron after subtracting the background is consistent with the expected yield from charm decay. Therefore the non-photonic electron  $v_2$  can be reflected the charm quark  $v_2$ . We found that the non-photonic electron  $v_2$  is clearly positive below 3.0 GeV/ $c$  in the minimum bias event sample. The non-photonic electron  $v_2$  is smaller than the  $\pi$   $v_2$  in whole  $p_T$  range, but the trend is same as  $\pi$   $v_2$ , increasing with  $p_T$  up to about 1.5-2.0 GeV/ $c$  and then saturate or slightly reduces with increasing  $p_T$ .

The main source of the non-photonic electron is  $D$  meson decay. We found that the decay angle is strongly correlated with the angle of the parent  $D$  meson and the decay electron  $v_2$  well reflects the parent  $D$  meson  $v_2$ . Therefore the non-zero  $v_2$  for the non-photonic electron gives a non-zero  $D$  meson  $v_2$ . We have extracted the  $D$  meson  $v_2$  from the non-photonic electron  $v_2$  by assuming various  $p_T$  dependent shape of  $D$  meson  $v_2$ .  $D$  meson prefers a pion like  $v_2$  shape which saturates around 2.0 GeV/ $c$  and the peak  $v_2$  value is obtained to be  $0.09 \pm 0.03$  at about 2-3 GeV/ $c$ .

Based on a quark coalescence model, we finally estimated charm quark  $v_2$  from the non-photonic electron  $v_2$ . In the calculation, the same  $p_T$  dependent shape for  $v_2$  of charm quark is assumed as for the light and strange quarks, and the effective mass of charm quark is used

for coalescing them at similar velocity. Simultaneous fitting of measured  $v_2$  parameters for pion, Kaon, proton and the non-photonic electron are done with 2  $v_2$  parameters for light and heavy quarks including the quark coalescence effect and  $D$  meson decay kinematics. We found that the extracted charm quark  $v_2$  has similar magnitude compared with the light quark. The strong elliptic anisotropy of charm quarks, which is similar to the light quark, indicates a collectivity of different mass quarks during the quark phase of the high density matter created in the ultra-relativistic heavy-ion collisions. The strong anisotropy of charm quarks also indicates that charm quarks are frequently scattered in the dense partonic matter due to their large mass, and we expect thermalization of charm quarks. We compared our result with a model assuming complete thermalization with the transverse flow of the bulk matter. Below 1.5 GeV/ $c$  the non-photonic electron  $v_2$  is in good agreement with the model. The energy loss of charm quarks is also observed via electron measurement at RHIC. The theoretical model predicts that the early time thermalization of charm quarks, which is comparable to QGP life time, is required to reproduce the non-photonic electron  $v_2$  and  $R_{AA}$ . Thus presented results on  $v_2$  measurement of the non-photonic electron could be one of the strong evidences of QGP formation at RHIC.

# Bibliography

- [1] F. Karsch, Lect. Notes Phys. 583 (2002) 209.
- [2] P. Braun-Munzinger, Nucl. Phys. A 681 119-123 (2001)
- [3] J D Bjorken Phys. Rev. **D27**:140, (1983)
- [4] PHENIX Collaboration, S.S. Adler *et al.*, Phys. Rev. **C71**,034908 (2005)
- [5] PHENIX Collaboration, K. Adcox *et al.*, Nucl. Phys. A volume 757, Issues 1-2, page 184-283 (2005)
- [6] P. F. Kolb, nucl-th/0304036
- [7] R. Baier *et al.*, Nucl. Phys. B484 (1997)
- [8] Y.L. Dokshitzer and D.E. Kharzeev, Phys. Lett. **B519**, 199 (2001)
- [9] L. Grandchamp and R.Rapp, Phys. Lett. **B523**, 60 (2001)
- [10] S. Batsouli *et al.*, Phys. Lett. **B577**, 26 (2003)
- [11] Braun-Munzinger *et al.*, Phys. Lett. **B518**, 41 (2001)
- [12] B. Alper *et al.*, Nucl. Phys. **B100** 237 (1975)
- [13] J. Y. Ollitrault, Phys. Rev.**D46**, 229 (1992)
- [14] Nu Xu for the NA44 Collaboration, Nucl. Phys. **A610** 175 (1996)
- [15] I.G. Berden *et al.*, Phys. Rev. Lett. **78**, 2080 (1997)
- [16] Akio Kiyomichi, Doctor thesis, January 2005
- [17] PHENIX Collaboration, S.S. Adler *et al.*, Phys. Rev. C 69, 034909 (2004)

- [18] H. Sorge, Phys. Rev. Lett. **82**, 2048 (1999)
- [19] PHENIX Collaboration, S.S. Adler *et al.*, Phys. Rev. Lett. **91**, 182301 (2003)
- [20] STAR Collaboration, J. Adams *et al.*, Phys. Rev. Lett. **87**, 182301 (2001)
- [21] STAR Collaboration, J. Adams *et al.*, Phys. Rev. Lett. **89**, 132301 (2002)
- [22] STAR Collaboration, J. Adams *et al.*, Phys. Rev. Lett. **92**, 052302 (2004)
- [23] P. Houvinen, P.E. Kolb, U.W. Heinz, P.V. Ruuskanen, and S.A. Voloshin, Phys. Lett. **B503**, 58 (2001)
- [24] STAR Collaboration, J. Adams *et al.*, Phys. Rev. Lett. **93** (2004) 252301
- [25] PHENIX Collaboration, S.S. Adler *et al.*, Phys. Rev. Lett. **91**, 072303 (2003)
- [26] D. Antreasyan *et al.*, Phys. Rev. **D19**,764 (1979)
- [27] M. Gyulassy and M. Plumer, Phys. Lett. **B243**,432 (1990); R. Baier *et al.*, Phys. Lett. **B345**,277 (1995)
- [28] X. N. Wang and M. Gyulassy, Phys. Rev. Lett. **68**,1480 (1992); X. N. Wang, Phys. Rev. **C58**,2321 (1998)
- [29] X. N. Wang, Nucl. Phys. **A715**, 775c (2003)
- [30] PHENIX Collaboration, S.S. Adler *et al.*, Phys. Rev. Lett. **91**, 172301
- [31] P. Abreu, *et al.*, Eur. Phys. J C **17** (2000) 207
- [32] Berndt Muller. Hadronic Signals of Deconfinement at RHIC. nucl-th/0404015
- [33] R. J. Fries *et al.*, Phys. Rev. C **68**, 044902
- [34] B.L. Combridge, Nucl. Phys. B **151** 429 (1979)
- [35] X. N. Wang and M. Gyulassy, Phys. Rev. D **44**, 3501 (1991)
- [36] F.W. Busser *et al.*, Phys. Lett. **53B**, 212 (1974)
- [37] F.W. Busser *et al.*, Nucl. Phys. **B113**, 189 (1976)
- [38] I. Hinchliffe and C. H. Llewellyn Smith, Phys. Lett. **61B**, 472 (1976); M. Bourquin and J.-M. Gaillard, Nucl. Phys. **B114**, 334 (1976)

- [39] A. Adare *et al.*, hep-ex/0609010
- [40] M. Cacciari *et al.*, Phys. Rev. Lett. **95**, 122001 (2005)
- [41] P. Levai *et al.*, Phys. Rev. C51 : 2177-2187, 1995
- [42] PHENIX Collaboration, S. S. Adler *et.al.*, Phys. Rev. Lett. **94**, 082301 (2005)
- [43] K. Adcox *et al.*, Nucl. Instrum. Methods Phys. Res. **A499**, 469 (2003)
- [44] PHENIX Collaboration, S.H. Aronson *et al.*, Nucl. Instrum. Methods Phys. Res. **A499**, 480 (2003)
- [45] NA 49 Collaboration. Eur. Phys. J. **C2**, 383 (1998)
- [46] S. Butsyk, hep-ex/0511048
- [47] S. Voloshin and Y. Zhang, Z Phys. C **70**, 665 (1996)
- [48] A.M.Poskanzer and S.A.Voloshin, Phys. Rev. **C58**, 1671 (1998)
- [49] Jean-Yves Ollitrault Phys. Rev. D **46**, 229 (1992)
- [50] E877 collaboration, J. Barrette *et al.*, Phys. Rev. **C56**, 3254 (1998)
- [51] K. Adcox *et al.*, Phys. Rev. Lett. **88**, 192303 (2002)
- [52] PHENIX Collaboration, S.S Adler et al ., Phy. Rev. Lett. **96**, 202301 (2006)
- [53] V. Ryabov *et al.*, hep-ex/0510017
- [54] F. Kajihara, Quark Matter 2006
- [55] PHENIX Collaboration, A. Adare, et al ., nucl-ex/0611018
- [56] PHENIX Collaboration, S.S Adler et al ., Phy. Rev. Lett. **91**, 072301 (2003)
- [57] PHENIX Collaboration, A. Adare, et al ., nucl-ex/0608033
- [58] PHENIX Collaboration, S.S Adler et al ., Phys. Rev. Lett. **96**, 032302 (2006), D. Winter for the PHENIX Collaboration, nucl-ex/0511039
- [59] PHENIX Collaboration, S.S Adler et al ., Phy. Rev. Lett. **94**, 232301 (2005)
- [60] PHENIX Collaboration, S.S Adler et al ., Phy. Rev. C. **69**, 034909 (2004)

- [61] Zi-wei Lin and Denes Molnar, Phys. Rev. **C68**, 044901 (2003)
- [62] V. Greco, C. M. Ko, R. Rapp Phys. Lett. **B595**, 202 (2004)
- [63] I. Vitev et.al, Phys. Lett. **B632** (2006) 81-86
- [64] Bin Zhang *et.al.*, Phys. Rev. C 72, 024906 (2005)
- [65] H. van Hees et.al, Phys. Rev. **C73** 034913 (2006)
- [66] M. Asakawa et.al, Phys. Rev. Lett. **92**, 012001 (2004)
- [67] F. Karsch et.al, hep-lat/0305025
- [68] H. van Hees et.al, Phys. Rev. **C71** 034907 (2006)
- [69] R. J. Glauber and G. Matthiae, Nucl. Phys. **B21**, 135 (1970)



# Appendix A

## Data points

$pt$	$\nu_2$	stat.err	sys. err
0.546386	0.0401248	0.00635844	0.0188964
0.645676	0.0408199	0.00711689	0.0187716
0.746343	0.0385246	0.00742423	0.0168286
0.847174	0.0625494	0.00767092	0.0144594
0.947197	0.0624677	0.00860714	0.0136772
1.08757	0.0562807	0.00699467	0.0117929
1.28803	0.0697922	0.00922824	0.011447
1.52502	0.0919859	0.0102673	0.0112271
1.8276	0.0869942	0.0152229	0.0106938
2.19729	0.0691944	0.018114	0.00931277
2.70457	0.0706206	0.0307665	0.00841521
3.24475	0.0307921	0.0465096	0.00789024
4.05063	0.00985709	0.0644943	0.0095675

Table A.1: Non-photonic electron  $\nu_2$  (minimum bias).

# Appendix B

## Kinematics

### B.1 Transverse Momentum and Transverse Mass

We take a beam line to be  $z$ -axis of a frame. Consider a particle which has momentum  $p = (p_x, p_y, p_z)$  and mass  $m$ . The momentum component along the beam direction is called the longitudinal momentum  $p_z$ . The perpendicular to the beam direction are combined and called the transverse momentum given as;

$$p_T = \sqrt{p_x^2 + p_y^2} \quad (\text{B.1})$$

The transverse momentum is Lorentz invariant in any frame moving parallel to the  $z$  direction. Using the transverse momentum, the transverse mass is defined as

$$m_T = \sqrt{p_T^2 + m^2}. \quad (\text{B.2})$$

### B.2 Rapidity

Rapidity,  $y$ , which is defined as

$$y = \frac{1}{2} \ln \frac{E + p_z}{E - p_z} \quad (\text{B.3})$$

is used as a target for the position of produced particles on  $z$  axis. The rapidity has a property in that it is additive under Lorentz transformation, just like a Galilean velocity under Galilean transformation. In the relativistic limit ( $p \gg m$ ), the rapidity becomes as;

$$y \sim -\ln\left(\tan\left(\frac{\theta}{2}\right)\right) \equiv \eta \quad (\text{B.4})$$

where  $\theta$  is polar angle. The  $\eta$  is called pseudo-rapidity.

### B.3 Centrality Variables

In heavy ion collisions due to the large size of the nucleus, their geometry aspects plays important role in collision dynamics. Figure B.1 shows an illustration of the collision geometry for a non-head on nucleus-nucleus collision. The vector that connects the center of the nuclei is called "*impact parameter*". Therefore the impact parameter is good guide for the collision geometry. In heavy ion collision impact parameter is represent as "*centrality*". The head on nucleon-nucleon collision is defined as centrality 0% and the variable increase with non-head on collisions. As is shown B.1, only the nucleons in the overlap region of the two nuclei participate in the collisions. These nucleons are called "*participants*" and the rest nucleons which are not participate in the collisions are called "*spectator*". The variable which means how many nucleons participate in the collision is called "*number of participants ( $N_{part}$ )*" and the number of collisions of nucleons in the participant region is called "*number of binary collisions ( $N_{coll}$ )*".

Centrality variables are calculated by the Glauber model [69] which is based on a simple geometrical picture of a nucleus-nucleus collision. The model treats nucleus-nucleus collision as multiple nucleon-nucleon collisions assuming

- nucleus travel in straight line trajectories
- not deflected after collisions
- secondary particles and possible excitation is neglected
- cross section is same in the vacuum

The nucleons in nucleus are randomly distributed according to Woods-Saxon distribution, the density profile  $\rho(r)$  is defined as;

$$\rho(r) = \frac{\rho_0}{1 + \exp(\frac{r-R}{a})} \quad (\text{B.5})$$

where  $R$  is radius of nucleus and  $a$  is surface diffuseness parameter. In case of Au+Au collisions at  $\sqrt{s_{NN}} = 200$  GeV, the parameters are  $R = 6.38$  fm,  $a = 0.54$  fm,  $\rho_0 = 0.169$  fm<sup>-3</sup> and  $\sigma_{NN} = 42$  mb.

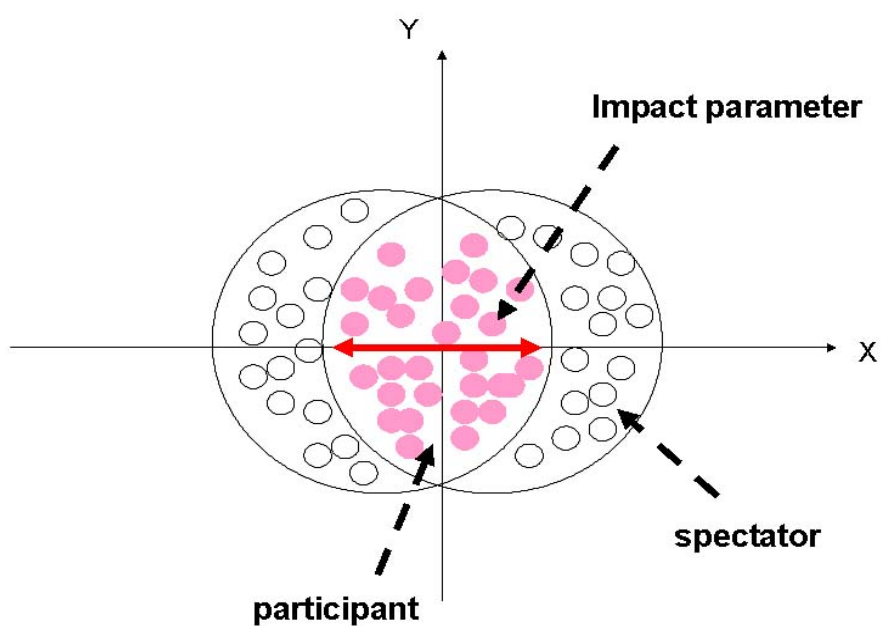


Figure B.1: an illustration of the collision geometry for a non-head on nucleus-nucleus collision. The nucleons in the overlap region of the two nuclei participate in the collisions are called "*participants*" and the rest nucleons which are not participate in the collisions are called "*spectator*"